2013-07-08

Analyses of Nonlinearity Measures in High-Amplitude Sound Propagation

Michael B. Muhlestein
Brigham Young University - Provo

BYU ScholarsArchive Citation
Muhlestein, Michael B., "Analyses of Nonlinearity Measures in High-Amplitude Sound Propagation" (2013). *Theses and Dissertations*. 3994.
https://scholarsarchive.byu.edu/etd/3994

Analyses of Nonlinearity Measures

in High-Amplitude Sound Propagation

Michael Boone Muhlestein

A thesis submitted to the faculty of
Brigham Young University
in partial fulfillment of the requirements for the degree of

Master of Science

Kent L. Gee, Chair
Tracianne B. Neilsen
Derek C. Thomas

Department of Physics and Astronomy

Brigham Young University

July 2013

ABSTRACT

Analyses of Nonlinearity Measures in High-Amplitude Sound Propagation

Michael Boone Muhlestein
Department of Physics and Astronomy, BYU
Master of Science

Military aircraft generate high-amplitude noise which can cause injury to attending personnel. Efforts to mitigate the effects of this noise require a detailed understanding of the propagation of the noise, which was shown previously to be nonlinear. This thesis presents an analysis of high-amplitude noise propagation, emphasizing measures used to quantify the importance of considering nonlinearity.

Two measures of the importance of nonlinearity are compared. These measures are the wave steepening factor and a skewness estimate. The wave steepening factor is a measure of how much nonlinear waveform steepening has occurred in a waveform. The skewness estimate is the skewness of the first time-derivatives of the pressure amplitudes, and can be considered a measure of the shock content in a waveform. These two measures are analyzed analytically in terms of the Earnshaw, Fubini, Fay, and Khokhlov solutions to the Burgers equation. In addition, an analysis of how discrete sampling affects the estimation of these quantities is also presented. It is determined that the wave steepening factor is robust with respect to low sampling rates, but the skewness of the first time-derivatives of the pressure amplitudes is not robust, and requires very large sampling rates to be adequately estimated.

Using numerical and experimental techniques, the two nonlinearity measures are applied to more complicated waveforms, such as Gaussian noise and noise with jet noise-like statistics. It is found that the evolution of the two nonlinearity measures discussed above for noise signals is distinctive in various ways. In particular, the skewness of the first time derivative of the pressure amplitudes suggest that noise waveforms experience nonlinear phenomena faster than initially sinusoidal signals, while the wave steepening factor suggests that they occur at approximately the same rate. The measures are then applied to full-scale military aircraft. By comparing these nonlinearity metrics with the results of the analytical, numerical, and experimental results found in this thesis, it is determined that nonlinearity is likely to be significant in the near field of a military aircraft at military and afterburner engine conditions.

Keywords: jet, nonlinear, shock, skewness, wave steepening factor

ACKNOWLEDGMENTS

I would like to thank the members of my graduate committee for their long suffering with helping learn how to write well. I would especially like to thank Dr. Kent Gee for giving me good advice since 2008 when I started attending the Acoustics Research Group. I would like to thank Dr. Tracianne Nielsen for all of the encouraging words that she has given me, especially as my thesis has drawn to a close. I would like to thank Dr. Derek Thomas for keeping my work high quality, and keeping me on track. It's true… I like analytical rabbit holes.

I would like to thank my wife Natalie for being patient with me getting my work done, especially while she has had hard semesters at the same time that I have.

I would like to thank my parents for all of their support for any endeavor that I have tried, and for my love of learning.

I am grateful to my office mates for putting up with my math and random thoughts (on everything from nonlinear acoustics to Jabberwocky).

This work has been funded in part by NASA, ONR, and by the Department of Physics and Astronomy at Brigham Young University.

Contents

List of Figures

Chapter 1

Introduction

1.1 Background

High-amplitude jet noise propagation has been of interest since the early 1950's, [1] and the effects of nonlinearity in the propagation of such noise have been studied since the early 1970's. [2] Recently, an interest in high-amplitude noise propagation has been renewed because of a concern of the impact of such noise on the environment. In particular, the issues associated with hearing loss of technicians working near military aircraft have resulted in funding for noise propagation research. The majority of studies of jet noise propagation have assumed the propagation of the noise is linear (e. g. Wall *et al.* [3]). However, due to the high-amplitude nature of some jet noise, the validity of the linear approximation is questionable. Since it is difficult to quantify the impact of nonlinear terms in propagation models, or the importance of nonlinearity, in certain scenarios – such as near-field jet noise propagation, due to the large amount of energy at high frequencies and the complicated nature of an extended, directional source – various measures of the importance of nonlinearity in arbitrary waveforms have been proposed. This thesis presents the results of the effort to understand the interpretation of nonlinear measures for high-amplitude noise propagation with applications to jet noise.

1.2 Physical Phenomena

In order to help facilitate an understanding of high-amplitude sound propagation, a brief, qualitative introduction to the physical phenomena associated with nonlinear propagation is presented in this section. A more detailed explanation of these phenomena can be found in Ref. [4] and as part of Chapter 2.

Certain physical phenomena associated with one-dimensional wave propagation are only predicted by propagation models that include second-order corrections or higher. The phenomenon most pertinent to this thesis which requires second-order corrections to model is waveform steepening due to amplitude-dependent processes. The two physical processes which drive the steepening of waveforms are convection and thermal variations. [4] The net effect of these two processes causes the wave speed of a waveform to be amplitude dependent; higher amplitudes will propagate faster than lower amplitudes, leading to shorter pressure rise times in a waveform, hence the name waveform steepening. This deformation of waveforms is manifested in the corresponding spectra by the interactions of acoustic energy with various frequencies. For example, given a sound wave consisting of two different frequencies with significant acoustic energy, nonlinear propagation will transfer energy from these two frequencies to the sum and difference of the two frequencies. [5] Further propagation will cause additional transfer. In short, from a frequency-domain perspective, second-order corrections to propagation models cause all frequencies to interact with all other frequencies.

If a waveform distorts sufficiently, portions of the waveform become nearly discontinuous and are referred to as acoustic shocks. Because acoustic shocks have different propagation behaviors than the rest of a waveform (discussed below), the propagation prior to shock formation is called the pre-shock propagation regime. Any waveform that propagates without linear losses will eventually form shocks, given a large enough propagation distance. The distance at which a waveform propagating without linear losses will generate shocks is called the shock formation distance. As might be expected, the shock formation distance is dependent upon the waveform and propagation geometry. In particular, the shock formation distance is inversely proportional to the greatest time derivative of the waveform and the characteristic frequency, and takes different forms for planar propagation and for cylindrical and spherical spreading. [4] Thus, larger amplitudes and higher frequencies will decrease the shock formation distance of a waveform, and geometric spreading will increase it. Since random noise does not have a fixed greatest time derivative, the shock formation distance for different noise waveforms will in general be different.

For propagation without linear losses, once a shock forms at the shock formation distance, the shock will continue to grow stronger. After three shock formation distances, an initially sinusoidal signal propagating without linear losses will approach a sawtooth wave-like form. For this reason, the propagation of an initially sinusoidal signal without linear losses from one to three shock formation distances is called the shock formation regime, and from three shock formation distances on is called the sawtooth regime.

The propagation of shocks may be fully modeled using the Rankine-Hugoniot shock relations, which are based on conservation of mass, momentum, and energy. [4] By making the assumptions that the shocks in a waveform are weak, energy dissipation is concentrated at the shocks, and shocks are true discontinuities (these assumptions are often valid for high-amplitude noise propagation; see Ref. [4] for a discussion of these assumptions as they relate to acoustic propagation), the Rankine-Hugoniot shock relations may be approximated using what is called weak shock theory. Using weak shock theory, it can be shown that shocks propagate at the average of the sound speeds of the pressure just before and after the shock wave. This means that shock waves can propagate at, above, or below the small-signal speed of sound. An example of the amplitude-dependent sound speed is shown in Figure 1.1. The variable P is a normalized pressure and τ is a normalized retarded time of arrival, which means signals propagating at the small-signal sound speed will not change temporal location. The distance from the source is denoted as x, and x_c is a critical distance that will be discussed below. The source waveform is a double N-wave (two shocks both in front of and behind the pulse center) and the wave propagates as a plane wave without linear losses. Notice that the shocks that have positive peak pressures arrive at earlier values of τ as the pulse propagates, indicating propagation speeds greater than the small-signal sound speed. Likewise, the shocks with negative or zero peak pressures arrive later as the pulse propagates, indicating propagation speeds less than the sound speed.

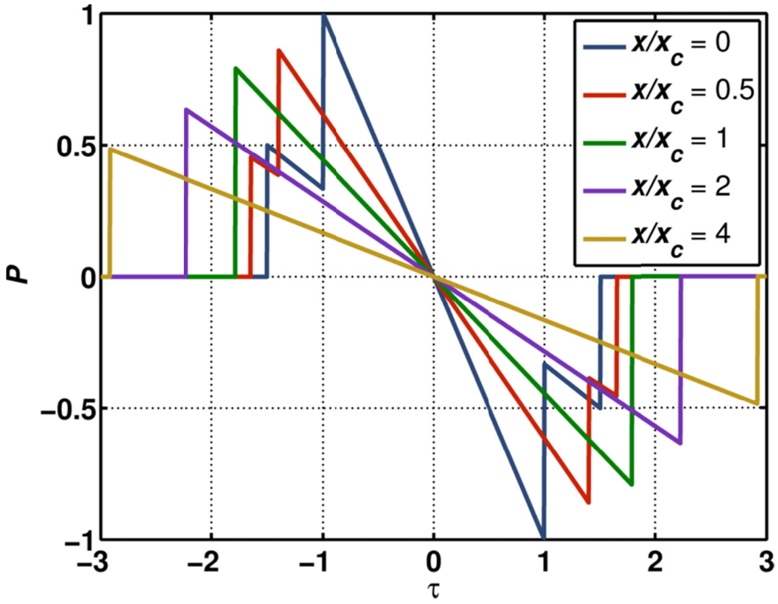

Figure 1.1. An example of shock propagation and coalescence. The source waveform is a double N-wave, and the propagation does not include linear losses. Weak shock theory and the Earnshaw solution were used to predict the propagation. At $x = x_c$ the two positive shocks merge, as do the two negative shocks.

Another aspect of shock propagation seen in Figure 1.1 is attenuation at shocks. [6] Notice the overall amplitude of the pulse decreases as it propagates despite the fact that it is propagating without ordinary losses. This is due to acoustic energy being transferred to thermal energy at the location of a shock. [7] The excess attenuation at shocks is important because it causes information about the source waveform to be lost as a signal propagates.

The example of shock propagation shown in Figure 1.1 also demonstrates another important phenomenon associated with shock propagation, called shock coalescence. [8] [9] Shock coalescence occurs when one shock overtakes another shock. The two shocks merge and propagate as a single shock in a manner distinct from either of the original shocks, thus losing information about the original two shocks. In the example shown in Figure 1.1, the two positive shocks coalesce at the critical distance x_c. Because of shock coalescence and extra attenuation at a shock, it is difficult to obtain source characteristics from measurements far from a high-amplitude noise source.

The success of linear models in most applications of acoustics suggests that nonlinear processes, which, strictly speaking, are always present in acoustic wave propagation, may be dominated by counteracting processes. The most obvious process that opposes nonlinear processes is that of absorption. While nonlinear effects generate energy at sum and difference frequencies as sound propagates, atmospheric absorption due to thermoviscous effects and molecular relaxation will attenuate the sound energy, particularly at high frequencies resulting from sum-frequency generation. If a nonlinear process transfers energy to the sum and difference frequencies more slowly than linear absorptive processes attenuate the energy, then linear processes dominate and that nonlinear process is not important.

Another way linear processes may decrease the importance of including nonlinear terms in propagation models is geometric spreading. Geometric spreading causes the amplitude of a signal to decrease, causing the nonlinear generation of energy at sum and difference frequencies to slow. Spherical spreading causes a signal to decrease in amplitude inversely with distance and cylindrical spreading causes the amplitude to decrease inversely with the square root of distance. In general, the geometric spreading of a signal may be both frequency and propagation distance dependent.

The importance of nonlinearity in the propagation of a signal relative to linear processes may be quantified for an initially sinusoidal signal with the Gol'dberg number. [4] The

Gol'dberg number Γ is defined as a characteristic absorption length divided by a characteristic nonlinear distortion length, and may be interpreted as the relative importance of nonlinearity in propagation relative to absorptive processes. For an initially sinusoidal wave, the characteristic absorption length is the inverse of the absorption coefficient at the frequency of the initial sinusoid and the characteristic nonlinear distortion length is the shock formation distance of the initial sinusoid. Since the shock formation distance of an initial sinusoid is well known for planar, cylindrical, and spherical waves, the Gol'dberg number accounts for both the absorptive and geometrical effects. A small absorption length and large shock formation distance will yield a Gol'dberg number much less than one, which indicates that absorptive processes dominate the propagation, and nonlinear processes may be ignored. On the other hand, a large absorption length and small shock formation distance will yield a Gol'dberg number much greater than one, and indicates that nonlinearity will be very important in the propagation. In the large Gol'dberg number limit, the propagation of a signal may be well approximated by neglecting linear absorption over a short distance relative to the absorption length. The Gol'dberg number will be used extensively throughout this thesis.

It should be noted that the Gol'dberg number was defined in light of nonlinear propagation with thermoviscous losses. Therefore, Gol'dberg number values obtained using absorption coefficients based on relaxational or boundary layer phenomena must be carefully interpreted. In particular, the effects of dispersion [6] [10] must be taken into account when considering real measured data.

Since linear absorption is always present in real acoustic processes, linear processes will dominate the propagation of a waveform if the wave propagates far enough, regardless of the initial amplitude. If a waveform at some distance from the source develops shocks significant enough to be considered sawtooth wave-like (thus having a sawtooth regime), once linear processes dominate, it enters what is called the old-age regime of propagation. In the old-age regime the propagation is characterized by unsteepening of the waveform rather than steepening, caused by the high absorption coefficients that are common to high frequencies. For specific absorption processes, such as thermoviscous losses, the old-age absorption coefficients of the nonlinearly generated harmonics of an initial sinusoid will never return to the linear predictions. For this reason, Pernet coined the phrase “once nonlinear, always nonlinear”. [11]

1.3 Nonlinearity in High-Amplitude Noise Propagation

Nonlinearity has been suspected to be important in high-amplitude noise propagation since before 1973. Pestorius and Blackstock [8] [9] showed both experimentally and computationally that initially 160 dB re 20μPa broadband Gaussian noise in a plane wave tube will generate significant shocks. Based on the spectra of the waveforms with significant shock content that they measured, Pestorius and Blackstock suggested propagation nonlinearity as a possible explanation to anomalously low high-frequency attenuation of measured jet noise. Pestorius *et al*. [12] further showed that shocks would form in plane-wave-tube propagation of broadband noise regardless of the initial phase distribution in the initial broadband signal. More recently, Gee *et al*. [13] studied outdoor, far field measurements of a large sound source capable of producing overall sound pressure levels of 155 dB re 20μPa at a few hundred hertz. They showed the measured harmonics of an initial sinusoid as far as 1 km from the source followed a nonlinear propagation prediction significantly more closely than a linear propagation prediction. This test showed nonlinear effects are important given spherical spreading and large propagation distances, as well as in plane wave tubes.

In addition to computational and experimental efforts to understand the importance of nonlinearity in high-amplitude noise propagation, various analytical descriptions of the evolution of broadband spectra during nonlinear propagation were found from the mid 1970’s to the early 1990’s. Rudenko and Soluyan [14] showed that in the pre-shock propagation regime the high frequencies of broadband noise spectra would trend as the inverse cube of frequency. Scott [15] showed that broadband noise which has developed significant shocks despite thermoviscous absorption will have high-frequency amplitudes that trend as the inverse of the square of frequency. Crighton and Scott [16] developed several asymptotic forms of the Burgers equation. In 1991, Gurbatov *et al*. [17] showed by using an asymptotic form of the Burgers equation that the low-frequency amplitudes of broadband noise with significant shock content follow a frequency squared trend.

Most of the studies dealing with the importance of nonlinearity in broadband noise have been constrained to idealized cases. For example, with the exception of Gee *et al*., the studies discussed above are limited to one-dimensional problems, such as plane-wave tube measurements or plane-wave assumptions. Furthermore, the analytical treatments are constrained by either thermoviscous absorption or no linear absorption. While these idealizations are not valid when considering more realistic and complex situations such as jet noise propagation, they allow important insights into the nature of nonlinearity in broadband noise propagation which may be applied to real world problems.

1.4 Nonlinearity in High-Amplitude Jet Noise

Interest in the importance of nonlinearity in jet noise arose due to anomalously low high-frequency attenuation rates of measured jet noise in the 1960's. In 1971 Pernet and Payne [2] first showed that nonlinearity may be part of the cause of the low attenuation rates. During the rest of the 1970's and early 1980's, several papers dealing with noise measurements of model scale jets, such as Gallagher [18], and of full-scale jets, such as Morfey and Howell [19] and Morfey [20], were published with the perspective of finite-amplitude propagation effects. These papers generally found that nonlinearity in high-amplitude jet noise propagation is important. However, by the mid 1980's, the interest of the aeroacoustics community in the effects of nonlinearity on jet noise propagation had significantly waned.

Recently, there has been renewed funding and interest in the importance of nonlinearity in jet noise due to concerns about the environmental impact of jet noise, in particular the hearing loss of technicians working near military aircraft. Several studies of full-scale military aircraft – in particular, Gee *et al*. has studied noise measurements of the F/A-18E engine, [21] the F-22A Raptor, [22] [23] and the F-35A Joint Strike Fighter [24] [25] – have shown nonlinearity is important in far-field high-amplitude jet noise propagation, and is important to some degree in near-field propagation. While Gee *et al*. studied noise radiating from stationary jets, McInerny *et al*. [26] studied military aircraft flyover measurements and found similar results.

In addition to full-scale jet measurements, a significant number of studies have been based on laboratory-scale jets. [27] [28] [29] [30] There has been some debate as to the importance of nonlinearity in the propagation of noise radiating from laboratory-scale jets. On the one hand, Gee *et al*. have shown preliminary results that suggest that nonlinearity is important in the noise radiated from Mach 2.0 unheated jets, [29] and that there is significant shock formation in the near-field propagation of unheated supersonic jets. [30] On the other hand, Baars et al. have shown evidence that any nonlinearity in waveforms measured near a fully expanded Mach 3 jet is due to source phenomena, and not due to nonlinearity in propagation. However, both Gee *et al*. [30] and Baars *et al*. [28] state that the sampling rates used in their investigations may not have been sufficiently high to adequately resolve characteristics of nonlinearity.

While the importance of nonlinearity in far-field measurements of full-scale jets has been shown conclusively, the degree of importance of nonlinearity in near-field propagation has not yet been established. In an attempt to aid in establishing the importance of nonlinearity in these cases, this thesis provides an extended analysis of some statistical measures of the effects of nonlinearity.

1.5 Measures of Nonlinearity

Several measures of the importance of nonlinearity in noise propagation have been defined. Some of these measures are based on spectral methods, such as an indicator derived by Morfey and Howell, and some are based on time-domain statistical methods, such as skewness estimates. In this section, we will discuss some of the history behind a subset of these measures.

Morfey and Howell [19] derived a cross-spectral form of the Burgers equation which explicitly separates the impact of nonlinearity in a measureable quantity. This quantity, written as Q_{p^2p}, is the quadspectral density between the pressure and the squared pressure, and is considered an indicator of nonlinearity. The quadspectral density has been used in several studies of jet noise propagation. [19] [23] [26] [27] [31] While potentially a useful way of characterizing near-field jet noise propagation nonlinearity, it is beyond the scope of this thesis to consider the quadspectral density. Another way the effect of nonlinearity may be visualized using spectra is to compare the asymptotic spectral slopes of the measured jet noise waveforms with the analytically derived solutions described above. However, there are two problems with this method: First, the analytically derived solutions rely on planar waves propagating with thermoviscous absorption. Since jet noise propagates with a more complicated atmospheric absorption and has a complicated geometry, these assumptions are not valid. Secondly, it has been shown that jet noise close to the source can also have similar slopes to those described in Section 1.2. [32] Thus, whether the spectral slopes are due to source phenomena or propagation phenomena becomes difficult to discern.

Time-domain statistics may be more useful than the spectral methods of determining the role of nonlinearity in near-field jet noise propagation. In 1982 Gallagher [18] defined a metric called the wave steepening factor. The wave steepening factor is the absolute value of the mean negative pressure slope in a waveform divided by the mean positive pressure slope in the waveform, and may be interpreted as a measure of how much distortion has occurred in the waveform due to nonlinear propagation. More on the details of the wave steepening factor will be given in Chapter 2. In addition to Gallagher, Baars *et al*. [28] have reported the wave steepening factor for various laboratory-scale jet noise waveforms. However, there has not been a comprehensive analysis on the interpretation of the wave steepening factor to date. For instance, Gallagher reported that a specific waveform had a wave steepening factor as low as 0.48, but what this means is unknown. The only comments Gallagher gives on the matter is that this value of wave steepening factor is lower than others, suggesting greater distortion. One of the goals of this thesis is to provide a foundation of analysis to interpret the wave steepening factor.

In addition to the wave steepening factor, Gallagher also presented the number of zero-crossings in a waveform per unit time as a nonlinearity measure. The idea behind this value was that as noise with significant shock content propagates, there would be some shock coalescence, which would decrease the number of zero crossings per unit time. However, this metric requires significant shock content in the waveform to be useful. In addition, not all noise waveforms have a zero crossing for every shock (such as rocket noise waveforms; see the waveforms in Ref. [33]), and if they do, the significant shocks are likely to be fairly evenly balanced across the zero pressure line, and will therefore not overtake each other. For these reasons, the number of zero crossings in a waveform will not be considered in this thesis.

Another time-domain measure that may be used to quantify the importance of nonlinearity in the propagation of a wave is the skewness, or the third central moment of a probability density function. Skewness may be interpreted as a measure of the asymmetry in a probability density function, and as such, is zero for a Gaussian process. In an attempt to quantify a perceived phenomenon called "crackle", Ffowcs Williams [34] suggested the skewness of the pressure waveform would be a useful metric. However, Gee *et al*. [35] showed that crackle is more likely associated with the shock content in a waveform, which is not necessarily associated with the time-domain statistics of a waveform. McInerny and Ölçmen [33] suggested the statistics of the time derivative of a pressure waveform, rather than the pressure waveform itself, will yield more pertinent information concerning shock content in the waveform. In addition, Gee *et al*. [25] [30] showed the skewness of the pressure waveform is probably a source phenomenon, not a propagation phenomenon (though Crighton [36] did find that propagation of a waveform with dispersion does generate non-zero skewness of the pressure waveform), whereas skewness of the first time derivative of the pressure waveform is related to propagation phenomena. Shepherd *et al*. [37] used numerical means to predict how various statistical measures, including the skewness of the pressure waveform and its first time derivative, evolve for an initially sinusoidal signal propagating without losses. Muhlestein and Gee [38] used a plane wave tube to estimate how the skewness of propagated pressure waveforms and their time derivatives evolve, but their analysis is incomplete. The skewness of a pressure waveform and the skewness of its first time derivative will be analyzed more carefully in this thesis.

1.6 Thesis Overview

The purpose of this thesis is to help establish an interpretation of various measures of the importance of nonlinearity in high-amplitude noise propagation. In order to accomplish this goal, analytical, numerical, and experimental analyses of these nonlinearity measures are presented and compared with measured jet noise data.

High-amplitude broadband noise propagation, such as the propagation of high-amplitude jet noise, can be extremely complicated, making it difficult to separate the propagation processes into distinguishable components. One of the most complicating factors in jet noise propagation is the geometry of the noise propagation. By using one-dimensional models and experiments (such as plane wave tube experiments [8] [31] [39] [40]), the effects of nonlinearity in noise propagation may be more easily discerned and then applied to more complicated systems like jet noise. The process of starting with simple models and working towards more complicated systems is the pattern used to organize this thesis.

Various analytical models of one-dimensional sound propagation are presented in Chapter 2. These propagation models are analyzed in terms of two measures of nonlinearity, the wave steepening factor and the derivative skewness, in Chapter 3. In addition, an analysis of the impact of finite sampling rates on the estimation of these measures of nonlinearity is presented. Chapter 4 contains an analysis of these nonlinearity measures using a numerical one-dimensional propagation model for various limiting and realistic cases.

The analytical and numerical analyses presented in Chapters 2 through 4 are used to interpret waveforms measured in a plane wave tube experiment in Chapter 5. These comparisons lead to insight into the interpretation of actual values of the nonlinearity measures being considered. Finally, the understanding obtained by the comparisons of the analytical, numerical, and experimental analyses are applied to interpreting measured full-scale jet noise waveforms in Chapter 6.

Chapter 2

Benchmark Cases

2.1 Introduction

Many models have been developed to describe the nonlinear propagation of sound in fluids. [41] The most notable model of one-dimensional propagation is the Burgers equation, [4] which describes the propagation of sound with thermoviscous absorption in addition to nonlinear effects, and may also be generalized to model arbitrary linear losses. Several important solutions to the Burgers equation, namely the Earnshaw, Fubini, Fay, and Khokhlov solutions, shed insights into the various limiting regimes of interest in nonlinear propagation, specifically of jet noise propagation. A derivation of the Burgers equation and most of the solutions presented here is found in Ref. [4] and Ref. [41], elements are repeated here for completeness. These solutions are used in Chapter 3 to evaluate the applicability of nonlinearity metrics prior to their application to numerical examples and experimental data.

2.2 Model Equations

2.2.1 Burgers Equation

The simplest way to model the propagation of a planar wave including thermoviscous losses and nonlinear effects is the Burgers equation. Following the notation of Ref. [4], the Burgers equation is written as

$$\frac{\partial p}{\partial x} - \frac{\delta}{2c_0^2}\frac{\partial^2 p}{\partial \tau^2} = \frac{\beta}{\rho_0 c_0^3} p \frac{\partial p}{\partial \tau}, \qquad (2.1)$$

where p is the acoustic pressure, x is the distance from the source, δ is a constant associated with acoustic absorption by the propagation medium, c_0 is small-signal sound speed, $\tau = t - x/c_0$ is the retarded time, β is the coefficient of nonlinearity, and ρ_0 is the ambient propagation medium density. The terms in Equation (2.1) represent, in order from left to right, lossless linear propagation, thermoviscous absorption, and quadratic nonlinear phenomena due to cumulative, oscillatory propagation.

Insights into the nature of the Burgers equation can be gained by examining the specific case of a sinusoidal source signal

$$p(x = 0, t) = p_0 \sin(\omega t), \qquad (2.2)$$

where p_0 is the source amplitude and ω is the angular frequency. In addition, because of the variety of scales that exhibit nonlinear phenomena, it is helpful to define a nondimensional distance

$$\bar{x} = \frac{\rho_0 c_0^3}{\beta \omega p_0} \qquad (2.3)$$

(which we will identify in Section 2.2.2.1 as the shock formation distance of an initially sinusoidal plane wave propagating without linear losses), a nondimensional pressure $P = p/p_0$, a nondimensional time $\theta = \omega\tau$, and a nondimensional distance $\sigma = x/\bar{x}$. The term “nondimensional” will generally be neglected when describing these quantities. Using these definitions, we may write the Burgers equation as

$$\frac{\partial P}{\partial \sigma} - \left(\frac{\delta \omega^2}{2c_0^2}\right)\bar{x}\frac{\partial^2 P}{\partial \theta^2} = P\frac{\partial P}{\partial \theta}, \tag{2.4}$$

and the nondimensional source function is written

$$P(\sigma = 0, \theta) = \sin(\theta). \tag{2.5}$$

The term in Equation (2.4) inside the parentheses is the thermoviscous attenuation coefficient α. If we further define $\Gamma = 1/\alpha\bar{x}$, we may further simplify Equation (2.4) to

$$\frac{\partial P}{\partial \sigma} - \frac{1}{\Gamma}\frac{\partial^2 P}{\partial \theta^2} = P\frac{\partial P}{\partial \theta}. \tag{2.6}$$

The parameter Γ is known as the Gol’dberg number and can be qualitatively described as the relative importance of nonlinearity for a given source strength and propagation. To illustrate this aspect mathematically, we define the absorption length $l_\alpha = 1/\alpha$ so that the Gol’dberg number may be written as

$$\Gamma = \frac{l_\alpha}{\bar{x}}. \tag{2.7}$$

Thus, large values of Γ suggests that $\bar{x} < l_\alpha$, and nonlinear effects happen on a shorter distance scale than absorptive effects. Similarly, if $l_\alpha < \bar{x}$ then $\Gamma < 1$ and the absorptive processes occur much more rapidly than nonlinear processes. Thus, large values of the Gol’dberg number suggest that nonlinearity dominate absorptive phenomena, and small values of the Gol’dberg number suggest that linear absorption dominates nonlinearity in propagation.

In the limit that Γ → ∞, nonlinear effects dominate thermoviscous losses (for arbitrary nondimensional source functions), and the inviscid Burgers equation is obtained:

$$\frac{\partial P}{\partial \sigma} = P\frac{\partial P}{\partial \theta}. \tag{2.8}$$

The inciscid Burgers equation is useful in understanding nonlinear processes over distances much less than l_α and for very high-amplitude signals, and will be the primary propagation model used in the Section 2.2.2. The Burgers equation as found in Equation (2.6) will be the primary propagation model used in Section 2.2.3.

2.2.2 Propagation without Linear Losses

It is often difficult to separate the effects of nonlinearity in measured waveforms from linear losses such as thermoviscous absorption, molecular relaxation, and boundary layer effects. In order to gain a qualitative understanding of general nonlinear propagation effects and a quantitative understanding of very high-amplitude propagation phenomena, we consider phenomena of waves propagating without the effects of linear losses in this section.

2.2.2.1 Earnshaw Solution to the Inviscid Burgers Equation

The method of characteristics may be used to directly solve the inviscid Burgers equation in an implicit form. This solution, called the Earnshaw solution, can be written

$$\begin{gathered} P = f(\phi) \\ \phi = \theta + \sigma P\,' \end{gathered} \tag{2.9}$$

where ϕ has been called the Earnshaw phase variable. [4] The Earnshaw solution may be interpreted as distorting the times of arrival of the initial waveform, represented by the Earnshaw phase variable, but not modifying the pressure values, $f(\phi)$. This interpretation may also be seen by writing the pressure waveform at a specific location parametrically. For instance, at the source ($\sigma = 0$), the pressure waveform may be described as $\big(\theta, f(\theta)\big)$, where the first value is the time of arrival and the second value is the pressure at the time of arrival. At a normalized distance σ from the source, the waveform may be described as $\big(\theta - \sigma f(\theta), f(\theta)\big)$. If we define θ' as the time of arrival of the pressure $f(\theta)$, then we find that

$$\theta' = \theta - \sigma f(\theta). \tag{2.10}$$

Equation (2.10) describes the arrival times of the pressure initially at θ propagated to σ as long as the times of arrival monotonically increase with increasing θ. When this is not the case, a shock has formed in the waveform and the Earnshaw solution no longer independently describes the propagation; in such situations more equations are needed to model the shock propagation. [4] For the case of the initially sinusoidal signal, described in Equation (2.5), the distance at which shocks first form is $\sigma = 1$, which corresponds to $x = \bar{x}$. For this reason, $\bar{x}$ is known as the shock formation distance.

Of particular use in Chapter 3 is the time-derivative of the pressure waveform at a given location written parametrically. In order to determine the parametric form of the time-derivative, consider two points of the pressure waveform,

$$\big(\theta_1 - \sigma f_1(\theta), f_1(\theta)\big) \tag{2.11}$$

and

$$\big(\theta_2 - \sigma f_2(\theta), f_2(\theta)\big) \tag{2.12}$$

where $\theta_1 < \theta_2$. We define $\Delta\theta = \theta_2 - \theta_1$ and $\Delta f(\theta) = f_2(\theta) - f_1(\theta)$. At different values of σ $\Delta f(\theta)$ does not vary, but $\Delta\theta$ does vary. In particular,

$$\Delta\theta' = \theta_2' - \theta_1' = \big(\theta_2 - \sigma f_2(\theta)\big) - \big(\theta_1 - \sigma f_1(\theta)\big) \tag{2.13}$$

$$= \Delta\theta - \sigma\Delta f(\theta) = \Delta\theta\left(1 - \sigma\frac{\Delta f(\theta)}{\Delta\theta}\right). \tag{2.14}$$

Then we may write the time-derivative that arrives at $(\theta_1' + \theta_2')/2$ as

$$\frac{\Delta f(\theta)}{\Delta\theta'} = \frac{1}{1-\sigma\frac{\Delta f(\theta)}{\Delta\theta}}\frac{\Delta f(\theta)}{\Delta\theta}. \tag{2.15}$$

In the limit that $\theta_2 \to \theta_1 = \theta$, the ratio of differences becomes a derivative:

$$\frac{d}{d\theta'}f(\theta) = \frac{1}{1-\sigma\frac{d}{\partial\theta}f(\theta)}\frac{d}{d\theta}f(\theta). \tag{2.16}$$

Since θ_1 and θ_2 were arbitrary, Equation (2.16) is true for any θ. Thus, the parametric description of the time-derivative of the pressure waveform is

$$\left(\theta - \sigma f(\theta), \frac{1}{1-\sigma\frac{d}{\partial\theta}f(\theta)}\frac{d}{d\theta}f(\theta)\right). \tag{2.17}$$

For the particular case $f(\theta) = \sin(\theta)$, we find that Equation (2.17) can be written as

$$\left(\theta - \sigma\sin(\theta), \frac{\cos(\theta)}{1-\sigma\cos(\theta)}\right). \tag{2.18}$$

The both terms of the parameterization of the time-derivative of the pressure waveform given in Equation (2.18) are dependent on σ, despite the fact that only the left-hand term of the parameterization of the pressure waveform itself is dependent on σ. The range dependent time-derivative amplitude is due to the fact that modifying times of arrival also modifies the instantaneous pressure slope.

2.2.2.2 Fubini Solution

While the Earnshaw solution is useful in certain circumstances (such as computational schemes and calculating WSF values, as in Section 3.2.1), it is sometimes desirable to have an explicit function to describe the propagation of a waveform without linear losses. For example, it is much easier to find the mean pressure of a portion of a waveform with an explicit expression of waveform than with a parametric expression. One way to find an explicit function is to eliminate the Earnshaw phase variable from the Earnshaw solution. While this process may not be possible in general, an explicit form of an initially sinusoidal signal propagating without linear losses prior to the formation of shocks was found, and is called the Fubini solution. [4] The Fubini solution is written as the infinite series

$$P = \sum_{n=1}^{\infty} \frac{2}{n\sigma} J_n(n\sigma)\sin(n\theta). \tag{2.19}$$

Just as the Earnshaw solution is only valid up to the shock formation distance, the Fubini solution is only valid for the pre-shock propagation regime, i.e. $\sigma < 1$. The time derivative of the Fubini solution is given as

$$\frac{\partial P}{\partial \theta} = \sum_{n=1}^{\infty} \frac{2}{\sigma} J_n(n\sigma)\cos(n\theta). \tag{2.20}$$

2.2.2.3 Blackstock Bridging Function

Although the Earnshaw and Fubini solutions are limited to distances less than or equal to a shock formation distance, it is beneficial to consider an analytic solution that is valid for all σ. For the case of an initially sinusoidal plane wave propagating without linear losses, a Fourier series representation of the waveform evolution that is valid for all σ was introduced by Blackstock. [42] The Blackstock bridging function is given as

$$P = \sum_{n=1}^{\infty} B_n \sin(n\theta), \tag{2.21}$$

where

$$B_n = \frac{2}{n\pi\sigma}\left[\Phi_{sh} + \int_{\Phi_{sh}}^{\pi} \cos(n[\Phi - \sigma\sin\Phi])\, d\Phi\right]. \tag{2.22}$$

The variable Φ_{sh} is associated with the presence of a shock, and is the solution to the transcendental equation

$$\Phi_{sh} = \sigma \sin \Phi_{sh}\,, \quad 0 \leq \Phi_{sh} < \pi. \tag{2.23}$$

As the name implies, the Blackstock bridging function connects two simpler analytical solutions. For $\sigma < 1$ the Blackstock bridging function reduces to the Fubini solution, and for $\sigma > 3$ the Blackstock bridging function may be approximated by a sawtooth wave, of the form

$$P = \frac{2}{1+\sigma} \sum_{n=1}^{\infty} \frac{1}{n} \sin(n\theta). \tag{2.24}$$

Equation (2.24) may also be written as

$$P = \frac{2\pi}{1+\sigma} \left(\text{floor}\left(\frac{\theta}{2\pi}\right) - \frac{\theta}{2\pi} + \frac{1}{2} \right). \tag{2.25}$$

The Blackstock bridging function is particularly useful when comparing harmonics, since the Fourier series representation allows for the harmonic amplitudes to be obtained by inspection.

2.2.2.4 Generalized Shock Formation Distance

While the regime over which each of the analytical solutions described above (Fubini, Earnshaw, and Blackstock bridging function) is valid is based on the shock formation distance, it is important to determine good representations of the shock formation distance for other types of waves. As mentioned above, the shock formation distance defined in Equation (2.3) is only valid for initially sinusoidal plane waves propagating without linear losses. For plane waves that propagate without linear losses, the general shock formation distance is given as

$$\bar{x} = \frac{\rho_0 c_0^3}{\beta f'_{max}}, \tag{2.26}$$

where f'_{max} is the greatest first time-derivative value in the source pressure waveform. [4] If we assume the source waveform is sinusoidal, then we find that $f'_{max} = \omega p_0$, and Equation (2.3) is obtained.

The question of how to characterize nonlinear distortion in noise waveforms is a non-trivial one. Due to the fact that each waveform is inherently unique, two noise waveforms with similar statistics may have significantly different shock formation distances. One way to accommodate this is to define a characteristic nonlinear distortion length to be used in place of the shock formation distance. In this thesis, we will use

$$\bar{x}_N = \frac{\rho_0 c_0^3}{\beta(2\pi f_c)\left(\sqrt{2}p_{\mathrm{rms}}\right)} \tag{2.27}$$

as the characteristic nonlinear distortion length for noise, where f_c is a characteristic frequency and p_{rms} is the root-mean-square pressure (or pressure standard deviation) of the waveform. Equation (2.27) is very similar to the nonlinear distortion length defined by Gubatov and Rudenko, [43] with the difference being the inclusion of the factor of $\sqrt{2}$. The inclusion of this factor gives the characteristic nonlinear distortion length the property that it will reduce to the shock formation distance of an initially sinusoidal plane wave in the limit that the noise bandwidth goes to zero.

In general, the shock formation distance for waves propagating with arbitrary diffraction is not known. However, the shock formation distances for spherically and cylindrically spreading waves propagating without linear losses are known, in addition to planar waves. The spherical and cylindrical shock formation distances have been found in terms of the planar shock formation distance found in Equation (2.26). The spherical shock formation distance is given as

$$\bar{r} = r_0 e^{\pm\bar{x}/r_0}, \tag{2.28}$$

where r_0 is a distance from the source where the waveform is known, the positive sign indicates diverging waves, the negative sign indicates converging waves, and $\bar{x}$ is the shock formation distance defined in Equation (2.26) (or, for noise, the nonlinear distortion length defined in Equation (2.27)) of the pressure wave at r_0. For reference in Chapter 4, we will define a nondimensional radius from a spherical source

$$\sigma_s = \frac{r}{\bar{r}}, \tag{2.29}$$

where r is the distance from the source.

2.2.3 Propagation with Thermoviscous Losses

While much can be learned about very high-amplitude sound propagation by considering the previous cases that exclude linear losses, the next step is to see what parallels can be formed when linear losses are included.

2.2.3.1 Linear Dissipative Processes

Due to the availability of analytical solutions to propagation according to the Burgers equation in Equation (2.1), such as the Mendousse, Fay, and Khokhlov solutions, the effects of thermoviscous absorption on propagating waves are better known than the other absorptive effects. However, realistic atmospheric absorption models include the effects of molecular relaxation for both oxygen and nitrogen, and propagation in ducts also includes boundary layer losses.

While the physical phenomena associated with the various linear absorptive processes are unique, they may each be modeled fairly simply in the frequency domain. The absorption coefficient associated with thermoviscous absorption is proportional to the square of the frequency, and the absorption coefficient associated with boundary layer losses is proportional to the square root of frequency. The absorption coefficients associated with molecular relaxation are of the form

$$\alpha_{\text{relaxation}} = \frac{Af^2}{f_0^2 + f^2}, \tag{2.30}$$

where A and f_0 are constants associated with the specific molecule being modeled. Absorption due to any combination of absorptive processes is modeled by an absorption coefficient which is the sum of the constituent absorption coefficients. For example, the absorption coefficient associated with plane wave tube propagation includes thermoviscous and boundary layer losses, in addition to primarily oxygen and nitrogen related molecular relaxation. Thus, the plane wave tube absorption coefficient would be

$$\alpha_{\text{PWT}} = \alpha_{\text{TV}} + \alpha_{O,\text{rel}} + \alpha_{N,\text{rel}} + \alpha_{\text{BL}}. \tag{2.31}$$

It should be noted that the atmospheric absorption coefficient is the same as the plane wave tube absorption coefficient if the boundary layer losses are neglected.

In addition to absorptive effects, the boundary layer and relaxational losses include dispersion, or a frequency dependent sound speed. Boundary layer dispersion scales with the square root of frequency, the same as boundary layer absorption. The dispersion due to molecular relaxation is directly proportional to the frequency. Dispersive phenomena are accounted for by the imaginary part of the absorption coefficients.

A plot of the real part of the absorption coefficients for thermoviscous, boundary layer, and oxygen and nitrogen molecular relaxation losses, as well as atmospheric and plane wave tube absorption is shown in Figure 2.1. The atmospheric conditions used to generate the plot are given in the title of the plot, and a is the radius of the plane wave tube of circular cross-section (for the boundary layer losses). Notice that the absorption coefficients associated with boundary layer losses are significantly larger than any of the other absorptive processes until near 10 kHz, and is the largest contributor to plane wave tube absorption until 140 kHz, after which thermoviscous absorption dominates.

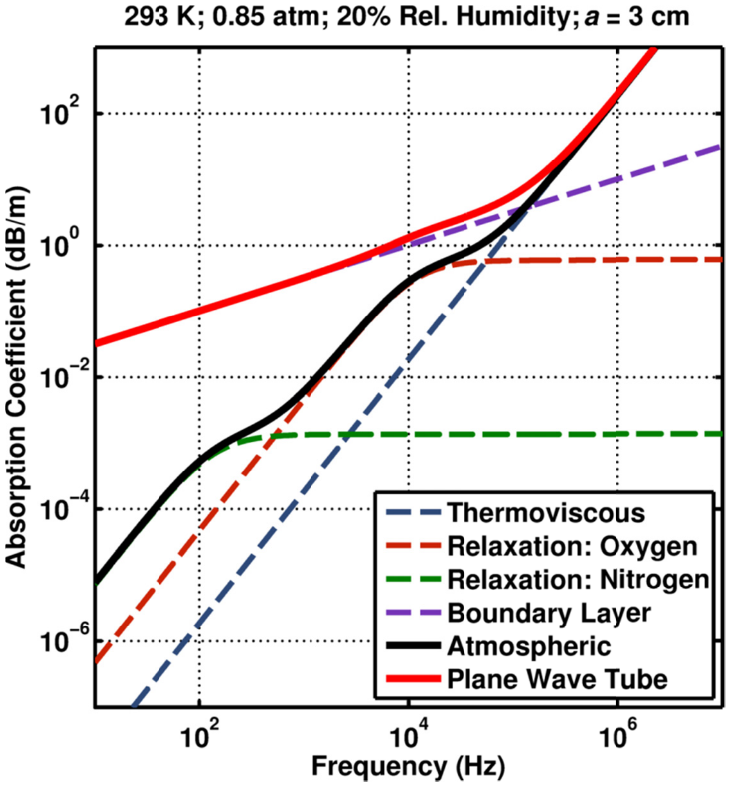

Figure 2.1. A plot of the real part of the absorption coefficients associated with thermoviscous, molecular relaxational, and boundary layer losses, as well as the real part of the absorption coefficients due to atmospheric propagation and propagation in a plane wave tube.

The fact that realistic absorption coefficients increase with the square of frequency for very large frequencies suggests that true discontinuities will never form in measured waveforms. While a full discussion of dissipative and dispersive phenomena and how they relate to nonlinear propagation is beyond the scope of this thesis, more information may be found in Ref. [10], Ref. [44], and Ref. [45].

2.2.3.2 Generalized Shock Formation Distance

Since realistic linear losses preclude the existence of true discontinuities in a waveform, determining a “lossy” shock formation distance is difficult. One method, used by Pernet and Payne, [2] is to assume that an initially sinusoidal plane wave will decay exponentially with propagation at a uniform rate determined by the fundamental frequency. This case is essentially assuming that there is a uniform absorption coefficient for all frequencies. Since a waveform that decays uniformly over all frequencies may still generate true discontinuities, the lossy shock formation distance may still be precisely defined. The distance at which such a wave will generate a shock is

$$\bar{x}_\alpha = \frac{1}{\alpha}\ln\frac{1}{1-\alpha\bar{x}}, \tag{2.32}$$

where α is the absorption coefficient of the fundamental frequency and $\bar{x}$ is the shock formation distance of the waveform assuming no linear losses. In terms of $\sigma = x/\bar{x}$ and the Gol'dberg number $\Gamma = 1/\alpha\bar{x}$, the "lossy" shock formation distance may be written

$$\sigma|_{x=\bar{x}_\alpha} = \Gamma\ln\frac{1}{1-1/\Gamma}. \tag{2.33}$$

Note that the Gol'dberg number is usually defined for the thermoviscous absorption coefficient, whereas Equation (2.33) makes use of a uniform absorption coefficient. According to Equation (2.33), shocks do not form for $\Gamma < 1$, and for $\Gamma = 1$, a shock forms at infinity. Under the assumption of a uniform absorption coefficient for all frequencies that is behind Equation (2.33) the lowest starting amplitude of an initially 1500 Hz sinusoidal plane wave in air that will generate shocks is about 109 dB re 20μPa at an ambient pressure of 1 atm. Since realistic absorption processes, such as atmospheric or thermoviscous absorption, predict that absorption will increase for higher frequencies, Equation (2.33) will underestimate the distance at which shocks will form in realistic cases.

For large Γ, the "lossy" shock formation distance may be approximated as

$$\sigma|_{x=\bar{x}_\alpha} \approx 1 + \frac{1}{2\Gamma}. \tag{2.34}$$

The amplitudes and characteristic frequencies associated with jet noise suggest Γ values between 10 and 100, [24] which would imply a "lossy" shock formation distance (assuming planar propagation) between 1.005 and 1.05 times the shock formation distance assuming propagation with no linear losses. Since this correction factor is less than 5% of the lossless shock formation distance, all of the analyses presented in this thesis will make reference to the lossless shock formation distance or characteristic nonlinear distortion length. It should be noted, however, that since this theory was based on an absorption coefficient that significantly underestimates the high-frequency absorption, it is likely that these "lossy" shock formation distances are also underestimated.

2.2.3.3 Mendousse Solution to the Burgers Equation

Returning to the Burgers equation as it appears in Equation (2.6), which includes thermoviscous absorption, a general solution for an initially sinusoidal wave is the Mendousse solution, written as

$$P = \frac{4}{\Gamma}\frac{\sum_{n=1}^{\infty}(-1)^{n+1} n I_n(\Gamma/2) e^{-n^2\sigma/\Gamma}\sin(n\theta)}{I_0(\Gamma/2) + 2\sum_{n=1}^{\infty}(-1)^{n} I_n(\Gamma/2) e^{-n^2\sigma/\Gamma}\cos(n\theta)}, \tag{2.35}$$

where I_n is the n^{th} modified Bessel function of the first kind. The Mendousse solution is only limited to positive values of σ, meaning that the entire propagation of a waveform undergoing thermoviscous absorption may be described by the Mendousse solution. However, the Mendousse solution will not be considered directly in this thesis, due to the difficulty of working with a solution in terms of a ratio of infinite series. Because the Mendousse solution is impractical for the present work, two approximations of it are instead considered that are not as general but which shed light on important propagation regimes.

2.2.3.4 Fay Solution

For $\Gamma \gg 1$ and $\sigma > 3$ – that is, for waveforms with very large amplitudes undergoing thermoviscous absorption in the sawtooth regime of propagation – the Mendousse solution may be approximated by

$$P = \frac{2}{\Gamma} \sum_{n=1}^{\infty} \frac{\sin(n\theta)}{\sinh\left(n \frac{\sigma+1}{\Gamma}\right)}, \tag{2.36}$$

which is called the Fay solution.

Due to its recurring appearance in the derivations in this chapter, we will define the variable

$$\psi = \frac{\sigma+1}{\Gamma}. \tag{2.37}$$

Since $\sigma/\Gamma = (x/\bar{x})/(1/\alpha\bar{x}) = \alpha x$, we will call ψ a nondimensional absorption distance, or just an absorption distance. In this thesis, the absorption distance will always be limited by the constraint $\sigma > 3$, such that $\psi \ll 1$ implies very strong shocks present in the waveform. Values of the absorption distance much larger than one indicate the propagation regime known as "old-age", where shocks have unsteepened significantly.

The Fay solution in Equation (2.37) may be written in terms of the absorption distance as

$$P = \frac{2}{\Gamma} \sum_{n=1}^{\infty} \frac{\sin(n\theta)}{\sinh(n\psi)}, \tag{2.38}$$

The time-derivative of the Fay solution is

$$\frac{\partial P}{\partial \theta} = \frac{2}{\Gamma} \sum_{n=1}^{\infty} \frac{n\cos(n\theta)}{\sinh(n\psi)}. \tag{2.39}$$

In the limit that ψ becomes large, the Fay solution may be approximated as

$$P \approx \frac{4}{\Gamma} \sum_{n=1}^{\infty} e^{-n\psi} \sin(n\theta), \tag{2.40}$$

With a time-derivative of

$$\frac{\partial P}{\partial \theta} \approx \frac{4}{\Gamma}\sum_{n=1}^{\infty} n e^{-n\psi}\cos(n\theta). \tag{2.41}$$

The Fay solution and its asymptotic form provide a way to consider the propagation of initially sinusoidal plane waves through the sawtooth and old-age propagation regimes that is easier than the Mendousse solution. However, the Fay solution is still written in terms of an infinite series. It is difficult to analyze certain nonlinearity measures, such as the wave steepening factor, of waveforms expressed as infinite series.

2.2.3.5 Khokhlov Solution

By approximating an integral early in the derivation of the Mendousse solution with the saddle-point method, another solution to the Burgers equation may be found:

$$P = \frac{1}{1+\sigma}\left[-\theta + \pi\tanh\frac{\pi}{2\psi}\theta\right], \qquad -\pi < \theta < \pi \tag{2.42}$$

which is called the Khokhlov solution. The Khokhlov solution is only valid for $3 < \sigma < \Gamma$ ($\psi < 1$, for large Γ; $0.4 < \psi < 1.1$ for $\Gamma = 10$), and describes only one cycle of the waveform. It is important to note that the range of applicable distances corresponds to only the sawtooth propagation regime. However, the Khokhlov solution is not represented by an infinite series, making it easier to manipulate analytically than the Fay solution. The time-derivative of the Khokhlov solution is

$$\frac{\partial P}{\partial \theta} = \frac{1}{1+\sigma}\left[-1 + \frac{\pi^2}{2\psi}\tanh\frac{\pi}{2\psi}\theta\right]. \tag{2.43}$$

2.3 Summary

The Burgers equation describes the one-dimensional propagation of pressure waves including thermoviscous absorption and quadratic nonlinear phenomena. When absorption is negligible, the evolution of an initially sinusoidal wave may be described by the Earnshaw and Fubini solutions prior to shock formation, called the pre-shock propagation regime. Once shocks form the Earnshaw and Fubini solutions cease to be complete, and other mathematical relations must be incorporated. The Blackstock bridging function may be used to model the propagation of an initially sinusoidal signal without linear losses (such as thermoviscous losses) to any distance from the source, and is particularly helpful in the sawtooth propagation regime (starting about three times the shock formation distance from the source).

For initially sinusoidal signals propagating with thermoviscous absorption, the Mendousse solution may be used to describe the evolution of the wave to any distance from the source. However, due to the complicated nature of the Mendousse solution, approximations are useful. For propagation from the sawtooth regime (starting about three times the shock formation distance from the source), the Fay solution is a good approximation. Another approximation that is sometimes useful is the Khokhlov solution, which is only valid between the distances that the sawtooth regime starts and that absorption begins to dominate again. The region where linear absorption dominates is called the old-age propagation regime. Thus, the Khokhlov solution is not valid in the old-age propagation regime, and either the Fay or Mendousse solution must be used to model the evolution of the waveform.

Chapter 3

Time-Domain Measures of Nonlinearity

3.1 Introduction

Many techniques for studying propagating noise fields must assume that the noise propagates in a linear fashion. This linear assumption is not strictly true, and is not likely to be a good approximation for high-amplitude noise propagation. In this chapter, two metrics for characterizing the importance of nonlinearity in jet noise are defined and their uses and limitations are discussed. Specifically, the wave steepening factor and skewness estimates are explored. Then several analytical forms of these measures, derived from the limiting cases described in Chapter 2, are presented. Finally, a discussion of the effects of discrete sampling of continuous waveforms on each of the measures of nonlinearity is presented.

3.1.1 Wave Steepening Factor

In 1982, Gallagher [18] defined the wave steepening factor (WSF) as the ratio of the magnitude of the average negative pressure time-derivative to the average positive pressure time-derivative, or in mathematical form,

$$\frac{|E[\dot{p}^-]|}{E[\dot{p}^+]} \tag{3.1}$$

where $E[\cdot]$ is the expectation value (mean) of the argument, $\dot{p}^{-}$ represents the negative pressure time-derivatives, and $\dot{p}^{+}$ represents the positive pressure time-derivatives. The WSF is a single-number characterization of a waveform, but also benefits from the fact that classification of and knowledge of the location of shocks in the waveform is not necessary. However, as with all single-number characterizations, the WSF does not include details concerning individual shocks or other pressure rises. In particular, the WSF is not sensitive to whether waveforms contain infrequent shocks (as is often the case for skewed waveforms such as the measured waveforms of jet noise; skewness will be discussed in Section 3.1.2) or if a waveform has no shocks, but does have significant waveform distortion due to nonlinear effects (such as a nonlinearly propagated sine wave before the shock formation distance). The WSF was discussed in the study of noise radiating from model-scale jets with low to moderate Reynolds number by Gallagher [18] and, more recently, reported by Baars *et al*. [28] in a study of noise radiating from model-scale jets. Both Gallagher and Baars et al. considered the WSF of a given waveform in a qualitative manner and did not give a physical interpretation of specific values, except to note that a sawtooth function has a WSF value of zero and that both sine waves and Gaussian noise have WSF values of unity.

3.1.2 Derivative Skewness

The skewness of a random variable x with mean value of zero, denoted in this report as $\mathrm{Sk}\{x\}$, is a measure of the asymmetry of the statistical distribution of x. The skewness is defined as

$$\mathrm{Sk}\{x\} = \frac{E[x^3]}{E[x^2]^{\frac{3}{2}}}. \tag{3.2}$$

It should be noted that the skewness of a sine wave and of noise with Gaussian statistics have skewness values of identically zero, as do the derivatives of these waveforms.

McInerny *et al*. [33] [46] [47] and Gee *et al*. [13] have suggested that the skewness of the first time-derivative of the pressure amplitudes (hereafter referred to as the derivative skewness) may be a more appropriate measure than the skewness of the pressure waveform (which was suggested by Ffowcs Williams *et al*. [34]) to characterize crackle, since crackle has been associated with acoustic shocks which likely develop via nonlinear propagation distortion of waveforms. [35] Shepherd *et al*. [37] used numerical means to predict the evolution of the derivative skewness for an initially sinusoidal wave propagating without linear losses. Muhlestein and Gee [38] estimated the derivative skewness for waveforms measured in a plane wave tube, and found similar evolution to that found by Shepherd *et al*. [37] These studies will be considered in more depth later. However, no analysis of the effects of finite sampling rates on the estimation of the pressure or derivative skewness (or the WSF) has been published to date.

3.2 Analytical Treatment of Benchmark Cases

Notwithstanding the fact that some limiting cases have been calculated, the interpretation of the two measures defined in Section 3.1 is not well understood. For example, Gallagher [18] stated that the WSF is “approximately unity for a pure sinusoidal wave, and … [is] close to zero for a pure N-type waveform”, but no mention is made of the WSF evolution for an initially sinusoidal wave as it distorts and generates shocks. (It should be noted that Baars *et al*. stated that the WSF of a sinusoid is identically one, and is identically zero for a sawtooth wave, which is a pure N-type waveform.) The lack of interpretation is similar for skewness estimates of waveforms after shocks form.

In this section, measures of nonlinearity for several benchmark cases are studied analytically and discussed with an emphasis on how the measures evolve over propagation. The WSF and skewness estimates of the planar, initially sinusoidal signal with and without thermoviscous losses are calculated using the solutions discussed in Chapter 2. Then the effects of finite sampling rates on the estimation of these nonlinearity metrics are discussed.

3.2.1 Wave Steepening Factor

3.2.1.1 Earnshaw Solution

In order to calculate the wave steepening factor (WSF) of a waveform the times of arrival of the pressure extrema must be known. For the Earnshaw solution assuming a sinusoidal source signal, the exact times of arrival of these extrema at $\sigma = 0$ are $\theta = n\pi + \pi/2$, for all $n \in \mathbb{Z}$, and the pressure maxima arrive at $\theta = 2n\pi + \pi/2$ and the pressure minima arrive at $\theta = 2n\pi - \pi/2$. Due to normalization, the pressure maxima have a value of one and the pressure minima have a value of negative one. Then, based on Equation (2.10), we find that the time of arrival of the n^{th} pressure maximum at a distance of σ is

$$\Theta_{\mathrm{max},n} = 2n\pi + \frac{\pi}{2} - \sigma, \tag{3.3}$$

and the time of arrival of the n^{th} pressure minimum at a distance of σ is

$$\Theta_{\mathrm{min},n} = 2n\pi - \frac{\pi}{2} + \sigma. \tag{3.4}$$

Due to the periodicity of the initial sine wave, calculating the WSF of a single period will accurately represent the entire waveform. Therefore, we consider the waveform between $\Theta_{\mathrm{max},0}$ and $\Theta_{\mathrm{max},1}$, which includes $\Theta_{\mathrm{min},1}$. The expectation value of the positive slopes is then the mean slope between $\Theta_{\mathrm{min},1}$ and $\Theta_{\mathrm{max},1}$, and the expectation value of the negative slopes is the mean slope between $\Theta_{\mathrm{max},0}$ and $\Theta_{\mathrm{min},1}$.

The average slope of a function $f(x)$ between two points, say, a and b, can be written as

$$E\left[\frac{df}{dx}\right] = \frac{1}{b-a}\int_a^b \frac{df}{dx}dx = \frac{f(b) - f(a)}{b-a}, \tag{3.5}$$

where the final equality is a result of the fundamental theorem of calculus. Therefore, we find that

$$E[\dot{P}^{+}] = \frac{P(\Theta_{\max,1}) - P(\Theta_{\min,1})}{\Theta_{\max,1} - \Theta_{\min,1}} = \frac{2}{\pi - 2\sigma}, \tag{3.6}$$

and

$$E[\dot{P}^{-}] = \frac{P(\Theta_{\min,1}) - P(\Theta_{\max,0})}{\Theta_{\min,1} - \Theta_{\max,0}} = \frac{-2}{\pi + 2\sigma}. \tag{3.7}$$

Thus, we find that the WSF based on the Earnshaw solution is

$$\mathrm{WSF} = -\frac{\frac{-2}{\pi + 2\sigma}}{\frac{2}{\pi - 2\sigma}} = \frac{\pi - 2\sigma}{\pi + 2\sigma}, \qquad \sigma \leq \frac{\pi}{2}. \tag{3.8}$$

For values of $\sigma > \pi/2$, we note that the extrema occur almost simultaneously. In fact, we could write

$$E[\dot{P}^{+}] = \lim_{\Delta\theta \to 0} \frac{P(\Delta\theta/2) - P(-\Delta\theta/2)}{\Delta\theta}, \tag{3.9}$$

which diverges. However, $E[\dot{P}^{-}]$ can be shown to be finite, which indicates that the WSF for $\sigma > \pi/2$ is zero. Thus we may write

$$\mathrm{WSF} = \begin{cases} \dfrac{\pi - 2\sigma}{\pi + 2\sigma} & \sigma < \dfrac{\pi}{2} \\ 0 & \sigma \geq \dfrac{\pi}{2} \end{cases} \tag{3.10}$$

Note the importance of the value $\pi/2$ in Equation (3.10). Since the maxima and minima in the initial waveform always have a time difference of π, we may interpret the distance $\sigma = \pi/2$ as the distance at which the maxima and minima collocate.

It is interesting to note that the amplitudes of the maxima and minima cancelled in the calculation of the WSF for the Earnshaw solution. In general, for periodic, zero-mean functions with a single peak and trough per period, this will always happen, since

$$\begin{aligned} P\left(\Theta_{\max,n}\right) &= P\left(\Theta_{\max,n+1}\right) \\ P\left(\Theta_{\min,n}\right) &= P\left(\Theta_{\min,n+1}\right) \end{aligned} \tag{3.11}$$

for all n. Thus, the WSF of a periodic, zero-mean function is

$$\mathrm{WSF} = \frac{\Theta_{\max,1} - \Theta_{\min,1}}{\Theta_{\min,1} - \Theta_{\max,0}} \tag{3.12}$$

Which is just the time it takes for the pressure to go from a minimum to the next maximum (or the rise time) over the time it takes for the pressure to go from a maximum to the next minimum (or the fall time).

In order to benchmark Equation (3.8), we will compare it with the Blackstock bridging function, defined in Section 2.2.2.3. Since the Blackstock bridging function is expressed as an infinite Fourier series which diverges for $\sigma \geq 1$, the theory and analytical formulation are not expected to match for values of σ close to or above unity.

The calculations of the analytic WSF based on the Earnshaw solution and the WSF based on the Blackstock bridging function are shown in Figure 3.1, below. The Blackstock bridging function was calculated with Equation (2.21), using 10,000 terms, and a single period was calculated using 10,000 samples.

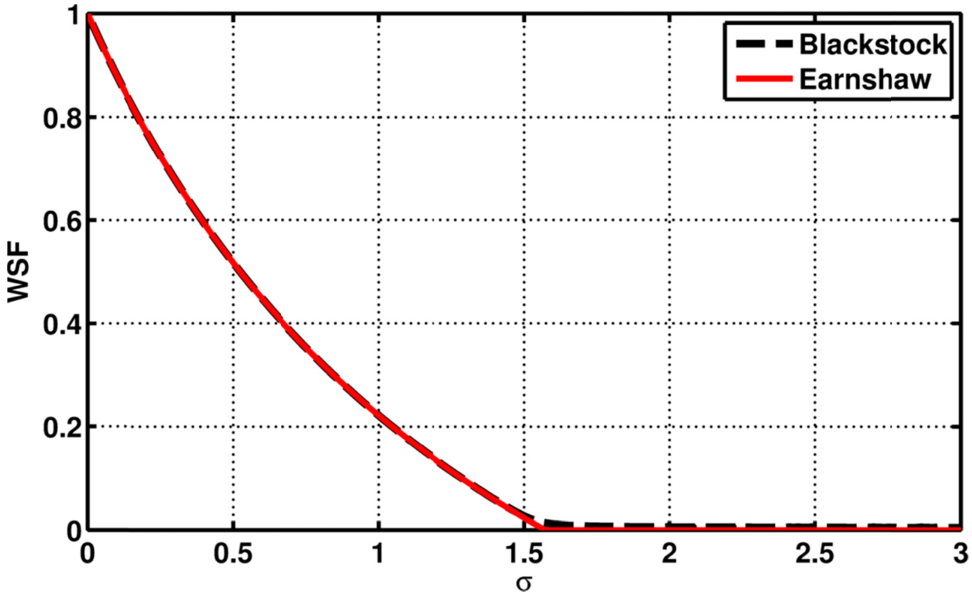

Figure 3.1. Calculations of the wave steepening factor (WSF) using the Blackstock bridging function and the Earnshaw solution.

As can be seen in Figure 3.1, the analytical formulation of the WSF from the Earnshaw solution (red line) follows the estimate of the WSF from the Blackstock bridging function (dashed, black line) very closely up to $\sigma = 1.5$. For $\sigma > 1.5$, the estimates based on the Blackstock bridging function do not quite reach as low values as the estimates based on the Earnshaw. Since the Blackstock bridging function was truncated and the Earnshaw solution is exact, it is likely that the WSF values based on the Earnshaw solution are more accurate.

A qualitative description of a waveform based on the WSF is facilitated by examining Figure 3.1. Notice that the WSF values of both the Earnshaw solution and the Blackstock bridging function are about 0.75 at $\sigma = 0.2$. Then, if we assume that the waveform has not been significantly deformed for $\sigma < 0.2$, then we conclude that in the case of no linear losses that a WSF value above about 0.75 may be considered to be a high WSF value (corresponding to low/no shock content). Similarly, if we assume that the waveform has been significantly deformed for $\sigma > 0.9$, then we conclude that a WSF value below about 0.25 may be considered to be a low WSF value, which indicates significant nonlinear distortion. One may be tempted to say that, since the slope of a shock is infinite, the mean positive slope for $\sigma > 1$ (propagation past the shock formation distance) would also be infinite. However, since the shock also has zero temporal extent (it starts and ends at the same time), the effect of the shock on the mean positive slope is somewhat reduced. All positive slopes other than the shock are gone for $\sigma > \pi/2$, and so the WSF becomes zero in this region. It should be noted that finite sampling rates will force the estimate of the rise time of the shock to be positive. Therefore, the estimate of the WSF of a discretely sampled waveform will never be zero.

3.2.1.2 Khokhlov Solution

The Khokhlov solution is a solution to the Burgers equation given in Equation (2.6), which includes the effects of thermoviscous absorption, given a sinusoidal source signal, and is valid for $3 < \sigma < \Gamma$, or, in physical distances, $3\bar{x} < x < l_{\alpha}$. The reason that the Khokhlov solution is used in this section rather than the Fay solution, which is valid for all $\sigma > 3$ is that, as will be seen below, the calculation of the WSF requires knowledge of the pressure extrema in a waveform. Since the Fay solution is written in terms of a Fourier series, it is not as conducive to finding the pressure extrema as the Khokhlov solution.

As shown in Section 3.2.1.1 the WSF of a periodic, zero-mean function can be determined by knowing the rise and fall times of the function. Since the Khokhlov solution, presented in Section 2.2.3.5, describes a periodic, zero-mean waveform, the WSF may be obtained once the rise and fall times are found. Note that the difference between the time of arrival of the pressure extrema in Equation (2.42) is the rise time. These extrema may be found by setting the time-derivative of the pressure waveform (Equation (2.43)) to zero and solving for θ. In particular,

$$\frac{1}{1+\sigma}\left[-1+\pi\left(1-\tanh^2\frac{\pi}{2}\frac{\theta}{\psi}\right)\frac{\pi}{2}\frac{1}{\psi}\right]=0 \tag{3.13}$$

$$\Rightarrow \tanh^2\frac{\pi}{2}\frac{\theta}{\psi}=1-\frac{2}{\pi^2}\psi \tag{3.14}$$

$$\Rightarrow \theta = \frac{2}{\pi}\psi \tanh^{-1} \pm \sqrt{1-\frac{2}{\pi^2}\psi} = \pm\frac{2}{\pi}\psi \tanh^{-1}\sqrt{1-\frac{2}{\pi^2}\psi}. \tag{3.15}$$

Thus, we obtain the times of arrival of the two extrema:

$$\Theta_{\text{min}} = -\frac{2}{\pi}\psi \tanh^{-1}\sqrt{1-\frac{2}{\pi^2}\psi} \tag{3.16}$$

and

$$\Theta_{\text{max}} = \frac{2}{\pi}\psi \tanh^{-1}\sqrt{1-\frac{2}{\pi^2}\psi}. \tag{3.17}$$

Thus, the rise time is

$$\Theta_{\text{max}} - \Theta_{\text{min}} = \frac{4}{\pi}\psi \tanh^{-1}\sqrt{1-\frac{2}{\pi^2}\psi}. \tag{3.18}$$

By using hyperbolic trigonometric identities, it can be shown that Equation (3.18) may be written

$$\Theta_{\text{max}} - \Theta_{\text{min}} = \frac{4}{\pi}\psi \cosh^{-1}\sqrt{\frac{\pi^2}{2\psi}}, \tag{3.19}$$

which was the form presented by Blackstock. [48] Since the waveform is 2π periodic, the fall time is

$$2\pi - (\Theta_{\text{max}} - \Theta_{\text{min}}) = 2\pi\left(1 - \frac{2\psi}{\pi^2}\cosh^{-1}\sqrt{\frac{\pi^2}{2\psi}}\right). \tag{3.20}$$

The WSF can then be written (see Section 3.2.1.1) as

$$\mathrm{WSF} = \frac{\text{Rise Time}}{\text{Fall Time}} = \frac{\frac{2\psi}{\pi^2}\cosh^{-1}\sqrt{\frac{\pi^2}{2\psi}}}{1 - \frac{2}{\pi^2}\psi\cosh^{-1}\sqrt{\frac{\pi^2}{2\psi}}} \tag{3.21}$$

$$= \left[\frac{\frac{\pi^2}{2\psi}}{\cosh^{-1}\sqrt{\frac{\pi^2}{2\psi}}} - 1\right]^{-1} = \left[\frac{\frac{\pi^2\Gamma}{2(\sigma+1)}}{\cosh^{-1}\sqrt{\frac{\pi^2\Gamma}{2(\sigma+1)}}} - 1\right]^{-1}. \tag{3.22}$$

We compare the analytical form of the WSF from the Khokhlov solution with that calculated for the Fay solution. For this comparison, 10,000 terms of the Fourier series were included, and a single period was used, with 10,000 samples. A plot of the calculated values of the WSF as a function of σ for three values of the Gol'dberg number is shown in Figure 3.2.

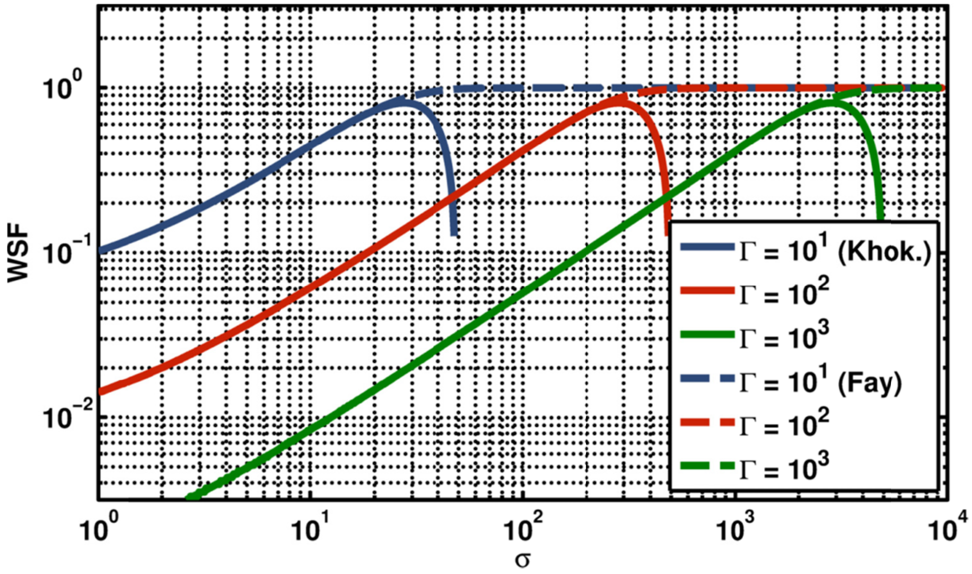

Figure 3.2. Plot of the wave steepening factor found using the Khokhlov solution (Khok.) and using the Fay solution, both plotted as a function of σ for three different values of Gol'dberg number.

In looking at Figure 3.2 recall that the Khokhlov solution is valid for $3 < \sigma < \Gamma$. Despite being invalid for $\sigma > \Gamma$, there is no discernible difference between the WSF values for the two solutions for $\sigma < 2\Gamma$. For $\sigma > 2\Gamma$ the analytic form predicts a lower WSF than the Fay solution does. Since the validity of the analytical form is limited to $\sigma < \Gamma$, the values predicted by the

Fay solution are more likely to be correct for $\sigma > 2\Gamma$. However, the fact that the WSF of the Khokhlov solution is analytical and does not rely on a finite sampling rate suggests that it is important.

3.2.2 Derivative Skewness

An analytical representation of the WSF of the Fay solution cannot be given because there is not an exact form of the WSF for an arbitrary Fourier series. On the other hand derivative skewness, which may give details about the shock content of a waveform, have an exact form for a waveform described in terms of a Fourier series. Since there are several Fourier series of interest in nonlinear acoustics – for example, the Fubini solution, Mendousse solution, and Fay solution – the derivation of the skewness for an arbitrary Fourier series will be presented first. The derivative skewness of the Fubini and Earnshaw solutions, which assume no linear losses, are then derived, followed by a derivation of the derivative skewness of the Fay solution, which assumes propagation with thermoviscous losses past the beginning of the sawtooth propagation regime.

3.2.2.1 Skewness of a Fourier Series

We seek the skewness of a 2π-periodic function $f(t)$ that may be written as

$$f(t) = \sum_{n=1}^{\infty} A_n \cos(nt) + \sum_{n=1}^{\infty} B_n \sin(nt) = \alpha + \beta, \tag{3.23}$$

where α is the cosine summation and β is the sine summation. By Equation (3.2) we know that the skewness may be written in terms of the expectation values of $f^3(t)$ and $f^2(t)$. Due to periodicity, the expectation value of the cube of Equation (3.23) may be written

$$E[f^3(t)] = \frac{1}{2\pi}\int_{-\pi}^{\pi} (\alpha + \beta)^3 dt \tag{3.24}$$

$$= \frac{1}{2\pi}\left[\int_{-\pi}^{\pi} \alpha^3 dt + 3\int_{-\pi}^{\pi} \alpha^2 \beta dt + 3\int_{-\pi}^{\pi} \alpha\beta^2 dt + \int_{-\pi}^{\pi} \beta^3 dt\right]. \tag{3.25}$$

Since β is an odd function, the second and fourth integrals are identically zero. The first integral is

$$\int_{-\pi}^{\pi} \alpha^3 dt = \int_0^{2\pi} \left\{\sum_{n=1}^{\infty} A_n \cos(nt)\right\}^3 dt \tag{3.26}$$

$$= \int_0^{2\pi} \sum_{n=1}^{\infty}\sum_{m=1}^{\infty}\sum_{l=1}^{\infty} A_n A_m A_l \cos(nt)\cos(mt)\cos(lt)\, dt \tag{3.27}$$

$$= \sum_{n=1}^{\infty}\sum_{m=1}^{\infty}\sum_{l=1}^{\infty} A_n A_m A_l \int_0^{2\pi} \cos(nt)\cos(mt)\cos(lt)\, dt. \tag{3.28}$$

By repeated use of the trigonometric identity

$$\cos(u)\cos(v) = \frac{\cos(u+v)}{2} + \frac{\cos(u-v)}{2}, \tag{3.29}$$

we find that the integrand in Equation (3.28) becomes

$$\begin{aligned} &\cos(nt)\cos(mt)\cos(lt) \\ &\qquad = \frac{1}{4}\begin{bmatrix} \cos([m+l+n]t) + \cos([m+l-n]t) \\ + \cos([m-l+n]t) + \cos([m-l-n]t) \end{bmatrix}. \end{aligned} \tag{3.30}$$

Each term in Equation (3.30) will integrate to zero unless their individual triple indices (m, n, l) combine to zero, in which case, it will integrate to 2π. These conditions include

$$\begin{array}{c} m+l+n=0 \\ m+l-n=0 \\ m-l+n=0. \\ m-l-n=0 \end{array} \tag{3.31}$$

Since $n, m, l > 0$, the first condition in Equation (3.31) will never occur. Notice that the remaining three conditions may be written

$$\begin{aligned} m+l&=n\\ n+m&=l.\\ l+n&=m \end{aligned} \tag{3.32}$$

These three conditions may be written in the triple summation in terms of a Kronecker delta,

$$\delta_{n,m}=\begin{cases}1 & n=m\\ 0 & n\neq m'\end{cases} \tag{3.33}$$

as

$$\begin{aligned}\int_{-\pi}^{\pi}\alpha^3dt=\frac{\pi}{2}\Bigg[&\sum_{n=1}^{\infty}\sum_{m=1}^{\infty}\sum_{l=1}^{\infty}A_nA_mA_l\delta_{m+l,n}\\ &+\sum_{n=1}^{\infty}\sum_{m=1}^{\infty}\sum_{l=1}^{\infty}A_nA_mA_l\delta_{n+m,l}\\ &+\sum_{n=1}^{\infty}\sum_{m=1}^{\infty}\sum_{l=1}^{\infty}A_nA_mA_l\delta_{l+n,m}\Bigg].\end{aligned} \tag{3.34}$$

By rearranging the arbitrary indices n, m, and l, it can be shown that each of the triple summations in Equation (3.34) are equal to each other. Therefore, the first integral of Equation (3.25) may be written

$$\int_{-\pi}^{\pi}\alpha^3dt=\frac{3\pi}{2}\sum_{n=1}^{\infty}\sum_{m=1}^{\infty}\sum_{l=1}^{\infty}A_nA_mA_l\delta_{n+m,l}. \tag{3.35}$$

The third integral of Equation (3.25) may be found using similar logic. This integral is written

$$\int_{-\pi}^{\pi}\alpha\beta^2dt=\int_{-\pi}^{\pi}\left\{\sum_{n=1}^{\infty}A_n\cos(nt)\right\}\left\{\sum_{m=1}^{\infty}B_m\sin(nt)\right\}^2dt \tag{3.36}$$

$$= \sum_{n=1}^{\infty}\sum_{m=1}^{\infty}\sum_{l=1}^{\infty} A_n B_m B_l \int_{-\pi}^{\pi} \cos(nt)\sin(mt)\sin(lt)\,dt. \tag{3.37}$$

Noting that

$$\sin(a)\sin(b) = \frac{1}{2}[\cos(a-b) - \cos(a+b)], \tag{3.38}$$

we find that the integrand of Equation (3.37) may be written

$$\frac{1}{4}\begin{bmatrix} \cos([n-m+l]t) + \cos([n+m-l]t) \\ -\cos([n-m-l]t) - \cos([n+m+l]t) \end{bmatrix}. \tag{3.39}$$

Applying the same reasoning used in obtaining Equation (3.34), we find that

$$\begin{aligned} \int_{-\pi}^{\pi} \alpha\beta^2 dt = \frac{\pi}{2}\Bigg[& \sum_{n=1}^{\infty}\sum_{m=1}^{\infty}\sum_{l=1}^{\infty} A_n B_m B_l \delta_{l+n,m} \\ & + \sum_{n=1}^{\infty}\sum_{m=1}^{\infty}\sum_{l=1}^{\infty} A_n B_m B_l \delta_{n+m,l} \\ & - \sum_{n=1}^{\infty}\sum_{m=1}^{\infty}\sum_{l=1}^{\infty} A_n B_m B_l \delta_{m+l,n} \Bigg]. \end{aligned} \tag{3.40}$$

By rearranging the arbitrary indices, it can be shown that the first and second triple summations are identical. Then, the third integral in Equation (3.40) may be written

$$\begin{aligned} \int_{-\pi}^{\pi} \alpha\beta^3 dt = \frac{\pi}{2}\Bigg[& 2\sum_{n=1}^{\infty}\sum_{m=1}^{\infty}\sum_{l=1}^{\infty} A_n B_m B_l \delta_{n+m,l} \\ & - \sum_{n=1}^{\infty}\sum_{m=1}^{\infty}\sum_{l=1}^{\infty} A_n B_m B_l \delta_{m+l,n} \Bigg]. \end{aligned} \tag{3.41}$$

Thus the expectation value of $f^3(t)$ is

$$\begin{aligned} E[f^3(t)] = \frac{3}{4}\Bigg[&\sum_{n=1}^{\infty}\sum_{m=1}^{\infty}\sum_{l=1}^{\infty} A_n A_m A_l \delta_{n+m,l} \\ &+ 2\sum_{n=1}^{\infty}\sum_{m=1}^{\infty}\sum_{l=1}^{\infty} A_n B_m B_l \delta_{n+m,l} \\ &- \sum_{n=1}^{\infty}\sum_{m=1}^{\infty}\sum_{l=1}^{\infty} A_n B_m B_l \delta_{m+l,n} \Bigg]. \end{aligned} \tag{3.42}$$

In the special case that $B_n = 0$ for all n, the Equation (3.42) reduces to

$$E[f^3(t)] = \frac{3}{4}\sum_{n=1}^{\infty}\sum_{m=1}^{\infty}\sum_{l=1}^{\infty} A_n A_m A_l \delta_{n+m,l}. \tag{3.43}$$

The expectation value of $f^2(t)$ may be found as well. Again, due to periodicity, we may write

$$E[f^2(t)] = \frac{1}{2\pi}\int_{-\pi}^{\pi}(\alpha+\beta)^2 dt = \frac{1}{2\pi}\int_{-\pi}^{\pi}(\alpha^2+\beta^2+2\alpha\beta)dt. \tag{3.44}$$

Since $\alpha\beta$ is an odd function, this term integrates to zero. The remaining terms yield

$$E[f^2(t)] = \frac{1}{2\pi}\int_{-\pi}^{\pi}\left[\left\{\sum_{n=1}^{\infty} A_n \cos(nt)\right\}^2 + \left\{\sum_{n=1}^{\infty} B_n \sin(nt)\right\}^2\right] dt \tag{3.45}$$

$$\begin{aligned} = \frac{1}{2\pi}\int_{-\pi}^{\pi}\sum_{n=1}^{\infty}\sum_{m=1}^{\infty} &[A_n A_m \cos(nt)\cos(mt) \\ &+ B_n B_m \sin(nt)\sin(mt)]\, dt \end{aligned} \tag{3.46}$$

$$= \frac{1}{2\pi} \sum_{n=1}^{\infty} \sum_{m=1}^{\infty} \left\{ A_n A_m \int_{-\pi}^{\pi} \cos(nt) \cos(mt)\, dt \right. \qquad (3.47)$$

$$\left. + B_n B_m \int_{-\pi}^{\pi} \sin(nt) \sin(mt)\, dt \right\}$$

$$= \frac{1}{2\pi} \sum_{n=1}^{\infty} \sum_{m=1}^{\infty} (A_n A_m + B_n B_m) \delta_{nm} \pi. \qquad (3.48)$$

The expectation value may take the form of Equation (3.48) due to the orthogonality of the integrand of Equation (3.47). The expectation value of $f^2(t)$ may then be simplified to

$$E[f^2(t)] = \frac{1}{2} \sum_{n=1}^{\infty} (A_n^2 + B_n^2). \qquad (3.49)$$

Again, in the special case that $B_n = 0$ for all n, Equation (3.49) reduces to

$$E[f^2(t)] = \frac{1}{2} \sum_{n=1}^{\infty} A_n^2. \qquad (3.50)$$

Using Equations (3.42) and (3.49) with Equation (3.2), we find that the skewness of $f(t)$ is

$$\mathrm{Sk}\{f(t)\}$$

$$= \frac{3}{\sqrt{2}} \frac{A_n A_m A_l \delta_{n+m,l} + 2A_n B_m B_l \delta_{l+n,m} - A_n B_m B_l \delta_{m+l,n}}{[\sum_n (A_n^2 + B_n^2)]^{3/2}}. \qquad (3.51)$$

In Equation (3.51) the combinations of three Fourier coefficients and the delta function is shorthand for a triple summation:

$$\gamma_{nml} \delta_{n+m,l} = \sum_{n=1}^{\infty} \sum_{m=1}^{\infty} \sum_{l=1}^{\infty} \gamma_{nml} \delta_{n+m,l}, \qquad (3.52)$$

where γ_{nml} is an arbitrary three-dimensional scalar array, is used. In the special case that $B_n = 0$ for all n, the skewness reduces to

$$\mathrm{Sk}\{f(t)\} = \frac{3}{\sqrt{2}} \frac{A_n A_m A_l \delta_{n+m,l}}{[\sum_n A_n^2]^{3/2}}, \tag{3.53}$$

and in the special case that $A_n = 0$ for all n, the skewness is identically zero. If $A_n = B_n = 0$ for all n, the skewness is not defined in this method; however, this is just a flat line with a skewness of zero.

It may also be useful in calculating skewness values to note that, for arbitrary scalar arrays E_n, F_n, and G_n,

$$E_n F_m G_l \delta_{n+m,l} = \sum_{n=1}^{\infty} \sum_{m=1}^{\infty} \sum_{l=1}^{\infty} E_n F_m G_l \delta_{n+m,l} = \sum_{l=2}^{\infty} G_l \sum_{n=1}^{l-1} E_n F_{l-n}. \tag{3.54}$$

3.2.2.2 Fubini Solution

The Fubini solution is described in Section 2.2.2.2. The time-derivative of the Fubini solution is written as Fourier cosine series (see Equation (2.20)). Thus, according to Equation (3.53), the derivative skewness of the Fubini solution is

$$\mathrm{Sk}\{\partial P/\partial\theta\} = \frac{3}{\sqrt{2}} \frac{J_n(n\sigma) J_m(m\sigma) J_l(l\sigma) \delta_{n+m,l}}{[\sum_{n=1}^{\infty} J_n^2(n\sigma)]^{3/2}}, \tag{3.55}$$

which is plotted as a function of σ in Figure 3.3. In the limit that $\sigma \to 1$, the triple series in the numerator diverges, and the derivative skewness goes to infinity. This is because a shock has formed at $\sigma = 1$. Since the Fubini solution assumes the propagation is lossless (other than nonlinear losses at shock fronts), after a shock has formed, there will always be shocks in the waveform. Therefore, the analytical derivative skewness will remain infinite for all $\sigma > 1$. It should be noted that the values shown in Figure 3.3 appear to agree with the results by Shepherd *et al*. [37] up to about $\sigma = 0.9$. The difference is discussed in the context of finite-sampling effects subsequently.

Based on the results for the Fubini solution in Figure 3.3, general trends of the derivative skewness for a waveform propagating without linear losses may be suggested. If a waveform is assumed to have very little nonlinear distortion for $\sigma < 0.2$, then a derivative skewness of 0.5 may be considered to be low. If a waveform is assumed to have very significant nonlinear distortion for $\sigma > 0.9$, then a derivative skewness of 5 may be considered high. The effects of discrete sampling will be considered subsequently.

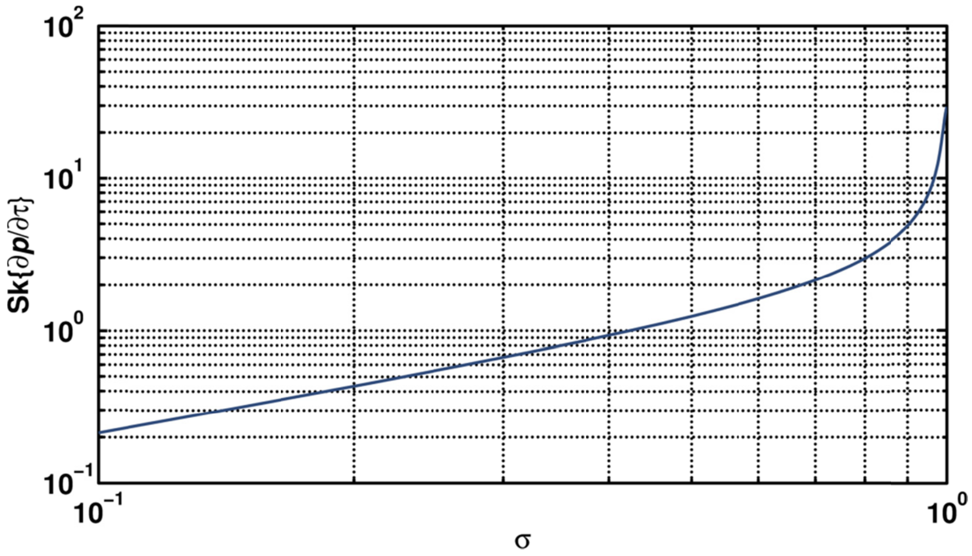

Figure 3.3. The skewness of the time-derivative of the pressure (derivative skewness, or $\mathrm{Sk}\{\partial p/\partial \theta\}$) of the Fubini solution. The dimensionless variable σ is the distance from the source divided by the shock formation distance.

3.2.2.3 Earnshaw Solution

The derivative skewness may be exactly calculated. The expectation value of the n^{th} power of the time-derivative of the waveform described by the Earnshaw solution assuming an initially sinusoidal signal at a distance σ can be written, using Equation (2.14) and Equation (2.18), as

$$E[(\partial P/\partial\theta)^n] = \frac{1}{2\pi}\int_0^{2\pi}\left(\frac{\partial P}{\partial\theta'}\right)^n d\theta' \tag{3.56}$$

$$= \frac{1}{2\pi}\int_0^{2\pi}\left(\frac{\cos(\theta)}{1-\sigma\cos(\theta)}\right)^n (d\theta[1-\sigma\cos(\theta)]) \tag{3.57}$$

$$= \frac{1}{2\pi}\int_0^{2\pi}\frac{\cos^n(\theta)\, d\theta}{(1-\sigma\cos(\theta))^{n-1}}. \tag{3.58}$$

Evaluating the integral in Equation (3.58) for $n = 3$ yields

$$E[(\partial P/\partial\theta)^3] = \frac{2(1-\sigma^2)^{3/2} + 3\sigma^2 - 2}{\sigma^3(1-\sigma^2)^{3/2}}, \tag{3.59}$$

and evaluating the integral for $n = 2$ yields

$$E[(\partial P/\partial\theta)^2] = \frac{1-(1-\sigma^2)^{1/2}}{\sigma^2(1-\sigma^2)^{1/2}}. \tag{3.60}$$

These integrations were found using Maple™. [49] Combining Eq. (3.59) and Eq. (3.60) with Eq. (3.1) produces the derivative skewness of the Earnshaw solution assuming an initially sinusoidal signal, which is

$$\mathrm{Sk}\{\partial P/\partial\theta\} = \frac{\dfrac{2(1-\sigma^2)^{3/2} + 3\sigma^2 - 2}{\sigma^3(1-\sigma^2)^{3/2}}}{\left[\dfrac{1-(1-\sigma^2)^{1/2}}{\sigma^2(1-\sigma^2)^{1/2}}\right]^{\frac{3}{2}}} \tag{3.61}$$

$$= \frac{2(1-\sigma^2)^{3/2} + 3\sigma^2 - 2}{(1-\sigma^2)^{3/4}\left(1-\sqrt{1-\sigma^2}\right)^{3/2}}. \tag{3.62}$$

The derivative skewness from the Earnshaw solution for $\sigma \ll 1$ can be approximated as

$$\mathrm{Sk}\{\partial P/\partial\theta\} \approx \frac{3}{\sqrt{2}}\sigma. \tag{3.63}$$

The derivative skewness derived from the Earnshaw solution for $\sigma \to 1$ can be approximated as

$$\mathrm{Sk}\{\partial P/\partial\theta\} \approx \frac{1}{(1-\sigma^2)^{3/4}}. \tag{3.64}$$

Equation (3.62) is equivalent to Equation (3.55), but is not in terms of an infinite series. Comparing the Fubini result in Equation (3.55) and the Earnshaw result in Equation (3.62) allows for an analysis of the error associated with using a truncated series to estimate the skewness of a waveform. The analytical derivative skewness of a waveform modeled by the Earnshaw solution and estimates of the derivative skewness based on the Fubini solution using different numbers of terms are plotted in Figure 3.4 on (a) a linear abscissa and (b) a logarithmic abscissa. The values of N indicate the number of terms included in the approximation of each of the infinite series in Equation (3.55). As σ approaches 1, the approximations all level off at some N-dependent value, while the analytical form continues to increase. The effect of increasing the number of terms is a more accurate estimate of the skewness is obtained for a large range of σ. For $\sigma < 0.7$ even the estimate only using 10 terms well approximates the analytical form. The estimate using 1000 terms is a reasonable approximation almost to $\sigma = 0.99$, and 10,000 terms is a reasonable estimate as high as $\sigma = 0.997$. In general, it appears that derivative skewness estimates obtained by using a truncation of the infinite series in Equation (3.55) are accurate up to about two-thirds of the largest derivative skewness value that the estimates predict. As an example, the largest derivative skewness that one may estimate using 100 terms is about 10. Therefore, any derivative skewness value greater than about 6.6 estimated using only 100 terms is not likely to be accurate.

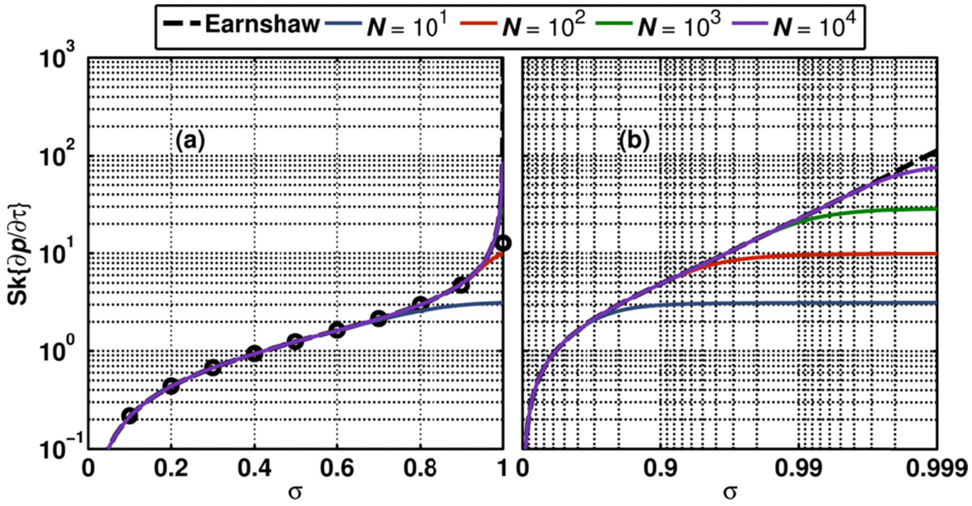

Figure 3.4. The analytical derivative skewness of an initially sinusoidal waveform modeled by the Earnshaw solution and estimates of the derivative skewness of the Fubini solution using *N* terms of each of the infinite series in Equation (3.55). The derivative skewness values are plotted on (a) a linear abscissa and (b) a logarithmic abscissa. The derivative skewness values found by Shepherd *et al.* [37] are plotted (black circles) in (a), for comparison.

3.2.2.4 Fay Solution

The Fay solution for the Burgers equation, which includes thermoviscous absorption, is described in Section 2.2.3.4. The time-derivative of the Fay solution is written as Fourier cosine series (see Equation (2.39)). Then, according to Equation (3.53), the derivative skewness of the Fay solution is

$$\mathrm{Sk}\{\partial P/\partial\theta\} = \frac{3}{\sqrt{2}} \frac{\frac{n}{\sinh(n\psi)}\frac{m}{\sinh(m\psi)}\frac{l}{\sinh(l\psi)}\delta_{n+m,l}}{\left[\sum_{n=1}^{\infty}\frac{n^2}{\sinh^2(n\psi)}\right]^{3/2}}, \qquad (3.65)$$

where $\psi = (1+\sigma)/\Gamma$. Equation (3.65) makes use of the triple-summation shorthand described in Equation (3.52). The derivative skewness of the Fay solution is plotted in Figure 3.5.

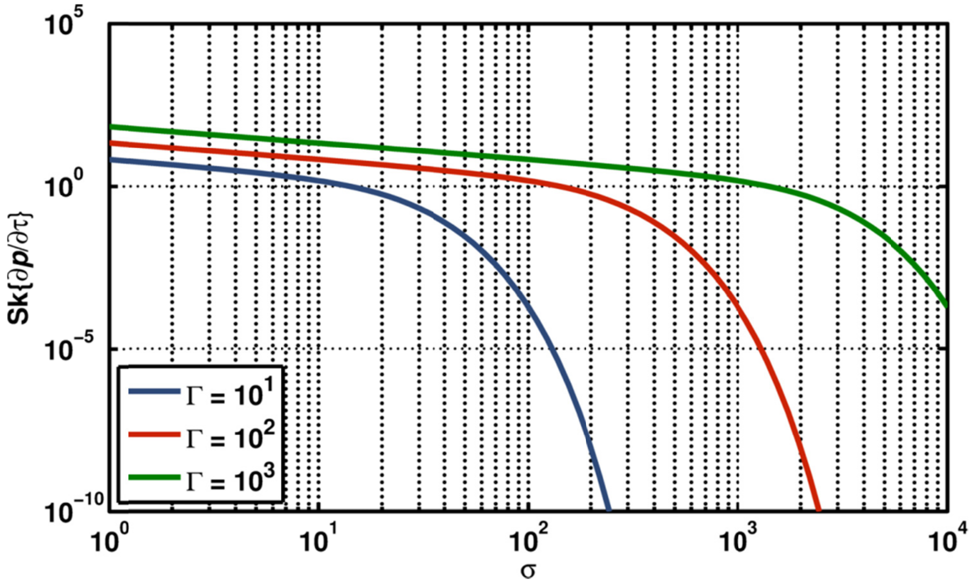

Figure 3.5. The skewness of the time-derivative of the pressure (derivative skewness, or $\mathrm{Sk}\{\partial p/\partial\theta\}$) of the Fay solution as a function of σ for three values of Gol'dberg number.

In the limit that $\Gamma \to \infty$ ($\psi \to 0$), that is, the limit that the propagation is lossless, the derivative skewness approaches infinity for small σ values. (It can be shown, using an asymptotic form of the Khokhlov solution, that for very small ψ, $\mathrm{Sk}\{\partial P/\partial\theta\}_{\psi\to 0} \approx (2\pi/5)\sqrt{3/\psi} = (2\pi/5)\sqrt{3\Gamma/(\sigma+1)}$.) This is expected, since the derivative skewness of the Fubini solution for $\sigma > 3$ is always infinite. In the limit that $\psi \to \infty$, that is, many absorption lengths from the source with finite losses, the Fay solution may be approximated as

$$P \approx \frac{4p_0}{\Gamma}\sum_{n=1}^{\infty} e^{-n\psi}\sin(n\theta), \tag{3.66}$$

(see Ref. [4]) which has a derivative skewness of

$$\mathrm{Sk}\{\partial P/\partial\theta\}_{\psi\to\infty} \approx \frac{3}{\sqrt{2}}\frac{ne^{-n\psi}me^{-m\psi}le^{-l\psi}\delta_{n+m,l}}{\left[\sum_{n=1}^{\infty} e^{-2n\psi}\right]^{\frac{3}{2}}} \tag{3.67}$$

$$= \frac{3}{\sqrt{2}}\frac{\sum_{l=2}^{\infty}\sum_{n=1}^{l-1} nl(l-n)e^{-2l\psi}}{\left[\sum_{n=1}^{\infty} e^{-2n\psi}\right]^{\frac{3}{2}}} \approx 3\sqrt{2}\frac{e^{-4\psi}}{e^{-3\psi}} \tag{3.68}$$

$$= 3\sqrt{2}e^{-\psi} = 3\sqrt{2}e^{-\sigma/\Gamma}. \tag{3.69}$$

Thus, as $\sigma \rightarrow \infty$ (or $\psi \rightarrow \infty$, which is the old-age propagation regime; wavefronts unsteepen as high-frequency content is absorbed) the derivative skewness of the Fay solution approaches zero exponentially.

3.3 Effects of Finite Sampling Rates

The measures described in Section 2.1 depend upon accurate (i.e., analytical) estimation of the first time-derivative of the pressure waveform. However, since in measurements the waveforms must be sampled discretely at finite time intervals, there is a limit to the maximum slopes that can be adequately resolved. These limits on the temporal resolution of the waveform derivatives are often significant in the study of acoustic shocks, and thus, a discussion of the sampling rate-related limitations of each of the measures defined in Section 2.1 is provided.

3.3.1 Finite-Difference of a Fourier Sine Series

Let $f(t)$ be a Fourier sine series, written

$$f(t) = \sum_{n=1}^{\infty} B_n \sin(nt). \tag{3.70}$$

An estimation of the first time-derivative of $f(t)$ can be obtained using a finite-difference technique. Using the uniform time step Δt, this is given by

$$\frac{\Delta f}{\Delta t} = \frac{f(t+\Delta t) - f(t)}{\Delta t} \tag{3.71}$$

$$= \frac{1}{\Delta t}\sum_{n=1}^{\infty} B_n \sin(nt + n\Delta t) - \frac{1}{\Delta t}\sum_{n=1}^{\infty} B_n \sin(nt) \tag{3.72}$$

$$= \frac{1}{\Delta t} \sum_{n=1}^{\infty} B_n (\sin(nt + n\Delta t) - \sin(nt)). \tag{3.73}$$

Using the trigonometric identity $\sin(a + b) = \sin(a)\cos(b) + \cos(a)\sin(b)$, Equation (3.73) becomes

$$\frac{\Delta f}{\Delta t} = \frac{1}{\Delta t} \sum_{n=1}^{\infty} B_n [\sin(nt)\cos(n\Delta t) + \cos(nt)\sin(n\Delta t) - \sin(nt)] \tag{3.74}$$

$$= \sum_{n=1}^{\infty} B_n \frac{\sin(n\Delta t)}{\Delta t} \cos(nt) + \sum_{n=1}^{\infty} B_n \frac{\cos(n\Delta t) - 1}{\Delta t} \sin(nt). \tag{3.75}$$

If we define

$$\begin{aligned} A'_n &= B_n \frac{\sin(n\Delta t)}{\Delta t} = nB_n \operatorname{sinc}(n\Delta t) \\ B'_n &= B_n \frac{\cos(n\Delta t) - 1}{\Delta t} \end{aligned}, \tag{3.76}$$

then we may write Equation (3.75) as

$$\frac{\Delta f}{\Delta t} = \sum_{n=1}^{\infty} A'_n \cos(nt) + \sum_{n=1}^{\infty} B'_n \sin(nt). \tag{3.77}$$

In the limit that $\Delta t \to 0$, we find that $A'_n \to nB_n$ and $B'_n \to 0$, which is the result obtained by assuming continuous sampling from the beginning. Thus, we find that the first time derivative a discretely sampled waveform expressed as a Fourier sine series may be expressed as a full Fourier series.

3.3.2 Wave Steepening Factor

The effect of discrete sampling on WSF estimates is evaluated by finding relationships between the WSF and the sampling rate for some of the analytical solutions described in Chapter 2. Specifically, the Fubini solution, a sawtooth function, and the Khokhlov solution will be considered. Understanding the effect of finite sampling rates on these solutions will lend insight into meaning of values of the WSF of measured waveforms.

3.3.2.1 Fubini-Earnshaw Solution

The Fubini solution describes the nonlinear evolution of an initially sinusoidal plane wave propagating without losses, and is written in terms of a Fourier series. Since the WSF of an arbitrary Fourier series is not known, this analysis will be supplemented by the Earnshaw solution.

In order to calculate a WSF estimate of a waveform, then we must first find the regions of the waveform that have positive time-derivative estimates and the regions that have negative time-derivative estimates. The boundaries between the positive and negative slopes will have a slope estimate of zero. For a sine wave, the time at which this occurs, Θ, is found by solving

$$\frac{f(\Theta+\Delta\theta)-f(\Theta)}{\Delta\theta}=\frac{\sin(\Theta+\Delta\theta)-\sin(\Theta)}{\Delta\theta}=0. \tag{3.78}$$

Using the trigonometric identity mentioned in Section 3.3.1, we find that

$$\frac{2}{\Delta\theta}\cos\left(\mathit{\Theta}+\frac{\Delta\theta}{2}\right)\sin\left(\frac{\Delta\theta}{2}\right)=0 \tag{3.79}$$

$$\Rightarrow \Theta=m\pi+\frac{\pi}{2}-\frac{\Delta\theta}{2}, \tag{3.80}$$

where $m=0,\pm1,\pm2,\ldots$, and even values of m represent the transition from positive slope to negative slope estimates, and odd values of m represent the transition from negative slope to positive slope estimates. Therefore, due to the periodicity of the waveform, averaging the slopes between $\theta=-\pi/2-\Delta\theta/2$ (Θ with $m=-1$) and $\theta=\pi/2-\Delta\theta/2$ (Θ with $m=0$) yields the average positive slope that would be estimated assuming a very long measurement time and that the value of $\nu=2\pi f_s/\omega$, where f_s is the sampling rate, is an irrational number. (The variable ν is a nondimensional number that indicates the sample-density of a waveform. The choice of an irrational number and long measurement time guarantees that every possible discretely sampled slope will be equally represented.) Similarly, averaging the slopes between $\theta = \pi/2 - \Delta\theta/2$ (Θ with $m = 0$) and $\theta = 3\pi/2 - \Delta\theta/2$ (Θ with $m = 1$) will be the average negative slope that would be estimated assuming a very long measurement time and that the value of ν is an irrational number. Note that $\nu = 1/\Delta t = 2\pi/\Delta\theta$. This means that Equation (3.80) may also be written

$$\Theta = m\pi + \frac{\pi}{2} - \frac{\pi}{\nu} = \pi\left(m + \frac{1}{2} - \frac{1}{\nu}\right). \tag{3.81}$$

The method described for a sinusoidal wave may be simply extended to the entire Fubni solution. The distortion due to nonlinear propagation without linear losses of a plane wave is strictly amplitude dependent (until shocks form), so the time delay between two points with the same amplitude will remain the same. This means that the time at which the slope estimate will be zero, Θ, will follow the distortion described by the Earnshaw solution in Section 2.2.2.1, which is

$$\begin{aligned} \Theta(\sigma) &= \pi\left(m + \frac{1}{2} - \frac{1}{\nu}\right) - \sigma \sin\left(\pi\left(m + \frac{1}{2} - \frac{1}{\nu}\right)\right) \\ &= \pi m + \frac{\pi}{2} - \frac{\pi}{\nu} - \sigma(-1)^m \cos\left(\frac{\pi}{\nu}\right). \end{aligned} \tag{3.82}$$

In addition, the long-time average positive slope estimate requires the mean slope between $\Theta(\sigma)$ for $m = -1$ and for $m = 0$:

$$E\left[\left(\frac{\Delta P}{\Delta\theta}\right)^{+}\right] = \frac{1}{\Theta(\sigma)|_{m=0} - \Theta(\sigma)|_{m=-1}} \int_{\Theta(\sigma)|_{m=-1}}^{\Theta(\sigma)|_{m=0}} \frac{\Delta P}{\Delta\theta} d\theta, \tag{3.83}$$

and the long-time average negative slope is found to be

$$E\left[\left(\frac{\Delta P}{\Delta\theta}\right)^{-}\right] = \frac{1}{\Theta(\sigma)|_{m=1} - \Theta(\sigma)|_{m=0}} \int_{\Theta(\sigma)|_{m=0}}^{\Theta(\sigma)|_{m=1}} \frac{\Delta P}{\Delta\theta}\, d\theta. \tag{3.84}$$

The integrals in Equation (3.83) and Equation (3.84) may be evaluated using the derivative estimate presented in Equation (3.77):

$$\int_a^b \frac{\Delta P}{\Delta\theta}\, d\theta = \int_a^b \sum_{n=1}^{\infty} [A_n' \cos(n\theta) + B_n' \sin(n\theta)]\, d\theta \tag{3.85}$$

$$= \sum_{n=1}^{\infty} \left[\frac{A_n'}{n} \sin(n\theta) - \frac{B_n'}{n} \cos(n\theta)\right]_a^b \tag{3.86}$$

$$= \sum_{n=1}^{\infty} \frac{1}{n} \{A_n'[\sin(nb) - \sin(na)] - B_n'[\cos(nb) - \cos(na)]\} \tag{3.87}$$

$$\begin{aligned} = \sum_{n=1}^{\infty} \frac{1}{n} \Bigg\{ & A_n' \left[2\cos\left(n\frac{[b+a]}{2}\right) \sin\left(n\frac{[b-a]}{2}\right)\right] \\ & + B_n' \left[2\sin\left(n\frac{[b+a]}{2}\right) \sin\left(n\frac{[b-a]}{2}\right)\right]\Bigg\} \end{aligned} \tag{3.88}$$

$$\begin{aligned} = \sum_{n=1}^{\infty} \frac{2B_n}{n\Delta\theta} \sin\left(n\frac{[b-a]}{2}\right) \Bigg\{ & \sin(n\Delta\theta) \cos\left(n\frac{[b+a]}{2}\right) \\ & + (\cos(n\Delta\theta) - 1) \sin\left(n\frac{[b+a]}{2}\right)\Bigg\} \end{aligned} \tag{3.89}$$

$$= \sum_{n=1}^{\infty} \frac{2B_n}{n\Delta\theta} \sin\left(n\frac{[b-a]}{2}\right) \left\{\sin\left(n\Delta\theta + n\frac{[b+a]}{2}\right) - \sin\left(n\frac{[b+a]}{2}\right)\right\} \tag{3.90}$$

$$= \sum_{n=1}^{\infty} 4B_n \sin\left(n\frac{[b-a]}{2}\right) \cos\left(n\frac{\Delta\theta}{2} + n\frac{[b+a]}{2}\right) \operatorname{sinc}\left(n\frac{\Delta\theta}{2}\right) \tag{3.91}$$

$$= \sum_{n=1}^{\infty} 4B_n \sin\left(n\frac{[b-a]}{2}\right) \cos\left(n\frac{\pi}{\nu} + n\frac{[b+a]}{2}\right) \operatorname{sinc}\left(n\frac{\pi}{\nu}\right). \tag{3.92}$$

Then, noting that,

$$\Theta(\sigma)|_{m=0} - \Theta(\sigma)|_{m=-1} = \pi - 2\sigma\cos\left(\frac{\pi}{\nu}\right) \tag{3.93}$$

$$\Theta(\sigma)|_{m=0} + \Theta(\sigma)|_{m=-1} = -\frac{2\pi}{\nu} \tag{3.94}$$

$$\Theta(\sigma)|_{m=1} - \Theta(\sigma)|_{m=0} = \pi + 2\sigma\cos\left(\frac{\pi}{\nu}\right) \tag{3.95}$$

$$\Theta(\sigma)|_{m=1} + \Theta(\sigma)|_{m=0} = 2\pi - \frac{2\pi}{\nu}, \tag{3.96}$$

we find that

$$\int_{\Theta(\sigma)|_{m=-1}}^{\Theta(\sigma)|_{m=0}} \frac{\Delta P}{\Delta\theta}\, d\theta = \sum_{n=1}^{\infty} 4B_n \sin\left(\frac{n}{2}\left[\pi - 2\sigma\cos\left(\frac{\pi}{\nu}\right)\right]\right)\cos\left(n\frac{\pi}{\nu} - n\frac{\pi}{\nu}\right)\operatorname{sinc}\left(n\frac{\pi}{\nu}\right) \tag{3.97}$$

$$= \sum_{n=1}^{\infty} 4B_n \sin\left(\frac{n}{2}\left[\pi - 2\sigma\cos\left(\frac{\pi}{\nu}\right)\right]\right)\operatorname{sinc}\left(n\frac{\pi}{\nu}\right), \tag{3.98}$$

and that

$$\int_{\Theta(\sigma)|_{m=0}}^{\Theta(\sigma)|_{m=1}} \frac{\Delta P}{\Delta\theta}\, d\theta = \sum_{n=1}^{\infty} 4B_n \sin\left(\frac{n}{2}\left[\pi + 2\sigma\cos\left(\frac{\pi}{\nu}\right)\right]\right)\cos\left(n\frac{\pi}{\nu} + n\left(\pi - \frac{\pi}{\nu}\right)\right)\operatorname{sinc}\left(n\frac{\pi}{\nu}\right) \tag{3.99}$$

$$= \sum_{n=1}^{\infty} 4B_n \sin\left(\frac{n}{2}\left[\pi + 2\sigma\cos\left(\frac{\pi}{\nu}\right)\right]\right)(-1)^n \operatorname{sinc}\left(n\frac{2\pi}{\nu}\right) \tag{3.100}$$

$$\begin{aligned} = \sum_{n=1}^{\infty} 4B_n \bigg\{&(-1)^n \sin\left(n\frac{\pi}{2}\right)\cos\left(n\sigma\, cos\left(\frac{\pi}{\nu}\right)\right) \\ &+ (-1)^n \cos\left(n\frac{\pi}{2}\right)\sin\left(n\sigma\, cos\left(\frac{\pi}{\nu}\right)\right)\bigg\}\operatorname{sinc}\left(n\frac{2\pi}{\nu}\right). \end{aligned} \tag{3.101}$$

Since $\sin(n\pi/2) = 0$ when n is even, and $\cos(n\pi/2) = 0$ when n is odd, the $(-1)^n$ term in front of the $\sin(n\pi/2)$ term in the curly brackets in Equation (3.101) may be replaced by a minus sign, and the $(-1)^n$ term in front of the $\cos(n\pi/2)$ term may be neglected. Thus, Equation (3.101) may be written

$$\int_{\Theta(\sigma)|_{m=0}}^{\Theta(\sigma)|_{m=1}} \frac{\Delta P}{\Delta \theta} d\theta = \sum_{n=1}^{\infty} -4B_n \left\{ \sin\left(n\frac{\pi}{2}\right) \cos\left(n\sigma\, cos\left(\frac{\pi}{\nu}\right)\right) - \cos\left(n\frac{\pi}{2}\right) \sin\left(n\sigma\, cos\left(\frac{\pi}{\nu}\right)\right) \right\} \operatorname{sinc}\left(n\frac{2\pi}{\nu}\right) \tag{3.102}$$

$$= -\sum_{n=1}^{\infty} 4B_n \sin\left(\frac{n}{2}\left[\pi - 2\sigma \cos\left(\frac{\pi}{\nu}\right)\right]\right) \operatorname{sinc}\left(n\frac{\pi}{\nu}\right) = -\int_{\Theta(\sigma)|_{m=-1}}^{\Theta(\sigma)|_{m=0}} \frac{\Delta P}{\Delta \theta} d\theta. \tag{3.103}$$

Thus, the integrals in Equation (3.83) and Equation (3.84) have equal magnitude an opposite sign. Using Equation (3.1), we find that the WSF estimate for the discretely sampled Fubini solution is

$$\mathrm{WSF} = \frac{\pi - 2\sigma \cos\left(\frac{\pi}{\nu}\right)}{\pi + 2\sigma \cos\left(\frac{\pi}{\nu}\right)}. \tag{3.104}$$

These WSF estimates for the discretely sampled Fubini solution are plotted as a function of σ in Figure 3.6(a) for several values of ν (or sample-densities). The number of terms used in the infinite summation was five times the value of ν. For comparison, the exact WSF values assuming continuous sampling are also plotted. The relative errors between the exact WSF and the WSF estimates ($|1 - \mathrm{WSF}_\nu/\mathrm{WSF}_{\mathrm{cont}}|$) are plotted in Figure 3.6(b). The error plot shows that, at least in the pre-shock region, greater values of σ generate greater errors for a given sampling frequency. However, the errors are quite small. As seen by the blue line in Figure 3.6(b), even $\nu = 10$ only has about 10% error at the shock formation distance. If we assume that less than 1% error is sufficient precision, then it appears that $\nu > 100$ is sufficient to estimate the WSF for initially sinusoidal plane waves propagating without linear losses prior to shock formation. Based on the trends of the WSF estimate errors, it seems likely that $\nu > 1000$ would be sufficient to estimate the WSF value for all σ.

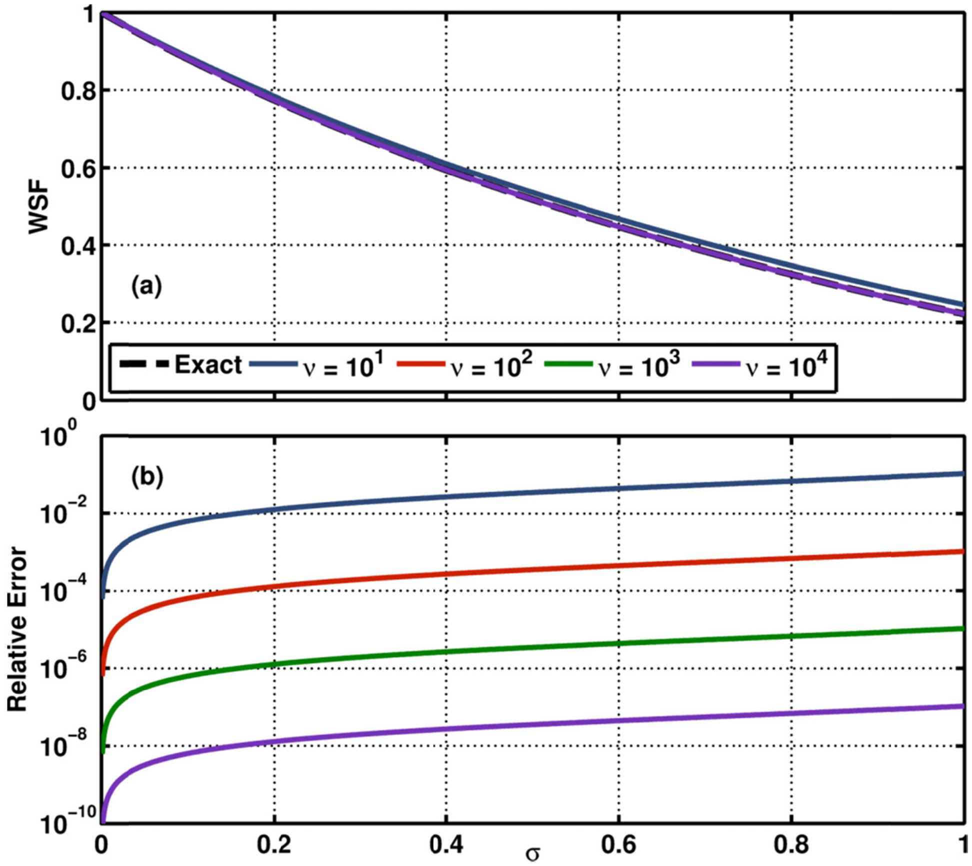

Figure 3.6. (a) Estimates of the WSF for $\nu = 10^1, 10^2, 10^3$, and 10^4. The exact WSF derived from using continuous sampling is plotted for comparison. (b) The relative error of the estimates in (a). The relative error is defined as $|1 - \mathrm{WSF}_\nu/\mathrm{WSF}_{\mathrm{cont}}|$, where WSF_ν is the estimate of the WSF for a given value of ν, and $\mathrm{WSF}_{\mathrm{cont}}$ is the exact WSF value using continuous sampling.

An interesting feature of the error plot in Figure 3.6 is that there appears to be a $1/\nu^2$ dependence for large values of ν. This observation may be made analytical by assuming that the arguments of the cosine terms in Equation (3.104) are small:

$$\text{Relative Error} = \left|1 - \frac{\mathrm{WSF}_\nu}{\mathrm{WSF}_{\mathrm{cont}}}\right| = \left|1 - \frac{\left(\dfrac{\pi - 2\sigma\cos\left(\frac{\pi}{\nu}\right)}{\pi + 2\sigma\cos\left(\frac{\pi}{\nu}\right)}\right)}{\left(\dfrac{\pi - 2\sigma}{\pi + 2\sigma}\right)}\right| \qquad (3.105)$$

$$\approx \left| 1 - \frac{\left(\dfrac{\pi - 2\sigma\left(1 - \dfrac{\pi^2}{\nu^2}\right)}{\pi + 2\sigma\left(1 - \dfrac{\pi^2}{\nu^2}\right)} \right)}{\left(\dfrac{\pi - 2\sigma}{\pi + 2\sigma}\right)} \right| = \left| 1 - \left(\frac{\pi - 2\sigma + \dfrac{2\pi^2\sigma}{\nu^2}}{\pi + 2\sigma - \dfrac{2\pi^2\sigma}{\nu^2}} \right) \left(\frac{\pi + 2\sigma}{\pi - 2\sigma} \right) \right| \tag{3.106}$$

$$= \left| 1 - \frac{1 + \dfrac{2\pi^2\sigma}{\nu^2}(\pi - 2\sigma)^{-1}}{1 - \dfrac{2\pi^2\sigma}{\nu^2}(\pi + 2\sigma)^{-1}} \right| = \left| \frac{\dfrac{2\pi^2\sigma}{\nu^2}(\pi + 2\sigma)^{-1} + \dfrac{2\pi^2\sigma}{\nu^2}(\pi - 2\sigma)^{-1}}{1 - \dfrac{2\pi^2\sigma}{\nu^2}(\pi + 2\sigma)^{-1}} \right| \tag{3.107}$$

$$\approx \frac{4\pi^3\sigma}{\pi^2 - 4\sigma^2} \cdot \frac{1}{\nu^2}. \tag{3.108}$$

3.3.2.2 Sawtooth Wave

For initially sinusoidal waves with very large Gol'dberg numbers, starting at $\sigma = 3$ the waveform may be modeled as a sawtooth wave. Although the WSF of a discretely sampled sawtooth may be modeled with the Khokhlov solution, a simpler expression of the WSF estimate of the sawtooth limit may be found using the mathematical description in Equation (2.25).

Suppose that $S(t)$ is sampled discretely with uniform normalized intervals of $\Delta\theta = 2\pi f \Delta t$, where f is the sawtooth frequency and Δt is the actual sample interval. Then the sampling rate is $f_s = \Delta t^{-1} = 2\pi f / \Delta\theta$, and the analytic function in Equation (2.25) will be partitioned into the array

$$P(t) \to P_n = \frac{2\pi}{1 + \sigma}\left(\text{floor}\left[\frac{n\Delta\theta}{2\pi}\right] - \frac{n\Delta\theta}{2\pi} + \frac{1}{2} \right). \tag{3.109}$$

Using a finite-difference scheme, the estimate of the time-derivative of the sawtooth function is

$$\frac{\partial P}{\partial \theta} \to \frac{\Delta P_n}{\Delta\theta} = \frac{P_{n+1} - P_n}{\Delta\theta} \tag{3.110}$$

$$= \frac{2\pi}{(1 + \sigma)\Delta\theta}\left[\left\{ \text{floor}\left[\frac{(n+1)\Delta\theta}{2\pi}\right] - \frac{(n+1)\Delta\theta}{2\pi} + \frac{1}{2} \right\} - \left\{ \text{floor}\left[\frac{n\Delta\theta}{2\pi}\right] - \frac{n\Delta\theta}{2\pi} + \frac{1}{2} \right\} \right] \tag{3.111}$$

$$= \frac{2\pi}{(1+\sigma)\Delta\theta}\left(\text{floor}\left[\frac{(n+1)\Delta\theta}{2\pi}\right] - \text{floor}\left[\frac{n\Delta\theta}{2\pi}\right] - \frac{\Delta\theta}{2\pi}\right). \tag{3.112}$$

Since the discontinuity associated with the floor function denotes an acoustic shock, then $\text{floor}[(n+1)\Delta\theta/2\pi] - \text{floor}[n\Delta\theta/2\pi] = M_n$ is the number of shocks that have occurred between $n\Delta\theta$ and $(n+1)\Delta\theta$. If we assume $f_s > f$, we find that M_n can only take on values of zero or one, and so the derivative estimate will be

$$\frac{\Delta P_n}{\Delta\theta} = -\frac{1}{1+\sigma} \tag{3.113}$$

if there is no shock, or

$$\frac{\Delta P_n}{\Delta\theta} = \frac{2\pi}{(1+\sigma)\Delta\theta}\left(1 - \frac{\Delta\theta}{2\pi}\right) = \frac{2\pi - \Delta\theta}{(1+\sigma)\Delta\theta} \tag{3.114}$$

if there is a shock.

The average number of measurement points between two shocks, which we will call N, is the period of the sawtooth divided by the spacing between samples, or, noting that the period is the inverse of the frequency,

$$N = \frac{f_s}{f}. \tag{3.115}$$

Since there is one shock per period, the average number of data points that lie within a single period of a sawtooth wave (or, the number of data points in a row that are not separated by shocks) is $N - 1$. Therefore the long-time WSF for a sawtooth wave can be analytically written as

$$\text{WSF} = \frac{\left|-\frac{1}{1+\sigma}\right|}{\left[\frac{2\pi - \Delta\theta}{(1+\sigma)\Delta\theta}\right]} = \frac{1}{2\pi/\Delta\theta - 1} = \frac{1}{\nu - 1}. \tag{3.116}$$

Since the WSF of a continuously sampled sawtooth wave is actually zero, the relative error of the estimated WSF undefined, and Equation (3.116) defines the absolute error.

If f_s is 96 000 Hz and f is 1000 Hz, then the absolute error of the WSF would be about $1/100 = 1\%$. In the limit that $f_s \to \infty$, or the sampling becomes continuous, the WSF approaches zero, but in general, the WSF of a discretely sampled sawtooth wave will never be identically zero due to the lack of temporal resolution of the waveforms near shocks.

3.3.2.3 Khokhlov Solution

Estimates of the WSF for waves propagating according to the Burgers equation (which includes thermoviscous losses) are also influenced by finite sampling rates. The effect of discrete sampling on the WSF for an initially sinusoidal signal propagating according to Equation (2.42) may be described by analyzing the Khokhlov solution. Recall that the Khokhlov solution is valid for $3 < \sigma < \Gamma$. We choose to study the Khokhlov solution rather than the Fay solution because the WSF of an arbitrary Fourier series is not known.

Suppose that a wave that is described by the Khokhlov solution (see Section 2.2.3.5) is sampled at a rate of f_s. The discrete sampling indicates that the slope must be estimated to determine the WSF estimate for the discretely sampled Khokhlov solution. Using a finite-difference scheme and the notation from previous sections yields a slope estimate of

$$\left.\frac{\Delta P}{\Delta t}\right|_\theta = \omega \left.\frac{\Delta P}{\Delta \theta}\right|_\theta = \omega \frac{P(\theta + \Delta\theta) - P(\theta)}{\Delta\theta} \tag{3.117}$$

$$= \frac{\omega}{\Delta\theta} \frac{1}{(1+\sigma)}\left[-\Delta\theta + \pi\left(\tanh\left(\frac{2}{\pi}\frac{(\theta+\Delta\theta)}{\psi}\right) - \tanh\left(\frac{2}{\pi}\frac{\theta}{\psi}\right)\right)\right]. \tag{3.118}$$

Since the ratio ν is irrational and the sampling time is very long, we find that the slope estimate at every possible value of $-\pi < \theta < \pi$ will be equally likely. This means that

$$E[\dot{P}^+] = \frac{1}{\Theta_2 - \Theta_1}\int_{\Theta_1}^{\Theta_2} \frac{\Delta P}{\Delta\theta} d\theta = \frac{I_{1,2}}{\Theta_2 - \Theta_1}, \tag{3.119}$$

where Θ_i is the θ location of the i^{th} zero crossing of $\Delta P/\Delta\theta$, and

$$I_{a,b} = \int_a^b \frac{\Delta P}{\Delta\theta} d\theta. \tag{3.120}$$

Similarly,

$$E[\dot{P}^-] = \frac{1}{(\pi - \Theta_2) + (\Theta_1 - (-\pi))}\left[\int_{-\pi}^{\Theta_1} \frac{\Delta P}{\Delta\theta} d\theta + \int_{\Theta_2}^{\pi} \frac{\Delta P}{\Delta\theta} d\theta\right] \tag{3.121}$$

$$= \frac{1}{2\pi - (\Theta_2 - \Theta_1)}\left[I_{-\pi,\pi} - I_{\Theta_1,\Theta_2}\right] = \frac{-I_{\Theta_1,\Theta_2}}{2\pi - (\Theta_2 - \Theta_1)}, \tag{3.122}$$

since $I_{-\pi,\pi} = 0$, because the net pressure difference over a period is zero. The limits of integration, Θ_1 and Θ_2, are the solutions to the equation found by setting Equation (3.118) equal to zero and choosing θ as the variable being solved for. This yields

$$\Theta_1 = \frac{\psi}{\pi}\ln\left(\frac{A_1 - \sqrt{A_2}}{2\Delta\theta}\right) - \Delta\theta \tag{3.123}$$

and

$$\Theta_2 = \frac{\psi}{\pi}\ln\left(\frac{A_1 + \sqrt{A_2}}{2\Delta\theta}\right) - \Delta\theta, \tag{3.124}$$

where

$$A_1 = e^{\pi\Delta t/\psi}(2\pi - \Delta\theta) - (2\pi + \Delta\theta), \tag{3.125}$$

and

$$A_2 = e^{\frac{2\pi\Delta\theta}{\psi}}(2\pi - \Delta\theta)^2 - 2e^{\pi\Delta\theta/\psi}((2\pi)^2 + \Delta\theta^2) + (2\pi + \Delta\theta)^2. \tag{3.126}$$

The Taylor series expansion of A_1 and A_2 in terms of $\Delta\theta$ are

$$A_1 = (\pi^2/\psi - 2)\Delta t + O(\Delta\theta^2) \tag{3.127}$$

and

$$A_2 = 4^2(\pi^4/4\psi^2 - \pi^2/2\psi)\Delta\theta^2 + O(\Delta\theta^3). \tag{3.128}$$

We find that letting $\Delta\theta \to 0$ (or $f_s \to \infty$),

$$\Theta_1|_{\Delta\theta\to 0} = \frac{\psi}{\pi}\ln\left(\pi^2/\psi - 1 - 2\sqrt{\pi^4/4\psi^2 - \pi^2/2\psi}\right) \tag{3.129}$$

$$= -\frac{\psi}{\pi}\ln\left(\frac{\sqrt{\pi^2/2\psi} + \sqrt{\pi^2/2\psi - 1}}{\sqrt{\pi^2/2\psi} - \sqrt{\pi^2/2\psi - 1}}\right) = -\frac{2}{\pi}\psi\tanh^{-1}\sqrt{1 - \frac{2}{\pi^2}\psi} \tag{3.130}$$

and

$$\Theta_2|_{\Delta t\to 0} = \frac{\psi}{\pi}\ln\left(\pi^2/\psi - 1 + 2\sqrt{\pi^4/4\psi^2 - \pi^2/2\psi}\right) \tag{3.131}$$

$$= \frac{\psi}{\pi}\ln\left(\frac{\sqrt{\pi^2/2\psi} + \sqrt{\pi^2/2\psi - 1}}{\sqrt{\pi^2/2\psi} - \sqrt{\pi^2/2\psi - 1}}\right) = \frac{2}{\pi}\psi\tanh^{-1}\sqrt{1 - \frac{2}{\pi^2}\psi}, \tag{3.132}$$

which are the values of Θ_1 and Θ_2 found assuming a continuous sampling.

Taking the above equations into account, we find that the WSF for the discretely sampled Khokhlov solution is

$$\mathrm{WSF} = -\frac{E[\dot{P}^-]}{E[\dot{P}^+]} = -\frac{\dfrac{-I_{\Theta_1,\Theta_2}}{2\pi - (\Theta_2 - \Theta_1)}}{\dfrac{I_{\Theta_1,\Theta_2}}{\Theta_2 - \Theta_1}} = \frac{\Theta_2 - \Theta_1}{2\pi - (\Theta_2 - \Theta_1)} \tag{3.133}$$

$$= \frac{1}{\dfrac{2\pi}{\Theta_2 - \Theta_1} - 1} = [2\pi[\Theta_2 - \Theta_1]^{-1} - 1]^{-1} \tag{3.134}$$

$$= \left[2\pi\left[\frac{\psi}{\pi}\ln\left(\frac{A_1+\sqrt{A_2}}{2\Delta\theta}\right)-\frac{\psi}{\pi}\ln\left(\frac{A_1-\sqrt{A_2}}{2\Delta\theta}\right)\right]^{-1}-1\right]^{-1} \tag{3.135}$$

$$= \left[2\pi\left[\frac{\psi}{\pi}\ln\left(\frac{A_1+\sqrt{A_2}}{A_1-\sqrt{A_2}}\right)\right]^{-1}-1\right]^{-1} = \left[\left[\frac{\psi}{\pi^2}\tanh^{-1}\frac{\sqrt{A_2}}{A_1}\right]^{-1}-1\right]^{-1}. \tag{3.136}$$

We now replace A_1 and A_2 with their definitions:

$$\mathrm{WSF} = \left[\frac{\psi}{\pi^2}\left[\tanh^{-1}\frac{\sqrt{e^{2\pi\Delta\theta/\psi}(2\pi-\Delta\theta)^2-2e^{\pi\Delta\theta/\psi}((2\pi)^2+\Delta\theta^2)+(2\pi+\Delta\theta)^2}}{e^{\pi\Delta t/\psi}(2\pi-\Delta\theta)-(2\pi+\Delta\theta)}\right]^{-1}-1\right]^{-1}. \tag{3.137}$$

Recalling that $\Delta\theta = 2\pi/\nu$, the WSF may be written as

$$\mathrm{WSF} = \left[\left(\frac{\psi}{\pi^2}\tanh^{-1}\frac{\sqrt{e^{4\pi^2/\psi\nu}\left(1-\frac{1}{\nu}\right)^2-2e^{2\pi^2/\psi\nu}\left(1+\frac{1}{\nu^2}\right)+\left(1+\frac{1}{\nu}\right)^2}}{e^{2\pi^2/\psi\nu}\left(1-\frac{1}{\nu}\right)-\left(1+\frac{1}{\nu}\right)}\right)^{-1}-1\right]^{-1}. \tag{3.138}$$

Another way to write Equation (3.138) is

$$\mathrm{WSF} = \left[\left(\frac{1}{\pi^2}\psi\tanh^{-1}\frac{\sqrt{\left(1+\frac{1}{\nu^2}\right)\sinh^2\left(\frac{\pi^2}{\psi\nu}\right)-\frac{1}{\nu}\sinh\left(\frac{2\pi^2}{\psi\nu}\right)}}{\sinh\left(\frac{\pi^2}{\psi\nu}\right)-\frac{1}{\nu}\cosh\left(\frac{\pi^2}{\psi\nu}\right)}\right)^{-1}-1\right]^{-1}. \tag{3.139}$$

For reference, the exact WSF, found by assuming continuous sampling, was found to be

$$\mathrm{WSF} = \left[\left(\frac{2}{\pi^2}\psi\tanh^{-1}\sqrt{1-\frac{2}{\pi^2}\psi}\right)^{-1}-1\right]^{-1}. \tag{3.140}$$

The estimates of the WSF for the Khokhlov solution are plotted as a function of σ assuming $\Gamma = 10^3$ in Figure 3.7, below. Due to the ratios of large numbers associated with Equation (3.139), the estimates plotted in Figure 3.7 are not complete. Since the estimates are not well known near the sawtooth propagation regime (σ near 3) and the WSF values are expected to approach the WSF value for a sawtooth wave, the WSF of a sawtooth wave is plotted in place of the portions of the WSF estimates that were not easily calculable.

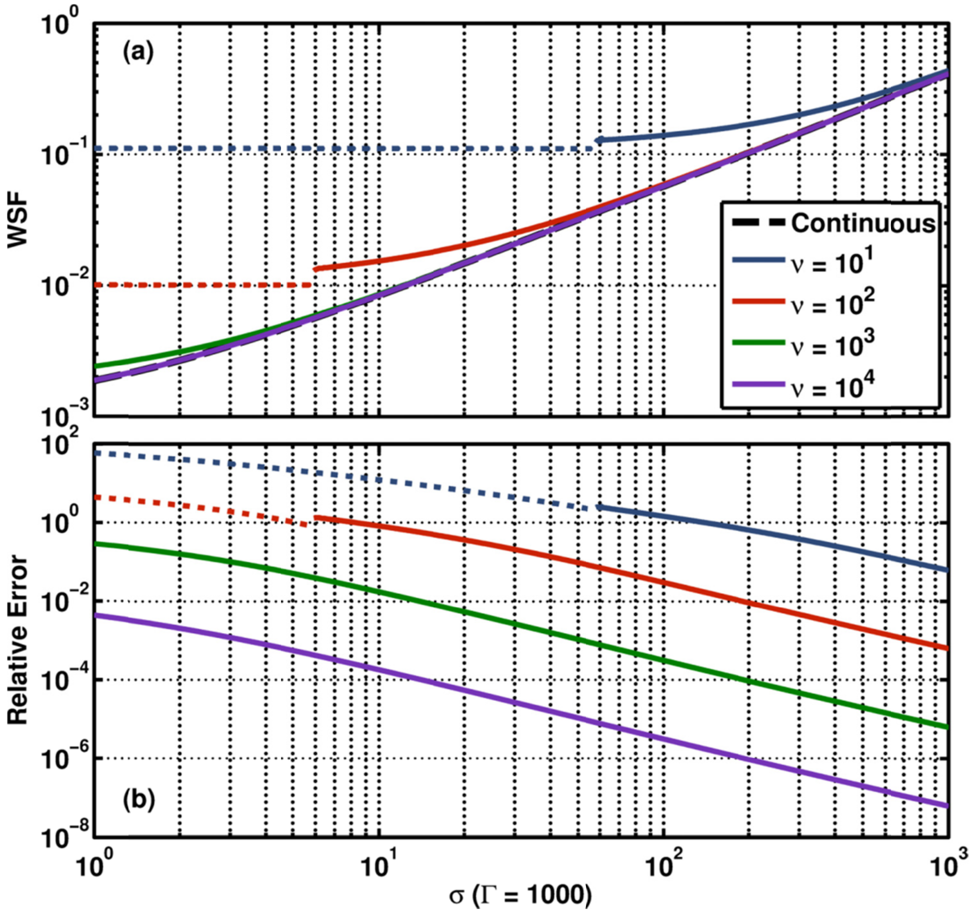

Figure 3.7. (a) Estimates of the wave steepening factor (WSF) of the Khokhlov solution for $\nu = 10^1,\ 10^2, 10^3$, and 10^4. The dashed lines denote the WSF of a sawtooth wave. The exact WSF derived from using continuous sampling is plotted as the black dashed line, for comparison. (b) The relative error of the estimates in (a). The relative error is defined as $|1 - \mathrm{WSF}_\nu / \mathrm{WSF}_{\mathrm{cont}}|$.

For σ near Γ (the upper limit of applicability of the Khokhlov solution), the estimates of the WSF shown in Figure 3.7 are all very close to the actual value. However, for waveforms with significant shock content, namely $\sigma \ll \Gamma$, the estimates based on lower sampling rates overestimate the true WSF quite significantly. In this limit, which is often called the sawtooth limit, the estimate of the WSF of a sawtooth wave (shown as colored dotted lines in Figure 3.7) is approached. Note that if the estimated WSF value approaches the sawtooth wave limit, it is a poor representation of the actual WSF. However, WSF estimates that are about four times the sawtooth limit are fairly close to the actual WSF value (relative error $< 10^{-1}$) for each value of ν considered in Figure 3.7. Thus, a simple rule of thumb is if a WSF estimate is at least four times larger than the sawtooth limit, it is likely to represent the true WSF value well.

The lack of temporal resolution near shocks is not the only concern with the WSF as a metric for shock content in noise. The calculation of the values of the WSF for ideal cases, such as sinusoids and sawtooth waves, is fairly straight-forward, but the behavior of the WSF for cases which are not ideal is likely to be more complicated. For example, it is currently unknown whether an absolute error of about 1%, which was calculated above, is a significant error for noise or not. In addition, there is no documentation of the evolution of the WSF for initially Gaussian noise propagation to the authors' knowledge. The uncertainty of the actual value of the WSF due to potentially insufficient temporal resolution and the lack of understanding of how to interpret a given value of the WSF of a waveform suggest that more study of the WSF is needed before it can be effectively used as a metric to study jet noise.

3.3.3 Derivative Skewness

Now we turn our attention to the effects of finite sampling rates on the estimation of the derivative skewness. The Fubini solution, a sawtooth wave, and the Fay solution will be considered. The effects of discrete sampling on the estimate of the derivative skewness of a waveform are particularly of interest, since the cubic nature of the skewness may greatly emphasize any low-resolution pressure rises.

3.3.3.1 Fubini Solution

Begin by looking at the Fubini solution described in Section 2.2.2.2, which is used to describe the propagation of an initially sinusoidal signal before shocks form. The estimate of the derivative skewness of the Fubini solution sampled with a normalized uniform time step

$\Delta\theta = 2\pi/\nu$ may be written as Equation (3.51) where $A_n = A'_n$ and $B_n = B'_n$ from Equation (3.76), and

$$B_n = \frac{2}{n\sigma} J_n(n\sigma). \tag{3.141}$$

The derivative skewness estimates of the Fubini solution with various values of ν is plotted in Figure 3.8(a), and the errors of the estimates relative to the exact derivative skewness obtained with continuous sampling are plotted in Figure 3.8(b). The number of terms used in each infinite summations is five times the value of ν. The abscissas used in Figure 3.8 are logarithmic, approaching one from negative infinity.

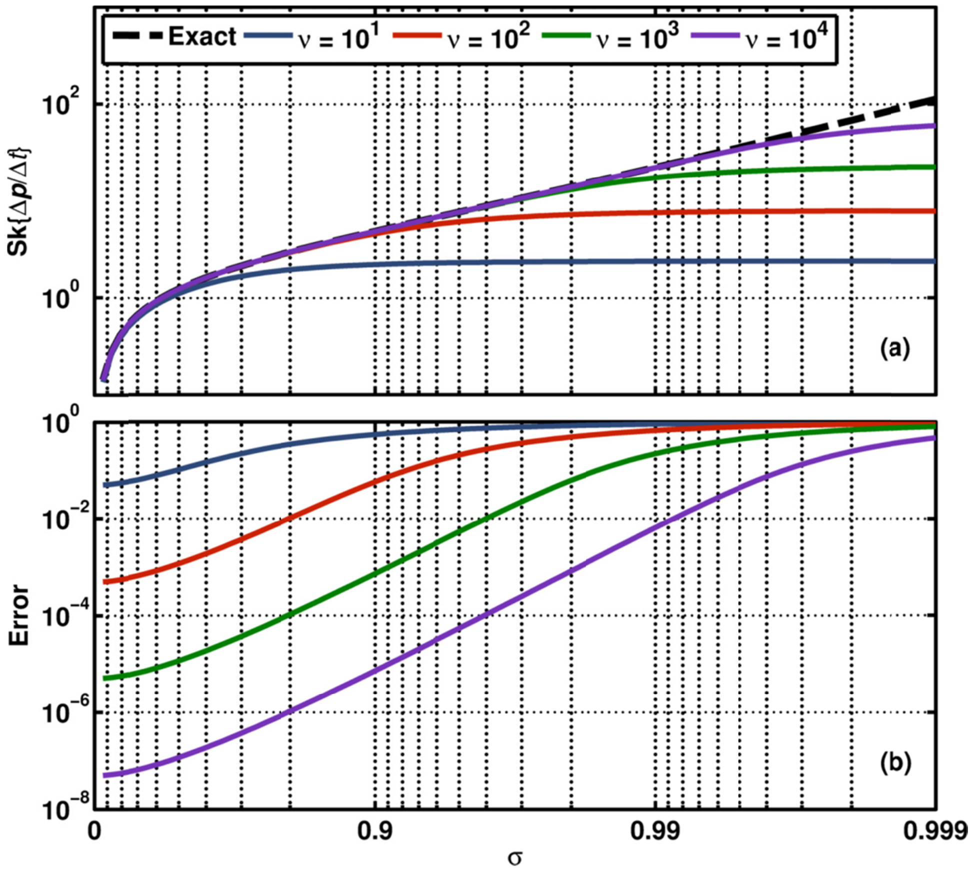

Figure 3.8. (a) Estimates of the derivative skewness of the Fubini solution for $\nu = 10^1$, $10^2, 10^3$, and 10^4. The exact derivative skewness derived from using continuous sampling is plotted for comparison. (b) The relative error of the estimates in (a). The relative error is defined as $|1 - \mathrm{Sk}\{\Delta P/\Delta\theta\}/\mathrm{Sk}\{\partial P/\partial\theta\}|$, where the Δ's indicate discrete sampling and the ∂'s indicate continuous sampling.

The derivative skewness estimates in Figure 3.8 all level off before reaching the maximum values, which are the values of the estimates at $\sigma = 1$. The exact value of the derivative skewness, based on continuous sampling, continues to increase as predicted in Equation (3.64). The divergent nature of the exact derivative skewness suggests that for σ sufficiently close to one, a derivative skewness estimate with any finite sampling rate will cease to be a good approximation of the actual derivative skewness value. This can be seen in the error plot in Figure 3.8(b). We see that the reliability of the derivative skewness estimates depends on the relationship between ν and σ. For example, for $\nu = 10$ the derivative skewness is never more accurate than 1% relative error, but for $\nu = 1000$ is more accurate than 1% relative error until about $\sigma = 0.93$. The physical interpretation of this phenomenon is that no reasonable finite sampling rate can adequately estimate the derivative skewness of a waveform that contains true discontinuities.

3.3.3.2 Sawtooth Wave

For $\sigma > 3$, an initially sinusoidal plane wave propagating without linear losses may be approximately modeled as a sawtooth wave, which has been defined in Equation (2.25). In order to estimate the derivative skewness, Equation (3.2) can be further expanded to the form

$$\mathrm{Sk}\{x\} = \lim_{N\to\infty} \frac{\frac{1}{N}\sum_n^N x_n^3}{\left[\frac{1}{N}\sum_n^N x_n^2\right]^{\frac{3}{2}}}. \tag{3.142}$$

To understand the error in the derivative skewness estimate, consider again the sawtooth wave defined in Equation (2.25). In Section 3.3.2.2 we found that, on average, the number of data points per period is $N = f_s/f$, with $N - 1$ of those data points being associated with the ramp of the wave with a slope of $-2fp_0$, and one data point associated with the shock with a slope of $2fp_0(f_s - f)$. Then, by replacing the random variable x in Equation (3.142) with the time-derivative of pressure estimates of the discretely sampled sawtooth wave, we may calculate a derivative skewness estimate:

$$\mathrm{Sk}\left\{\frac{\Delta S_n}{\Delta t}\right\} = \frac{\frac{1}{N}\left[(N-1)(-2fS_0)^3 + (2fS_0)^3(f_s - f)^3\right]}{\left[\frac{1}{N}\left[(N-1)(-2fS_0)^2 + (2fS_0)^2(f_s - f)^2\right]\right]^{\frac{3}{2}}}. \tag{3.143}$$

Simplifying Eqaution (19), the skewness becomes

$$\mathrm{Sk}\left\{\frac{\Delta S_n}{\Delta t}\right\} = \frac{f_s - 2f}{\sqrt{f(f_s - f)}} = \frac{\nu - 2}{\sqrt{\nu - 1}}. \tag{3.144}$$

As expected, in the limit that $f_s \to \infty$, the derivative skewness of the sawtooth wave also diverges. Since the actual derivative skewness is indefinite, defining a relative error does not make sense. However, the estimated derivative skewness can be calculated for a characteristic case, which would give some intuition as to the expected values. Given $\nu = 100$, the derivative skewness of a sawtooth wave would be expected to be about 10.

A last comment: recall that the sawtooth wave and the Fubini solution have been based on the assumption of no linear losses in propagation. Since any real system will include linear losses, no true discontinuities can form in a waveform, regardless of the initial amplitude or propagation distance. This implies that the waveform described by the Earnshaw or Fubini solutions for $\sigma = 1$ is pathological. While propagation without linear losses is a useful analysis tool, it does not occur in realistic waveforms. Other models, such as the Mendousse or Fay solutions, must be used to understand some of the effects of linear losses on the estimation of the derivative skewness of a waveform containing shocks.

3.3.3.3 Fay Solution

The estimate of the derivative skewness of the Fay solution sampled with a normalized uniform time step $\Delta\theta = 2\pi/\nu$ may be written as Equation (3.51) with Equation (3.76), where

$$B_n = \frac{2/\Gamma}{\sinh(n\psi)}, \tag{3.145}$$

and $\psi = (1+\sigma)/\Gamma$. The derivative skewness estimates of the Fay solution with various values of ν is plotted in Figure 3.9(a), and the errors of the estimates relative to the exact derivative skewness obtained with continuous sampling are plotted in Figure 3.9(b). The number of terms used in the infinite summations is five times the value of ν.

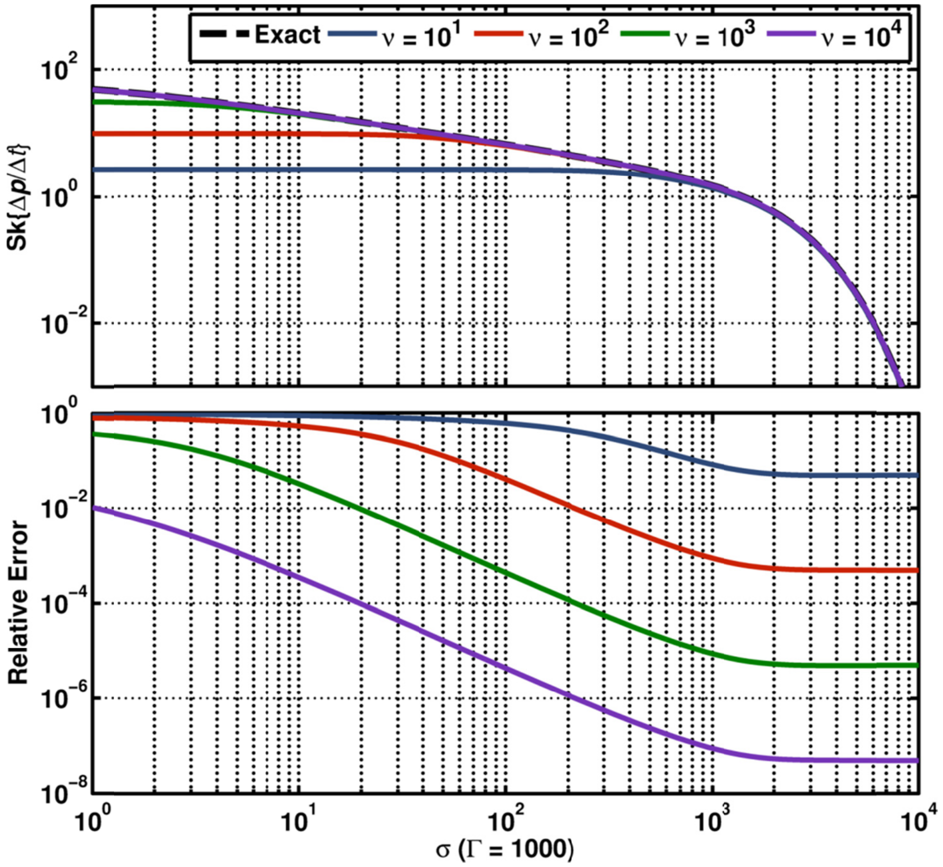

Figure 3.9. (a) Estimates of the derivative skewness of the Fay solution plotted as a function of σ for $\nu = 10^1,\ 10^2,\ 10^3$, and 10^4, with a Gol'dberg number of 1000. The exact derivative skewness derived from using continuous sampling is plotted for comparison. (b) The relative error of the estimates in (a). The relative error is defined as $|1 - \mathrm{Sk}\{\Delta P/\Delta\theta\}/\mathrm{Sk}\{\partial P/\partial\theta\}|$, where the Δ's indicate discrete sampling and the ∂'s indicate continuous sampling.

The derivative skewness estimates shown in Figure 3.9(a) show similar results to the derivative skewness estimates based on the Fubini solution, shown in Figure 3.8(a). For $\sigma < \Gamma$

(the sawtooth regime), the derivative skewness estimates at larger values of σ will be more accurately described. This is most likely due to the significant shocks that are present in waveforms during this regime. For $\sigma > \Gamma$ (transition from the sawtooth and the old-age propagation regime), the accuracy of the derivative skewness estimate for a given value of ν appears to be constant. This may be due to the very small derivative skewness values associated with the Fay solution for large values of σ.

3.4 Summary and Conclusions

The analytic discussions of the measures of nonlinearity given in this chapter provide a better framework to interpret these measures for more complicated waveforms. The idealized cases introduced in Chapter 2 have been used to explore the evolution of measures as a waveform propagates, giving a general estimate of the rate of evolution that one would expect for measured data. Also, an analysis of the effects of under-sampling a waveform on the measures of nonlinearity suggests ways to verify that a given sampling rate is sufficient to adequately represent a measure of nonlinearity.

The first metric considered was the wave steepening factor (WSF), which may be considered a measure of the waveform distortion characteristic of nonlinear propagation. The analysis of the WSF has shown that periodic waveforms with a WSF value above about 0.75 are not likely to have been distorted by nonlinear effects very much. Waveforms that have WSF values below about 0.25 are likely to have experienced nonlinear distortion. In addition, the importance of nonlinear distortion in a waveform increases dramatically as the WSF value approaches zero. When considering the sampling rate, if the value of the WSF of a waveform is less than four times the lower limit of the WSF based on assuming a sawtooth wave, the sampling rate is probably too low to accurately gauge the WSF.

In addition to the WSF, calculations of the pressure and derivative skewness, measures of the asymmetry of the probability density function of the pressure amplitudes and time derivatives of the pressure amplitudes, respectively, of idealized cases were analyzed. The derivative skewness was shown to vary significantly. At about 0.85 times the shock formation distance the derivative skewness of a lossless initially sinusoidal plane wave began to dramatically rise. A derivative skewness value of 0.5 may be considered low and indicate that nonlinear distortion has not affected the waveform significantly, while a derivative skewness value of 5 may be considered high, and that nonlinear distortion has affected the waveform significantly. It should be noted that insufficient temporal resolution will cause the derivative skewness estimate to be significantly less than the actual derivative skewness value for a waveform.

Both the WSF and derivative skewness can be used to analyze the importance of nonlinearity in propagating waveforms. The WSF is useful due to the fact that it is relatively robust with respect to limited sampling rates, while the cubic nature of the derivative skewness causes it to be relatively sensitive to insufficient temporal resolution. On the other hand, the relatively dramatic variation in the derivative skewness near the shock formation distance and as a waveform transitions to the old-age region suggest that the derivative skewness may give more information about the nonlinearity in a propagating waveform.

Chapter 4

Numerical Analysis of Nonlinearity Measures

4.1 Introduction

The model equations described in Chapter 2 and the analyses of the nonlinearity metrics presented in Chapter 3 are important, limiting cases. However, actual noise propagation is much more complicated, as will be shown in Chapter 5 and Chapter 6, with waveforms measured from plane wave tube experiments and jet noise measurements, respectively. In addition to the propagation phenomena that are expected, such as boundary layer absorption and dispersion plane wave tube propagation, and frequency-dependent geometrical spreading for full scale jet noise, measured results often include unexpected phenomena, such as digital noise and source distortion. One way to isolate these unknown phenomena in measured data is to first model the physical waveforms using numerical methods, and then compare the predictions with the measurements.

The purpose of this chapter is to use a numerical model of noise propagation to connect the analytical results from Chapter 2 and Chapter 3 to the measured data presented in Chapter 5 and Chapter 6. To this end, three different numerical experiments are presented in this chapter.

First, predicted waveforms based on an initially sinusoidal plane wave propagating with thermoviscous losses will be considered. Then, predicted waveforms based on an initially sinusoidal wave and initially broadband noise propagating with linear losses similar to propagation in a plane wave tube will be discussed. These last two cases are similar to the physical experiments discussed in Chapter 5. For each of the cases discussed, the effects of nonlinearity in the waveforms, spectra, and the nonlinearity metrics described in Chapter 3 are discussed.

4.2 Numerical Model of Propagation

Modeling of nonlinearity in broadband noise propagation dates back to work by Pernet and Payne [2] who examined anomalously low absorption of high-frequency energy in the spectrum for noise of sufficient intensity. Pestorius and Blackstock [9] developed a time-waveform propagation model based on the generalized Burgers equation (GBE) [4] and successfully modeled noise propagation, including shock formation and coalescence, in a long pipe. Additional arbitrary waveform modeling developments took place in the context of nonlinear sonic boom propagation, [50] [51] [52] but much of the recent interest has been the noise propagation from modern high-performance tactical aircraft. Nonlinear F/A-18E noise propagation was calculated by Gee *et al.*, [21] Brouwer, [53] and Saxena *et al.* [54] using different GBE-based algorithms. A more comprehensive treatment of the noise radiated by the F-22A Raptor was carried out by Gee *et al.* [23] [22] and algorithm refinements were incorporated in a study of the noise propagation from the F-35AA Joint Strike Fighter. [24] In these latter studies of F-22A and F-35AA noise, excellent agreement between nonlinear models and measurements were achieved at a maximum comparison distance of 305 m (1000 ft).

The GBE algorithm used previously by Gee *et al.* [24] has been employed to model the nonlinear propagation of various signals in this chapter. This algorithm is a combined time-frequency domain propagation scheme. First, a waveform is propagated forward a spatial step in the time domain according to the Earnshaw solution and weak shock theory. The size of the spatial step varies, depending on the amplitude of the sound signal at the present location. After the waveform has been propagated in the time domain, the linear absorption and dispersion associated with the nonlinear step is applied in the frequency domain. The waveform thus propagates, alternating between the time and frequency domains and nonlinear and linear processes, until the desired propagation distance is reached.

4.3 Numerical Experiments

A good place to begin with modeling nonlinear propagation is with initially sinusoidal waveforms. First, we will consider propagation with thermoviscous losses, and then propagation in a plane-wave-tube environment. For both of these conditions, comparisons are made with the analytical and limiting solutions discussed in Chapter 2.

4.3.1 Thermoviscous Propagation of an Initially Sinusoidal Signal

The first case that is considered numerically is also a problem that has an analytical solution. In particular, this is the initially sinusoidal plane wave propagating with thermoviscous losses. As stated in Chapter 2, the exact solution is the Mendousse solution. The input waveform consists of a sine wave sampled at 204 800 samples/s (to mimic the plane wave tube tests described in Chapter 5) for 1.28 s. This sampling rate and waveform time duration are the same for all of the numerical experiments described in this chapter. In order to understand how different values of Gol'dberg number affect the evolution of the nonlinearity metrics described in Chapter 3, the numerical experiment is carried out for $\Gamma = 10$ and for $\Gamma = 1000$.

Since many of the results in Chapter 3 rely on the ratio of the sampling frequency to the characteristic frequency $\nu = f_s/f_c$ being an irrational number, the frequency of the sine wave was chosen to be 500π Hz (about 1570 Hz). Therefore, the value of ν is approximately 130.4.

The atmospheric conditions, sampling rates, and absorption coefficients used for the numerical experiments described in this chapter are summarized in Table 4.1, below.

Table 4.1. Summary of conditions used in numerical experiments described in Chapter 4.

	Atmospheric Propagation	Plane Wave Tube Propagation
Temperature	293.15 K	293.15 K
Atm. Pressure	0.85 atm.	0.85 atm.
Relative Humidity	20%	20%
Tube Radius		2.54 cm
Sample Length	0.78 s	0.78 s
Sampling Frequency	204 800 Samples/s	204 800 Samples/s
Characteristic Frequency	500π Hz (≈ 1571 Hz)	500π Hz (≈ 1571 Hz)
Absorption (Real Part)	13.3×10^{-3} dB/m (at 500π Hz)	0.415 dB/m (at 500π Hz)

Portions of the numerically predicted waveforms are plotted in Figure 4.1. The portions of the waveforms associated with $\Gamma = 10$ steepen less quickly and to a lesser extent than the portions associated with $\Gamma = 1000$. In addition, the portions of the waveforms associated with $\Gamma = 10$ have significantly unsteepened by $\sigma = 2^4$, whereas the portions associated with $\Gamma = 1000$ do not appear to have unsteepened at all. Since the Gol'dberg number quantifies the importance of nonlinear effects relative to absorptive effects, the more significant and longer lasting shocks associated with the greater Gol'dberg number is expected.

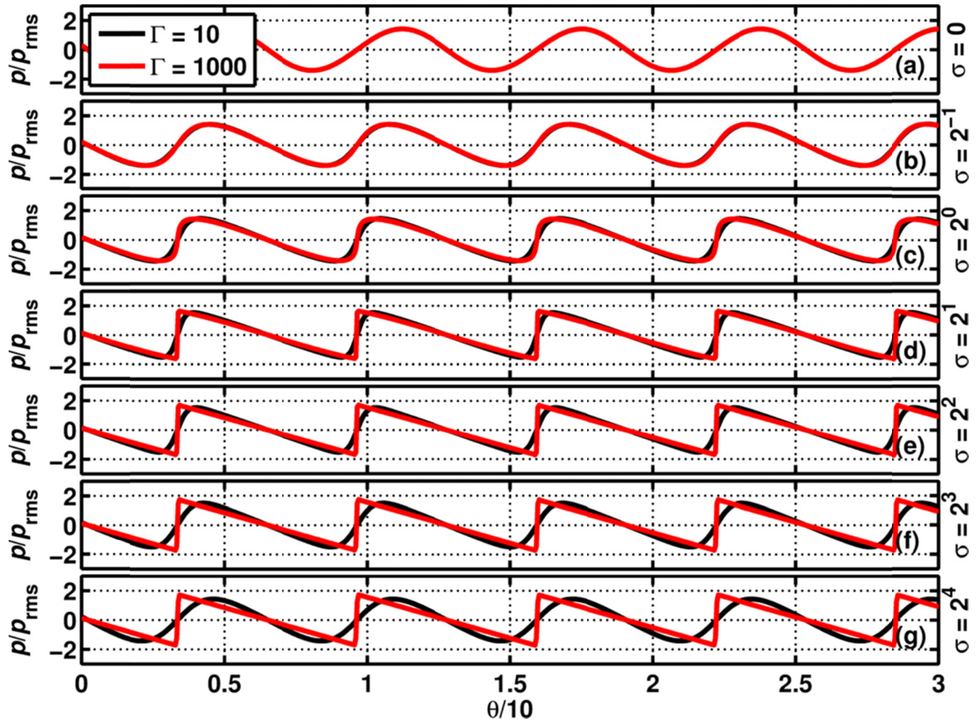

Figure 4.1. Portions of the waveforms predicted by numerically propagating an initially sinusoidal plane wave to various values of σ with thermoviscous losses and a Gol'dberg number of 10 (black lines) and 1000 (red lines).

The amplitudes of the harmonics of the predicted waveforms for a Gol'dberg number of 10 relative to the initial amplitude are plotted in Figure 4.2. The fact that there is energy at any of the higher harmonics for $\sigma > 0$ is indicative of the importance of nonlinearity in the wave propagation. Also, the fact that the rate of decrease of the relative amplitudes increases overall as σ becomes large indicates that the thermoviscous losses also play an important role.

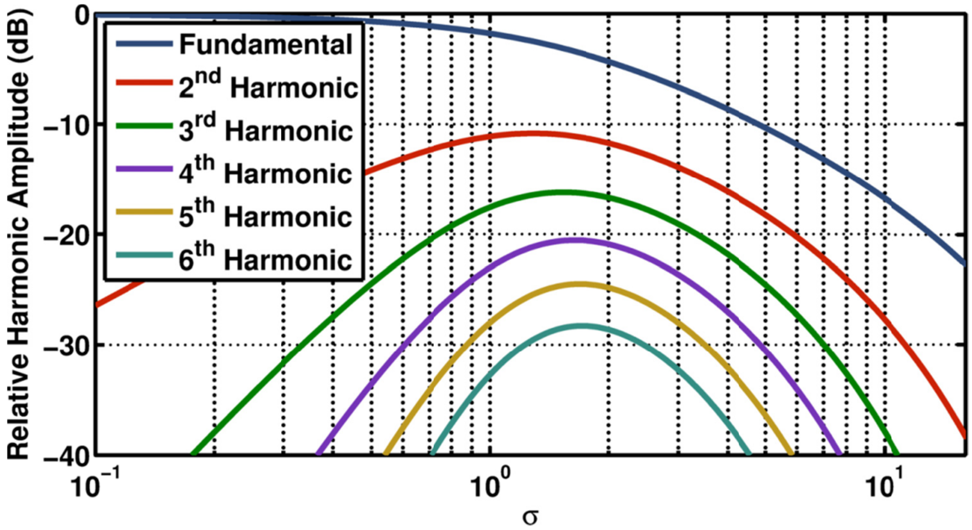

Figure 4.2. The first six harmonic amplitudes of waveforms predicted by numerically propagating an initially sinusoidal plane wave to various values of σ with thermoviscous losses. The amplitudes are plotted in dB relative to the amplitude of the initial signal. The Gol'dberg number of the source signal is 10.

The first nonlinearity metric that is considered for the numerical propagation of an initially sinusoidal plane wave with thermoviscous losses is the wave steepening factor. The WSF of the numerically propagated wave is plotted in Figure 4.3 as a function of σ, as well as the WSF derived from the Earnshaw solution and the WSF of the discretely-sampled Khokhlov solution given the value of ν used in this experiment for both $\Gamma = 10$ and $\Gamma = 1000$. Recall that the Khokhlov solution is used for WSF comparisons because there is an analytical form of the WSF for the Khokhlov solution, while no analytical form for the Fay solution (which is more generally applicable than the Khokhlov solution).

The numerically predicted values of the WSF follow the trends predicted by the analytical results of Chapter 3. For small values of σ the numerically predicted values of the WSF follow the trend predicted by the Earnshaw solution very closely for both Gol'dberg numbers. This is due to the fact that the waveforms have high amplitudes, and the nonlinearity dominates the absorptive effects. However, as the waveform associated with $\Gamma = 10$ approaches $\sigma = 1$ (the shock formation distance) the numerically predicted WSF values become higher than the predictions of the Earnshaw solution. This is due to the fact that the higher harmonics in the waveform, which have been nonlinearly generated, have much greater absorption than the fundamental frequency. These higher harmonics are attenuated, and the waveform slows its nonlinear steepening trend. The WSF values associated with the waveform with $\Gamma = 1000$, on the other hand, do not increase at all for the range shown, and stay close to the Earnshaw solution all the way to $\sigma = 16$, which is the end of the range shown. While the higher harmonics are being attenuated for this case as well, the higher amplitudes transfer energy to the higher harmonics fast enough to counter the effects of absorption.

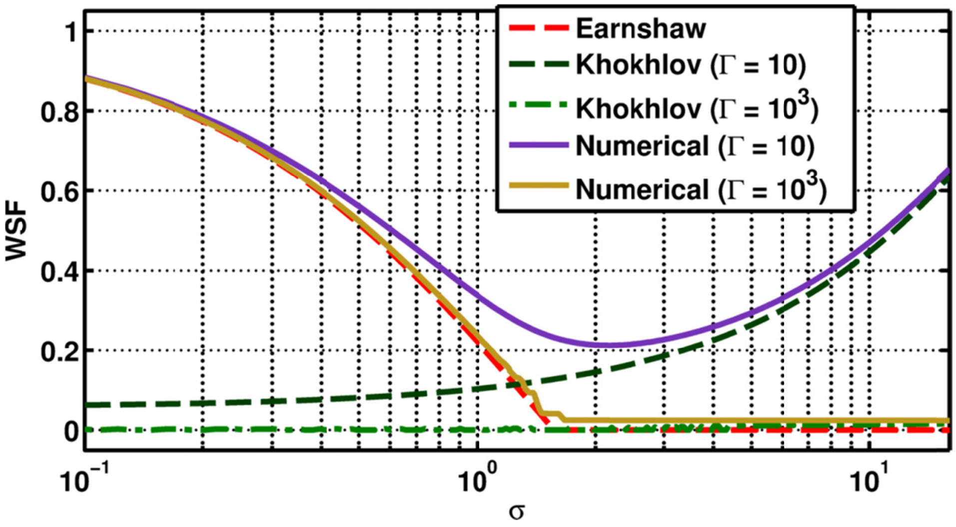

Figure 4.3. Estimates of the wave steepening factor (WSF) of waveforms predicted by numerically propagating an initially sinusoidal plane wave to various values of *σ* with thermoviscous losses.

Near $\sigma = 2$ the numerically predicted values of the WSF of the waveform with $\Gamma = 10$ reach a minimum, and begin to increase. This increase is because the absorptive effects have started to dominate the nonlinear effects, and the waveform is beginning to unsteepen. For $\sigma > 3$, the Khokhlov solution is a better representation of the physical waveforms, and correspondingly the numerically predicted values of the WSF begin to follow the trend predicted by the Khokhlov solution. The waveforms were predicted as far as $\sigma = 16$. For these large values of σ, the $\Gamma = 10$ waveform has unsteepened so that it is out of the sawtooth regime and is beginning to enter the old-age regime. Since the Khokhlov solution is not valid in the old-age regime, if the waveform were propagated further, it is expected that the WSF values predicted by the numerical model would diverge from the Khokhlov solution beyond $\sigma = 16$. The WSF values of the $\Gamma = 1000$ waveform, on the other hand, are likely to be well approximated by the trend predicted by the Khokhlov solution as far out as $\sigma = 1700$.

In addition to the WSF, the derivative skewness was estimated for the $\Gamma = 10$ and $\Gamma = 1000$ initially sinusoidal waveforms. The derivative skewness estimates are plotted in Figure 4.4 as a function of σ, along with the derivative skewness values predicted by the "lossless" Earnshaw solution and the discretely-sampled "lossy" Fay solution, both with $\Gamma = 10$ and with $\Gamma = 1000$. The number of terms used in the Fay solution is five times ν, or 650 terms. Similar to the estimated WSF values, the derivative skewness estimates of both waveforms follow the trend of the Earnshaw solution for very small σ. For the waveform with a Gol'dberg number of 10, as the waveform approaches the shock formation distance, the high harmonics begin to be more significantly attenuated due to the thermoviscous effects, and the waveform slows its steepening process, thus slowing the increase of the derivative skewness. Shortly after the shock formation distance, the lower amplitude waveform has completely stopped steepening, and is beginning to unsteepen, causing the derivative skewness to begin to decrease. As the propagation continues, the derivative skewness of the numerical case begins to follow the trend predicted by the Fay solution. Unlike the Khokhlov solution, the Fay solution is valid even in the old-age regime, and so it is expected that if the waveform were propagated further, the predicted values of the derivative skewness would continue to follow the trend predicted by the Fay solution.

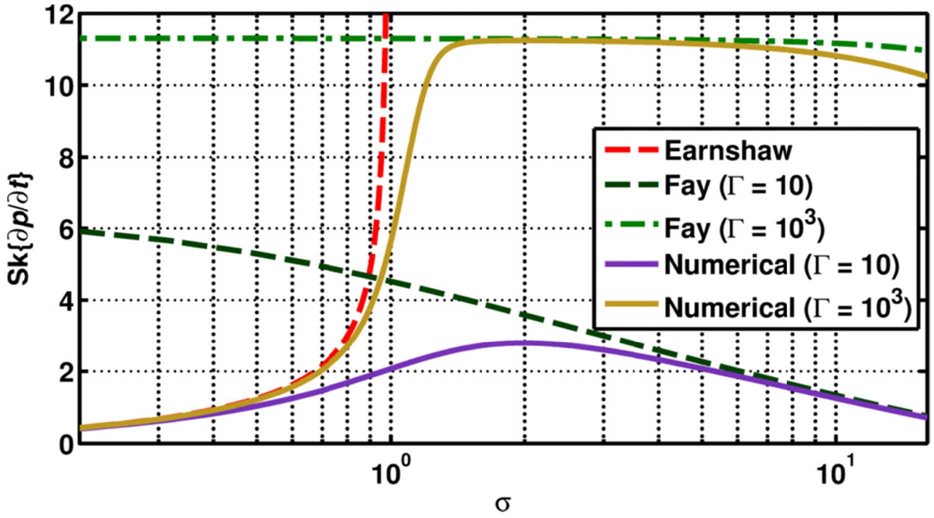

Figure 4.4. Estimates of the derivative skewness of waveforms predicted by numerically propagating an initially sinusoidal plane wave to various values of σ with thermoviscous losses.

The waveform with a Gol'dberg number of 1000, on the other hand, somewhat abruptly reaches a maximum value of about 11.2 at about $\sigma = 1.4$. This is the limit that the Fay solution predicts for $\Gamma = 1000$, assuming a value of $\nu = 130$. In addition, the upper limit of the derivative skewness estimate for a discretely sampled sawtooth wave with a ν value of 130 is about 11.3, suggesting that this upper limit is most likely due to finite sampling effects, rather than physical phenomena. About $\sigma = 7$, the derivative skewness of the higher amplitude waveform departs from the trend predicted by the Fay solution. This means that the waveform predicted by numerical model has begun to unsteepen a little by this distance, such that the finite sampling rate used is more likely to be sufficient to estimate the derivative skewness.

4.3.2 Plane Wave Tube Propagation of an Initially Sinusoidal Signal

The initially sinusoidal plane wave propagating with losses similar to that of a plane wave tube is of interest for three main reasons. First, plane wave tubes are easily realized physically, and which provides a suitable way to experimentally verify the analytical and numerical theory that has is described in this thesis. The comparison of physical and numerical plane wave tube measurements, especially of nonlinearity measures, is given in Chapter 5. The second reason is that the absorption due to the boundary-layer effects associated with sound propagation in a duct increases with the square root of frequency, rather than the square of the frequency as in the case of thermoviscous and high-frequency atmospheric absorption. As low-frequency absorption coefficients are dominated by boundary-layer effects, and high-frequency absorption coefficients will be dominated by atmospheric propagation effects (the cross-over frequency is about 156 kHz; see Section 2.2.3.1), the plane-wave-tube environment is a fascinating case study in terms of absorption. Finally, losses due to both boundary-layer effects and atmospheric propagation include dispersive phenomena. This is a phenomenon that is very difficult to understand analytically, [6] [55] and so numerical and physical experiments are the primary method for understanding dispersion. The choice of the sinusoidal plane wave as the input waveform allows for a ready comparison of the predicted waveforms with the previous case of an initially sinusoidal signal propagating with thermoviscous absorption.

A Gol'dberg number of 10 is chosen for the numerical plane wave tube propagation experiment. The absorption coefficient of the initial sine wave frequency (500π Hz) is about $0.048\ \mathrm{m}^{-1}$, and so the initial amplitude is about 166 Pa. Portions of the input waveform and the waveforms predicted at different distances assuming plane-wave-tube-like propagation are plotted in Figure 4.5, along with the Mendousse solution (the exact solution given only thermoviscous absorption), for comparison.

The first thing to notice about the waveforms presented in Figure 4.5 is that the steep portions of the waveform (the shocks at $\theta = 0, 1, 2,$ and 3) are sharper for the plane wave tube predictions than for the Mendousse solution, especially for $\sigma \geq 1$. This is likely due to the fact that the absorption coefficients of the higher harmonics are relatively smaller for the plane wave tube absorption than for thermoviscous absorption. Also notice that tops of the shocks are more rounded than the bottoms. This phenomenon has been observed by Webster and Blackstock [6] and Blackstock, [10] and has been attributed to the dispersive nature of the propagation. The dispersion is also likely the reason that the predicted shock fronts have a slight delay relative to the Mendousse solution.

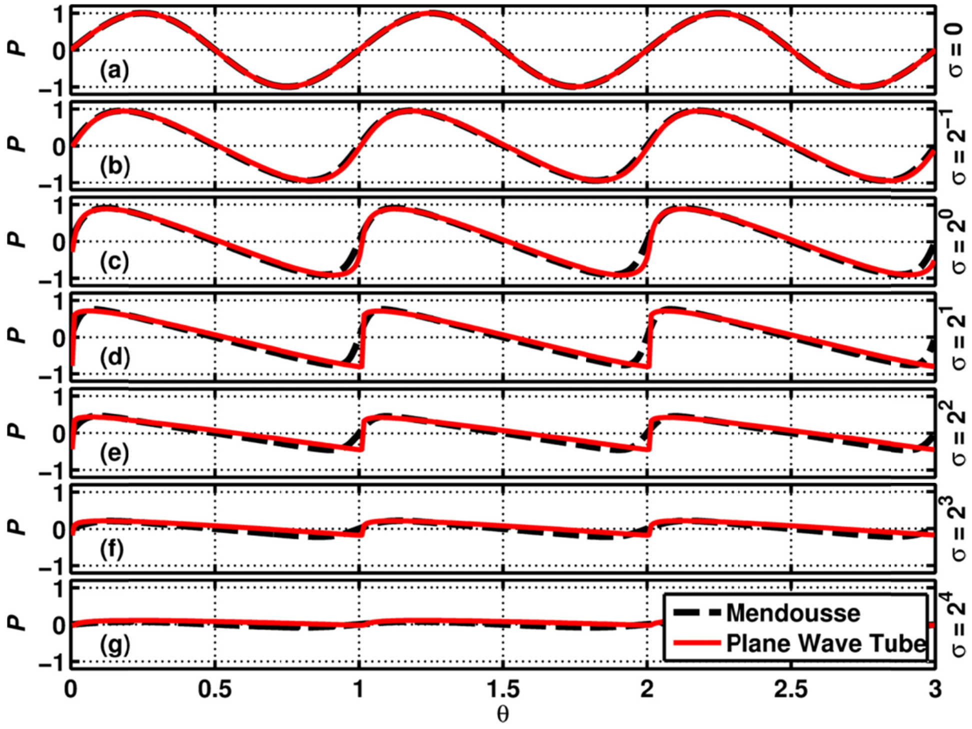

Figure 4.5. Portions of the waveforms predicted by numerically propagating an initially sinusoidal plane wave to various values of σ with linear losses similar to those of propagation in a plane wave tube (red), with the Mendousse solution (only thermoviscous absorption) plotted (dashed black), for comparison. The Gol'dberg number used for this plot is 10.

The harmonic amplitudes of the predicted waveforms relative to the input waveform amplitude are presented in Figure 4.6. The main difference between the harmonic amplitudes predicted using thermoviscous absorption shown in Figure 4.2 and the harmonic amplitudes predicted using plane-wave-tube-like absorption is that the amplitudes of the higher harmonics are much closer to the lower harmonic amplitudes than in the thermoviscous case. The relatively large high-harmonic amplitudes associated with the plane-wave-tube propagation prediction is likely due to the fact that the high-frequency absorption is not as large relative to the absorption of the fundamental frequency, making nonlinear processes more important in the propagation prediction than the thermoviscous predictions. As mentioned in Chapter 2, the boundary layer absorption (for low to moderate frequencies) increases as $\sqrt{f}$ rather than the rate of f^2 associated with thermoviscous absorption.

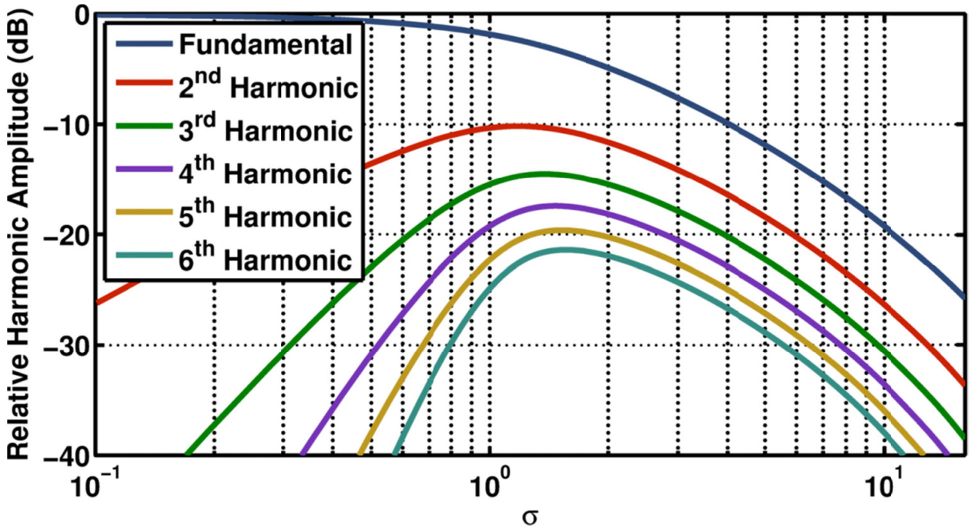

Figure 4.6. The first six harmonic amplitudes of waveforms predicted by numerically propagating an initially sinusoidal plane wave to various values of σ with linear losses similar to those of propagation in a plane wave tube. The Gol'dberg number used for this plot is 10.

The WSF values predicted by the plane wave tube model show similar trends as the WSF values predicted by the thermoviscous propagation model, but differ in the details. The WSF values predicted by the plane wave tube model are plotted in Figure 4.7 as a function of the absorption distance, and the WSF values of the Earnshaw solution and the discretely-sampled Khokhlov solution are plotted for reference. Similar to the WSF values predicted by the thermoviscous propagation model for the $\Gamma = 10$ initial waveform, the predicted WSF values for the tube follow the Earnshaw solution fairly closely for distances much less than the shock formation distance. However, the WSF values predicted by the plane wave tube model follow the Earnshaw solution much longer than the WSF values predicted by the thermoviscous model given $\Gamma = 10$, shown in Figure 4.3. In fact, the WSF values predicted by the plane wave tube model do not differ much from the Earnshaw solution until about $\sigma = 1$, and then continue to much lower values than predicted by either the Khokhlov solution, which is based on the thermoviscous model. The lower values of the WSF indicate that, for the same Gol'dberg number, nonlinearity is more important for the plane-wave-tube-like propagation model than for the thermoviscous propagation model, likely due to the relatively lower absorption of the higher harmonics.

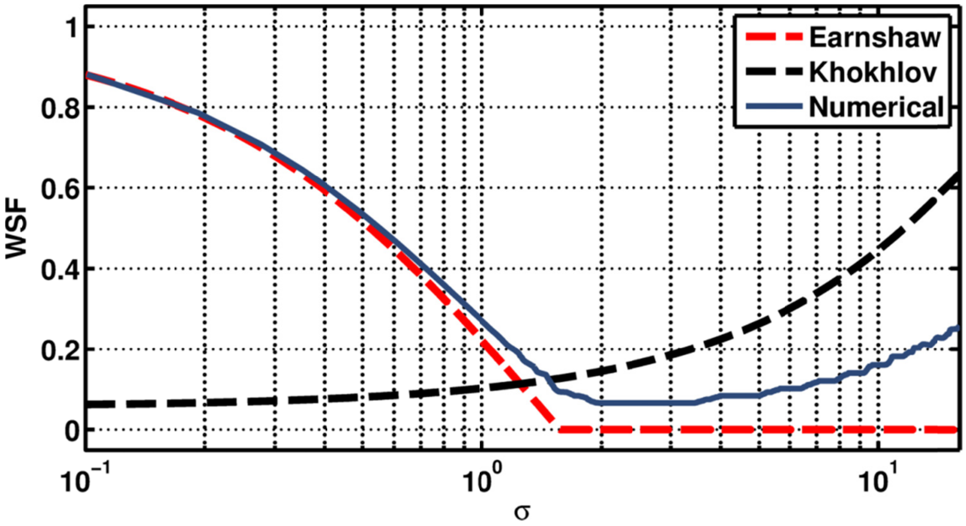

Figure 4.7. Estimates of the wave steepening factor (WSF) of waveforms predicted by numerically propagating an initially sinusoidal plane wave to various values of σ with linear losses similar to those of propagation in a plane wave tube.

The WSF values continue to decrease until about $\sigma = 2$, where they reach a minimum value of about 0.07. After the minimum value, the predicted WSF values begin to increase. The shape of the increasing trend is somewhat similar to the shape of the trend predicted by the Khokhlov solution, but the actual values are significantly lower. Thus, the plane wave tube model predicts that the waveform will behave somewhat similarly to the waveform predicted by the thermoviscous propagation model, but due to either lower high-frequency absorption or due dispersion nonlinearity appears to be more important for plane-wave-tube propagation than thermoviscous propagation, assuming similar values of Γ. Based on the findings of Blackstock, [10] the effects of boundary-layer dispersion are more likely to oppose nonlinear phenomena, so it is likely that the dominant effect is the lower high-frequency absorption.

The derivative skewness values predicted by the plane-wave-tube model show a similar trend as the trend of the predicted values of the WSF. The derivative skewness values predicted by the plane-wave-tube model are plotted as a function of the absorption distance in Figure 4.8, along with the derivative skewness values of the Earnshaw solution and the discretely-sampled Fay solution, for comparison. For values of $\sigma < 0.6$, the derivative skewness estimates follow the Earnshaw solution fairly closely. However, the derivative skewness values diverge from the trend predicted by the Earnshaw solution past the shock formation distance, and do not approach the derivative skewness of the Fay solution. Once again, at about $\sigma = 1.6$ the derivative skewness estimates appear to abruptly reach a maximum value, and is due to a sampling rate that is insufficient to adequately estimate the derivative skewness. The derivative skewness remains at the maximum value until about $\sigma = 9$. For $\sigma > 9$ the derivative skewness values predicted by the plane-wave-tube model begin to decrease again, somewhat similar to the trend suggested by the Fay solution. Thus, by $\sigma = 9$ the numerical model predicts that the waveform will begin to unsteepen.

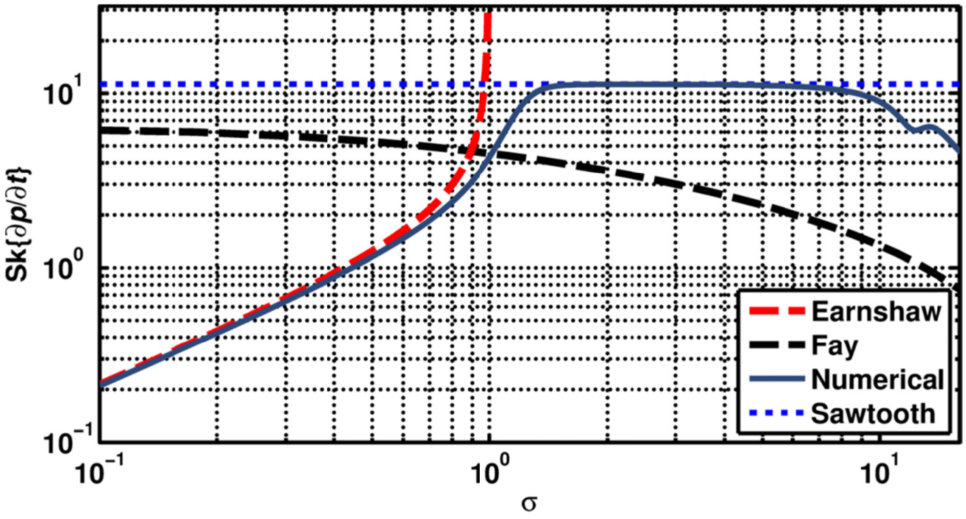

Figure 4.8. Estimates of the derivative skewness of waveforms predicted by numerically propagating an initially sinusoidal plane wave to various values of σ with linear losses similar to those of propagation in a plane wave tube. The dotted blue line represents the upper limit based on a discretely sampled sawtooth wave.

The largest difference between the trends of the predicted WSF and derivative skewness values for the plane wave tube case (given $\Gamma = 10$) occurs between $\sigma = 1.5$ and $\sigma = 9$. The predicted values of the WSF follow a plausible trend based on the lower high-frequency absorption coefficients associated with plane-wave-tube propagation, but the predicted values of the derivative skewness reach some upper limit (about 11), and stay there until about $\sigma = 9$, where the values decrease again. Based on the curved nature of the derivative skewness values predicted by the thermoviscous propagation model for the waveform with the Gol'dberg number equal to 10 in the transition from the Earnshaw to the Fay solutions, we would expect that the derivative skewness predicted by the plane-wave-tube model would also be rounded. As mentioned above, a likely reason is that the discretely sampled nature the numerical model will put an upper bound on the derivative skewness estimates.

4.3.3 Plane Wave Tube Propagation of an Initially Broadband Gaussian Noise Signal

The plane-wave-tube model used for the case of the initially sinusoidal wave may also be used to study the effects of nonlinearity on broadband noise. Since the numerical experiment is identical to the initially sinusoidal case except for the input waveform, any differences between the nonlinearity measures predicted in Section 4.3.2 and those predicted in this section will be due to the difference in the input signals. In order to compare the two, the nonlinear distortion distance defined and discussed in Section 2.2.2.4 will take the place of the shock formation distance used in the previous two sections.

The broadband noise used in this numerical experiment consists of bandpass-filtered spectrally white Gaussian noise. The pass-band was chosen to be between 700 Hz and 2300 Hz. This yields a geometric mean frequency of about 1269 Hz and an arithmetic mean frequency of 1500 Hz. If we assume that nonlinearity affects noise propagation over shorter distances than for a tonal wave, as suggested by Muhlestein, et al. [38] and in Gurbatov and Rudenko, [43] then the higher arithmetic mean frequency is more likely to be a reasonable characterization of the noise signal. The root-mean-square of the pressure amplitudes of the noise is about 1.17 kPa (about 155 dB re 20μPa). These conditions, along with the propagation conditions described in the previous sections, lead to $\Gamma = 1/\alpha\bar{x}_N = 10$.

Portions of the waveforms predicted by the plane-wave-tube model and the input noise described above are shown in Figure 4.9. Similar to the initially sinusoidal case, the pressure rises steepen, and the peaks become more rounded than the troughs due to dispersion. However, not all of the pressure rises become shocks, since the pressure rises vary in amplitude. The large pressure rises experience significant nonlinear distortion (as seen by the initially large pressure rise near $\theta = 1.6$), and the small pressure rises experience much less distortion (as seen by the slight pressure rise near $\theta = 0.3$). As the waveform propagates, the distribution of the pressure rises appears to become more uniform. This is due to the fact that shocks with higher amplitudes will experience more nonlinear attenuation than shocks with lower amplitudes. Thus, pressure outliers will be attenuated, and the pressure rise distribution becomes more uniform.

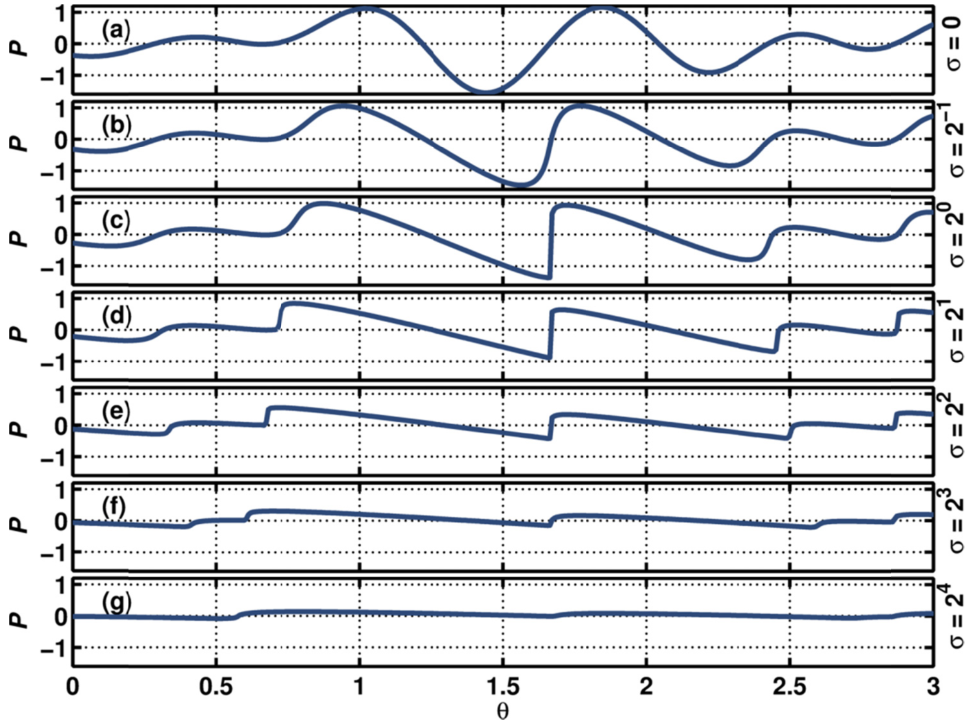

Figure 4.9. Portions of the waveforms predicted by numerically propagating an initially broadband Hz plane wave to various values of σ with linear losses similar to those of propagation in a plane wave tube.

The spectra of the predicted waveforms also provide information of the waveforms on the whole. Gurbatov *et al*. [17] found that broadband noise with well-developed shocks due to nonlinear propagation will have a spectrum that decays as f^{-2} at high frequencies, and grows as f^2 at low frequencies, assuming an initially Gaussian noise signal with a spectrum that goes as f^n, where $n \geq 2$, as $f \rightarrow 0$. (As mentioned in Chapter 1, in the pre-shock propagation regime, the higher frequencies decay as f^{-3}.) However, the theory used to find this spectral relationship assumed propagation with only thermoviscous absorption (where the pressure amplitude decays as $e^{-\alpha f^2 x}$) and no dispersion. This assumption suggests that broadband noise that develops shocks due to propagation in a tube that includes absorption of the form $e^{-\alpha\sqrt{f}x}$ and significant dispersion could have spectral characteristics that deviate significantly from spectral shape reported by Gurbatov and Rudenko.

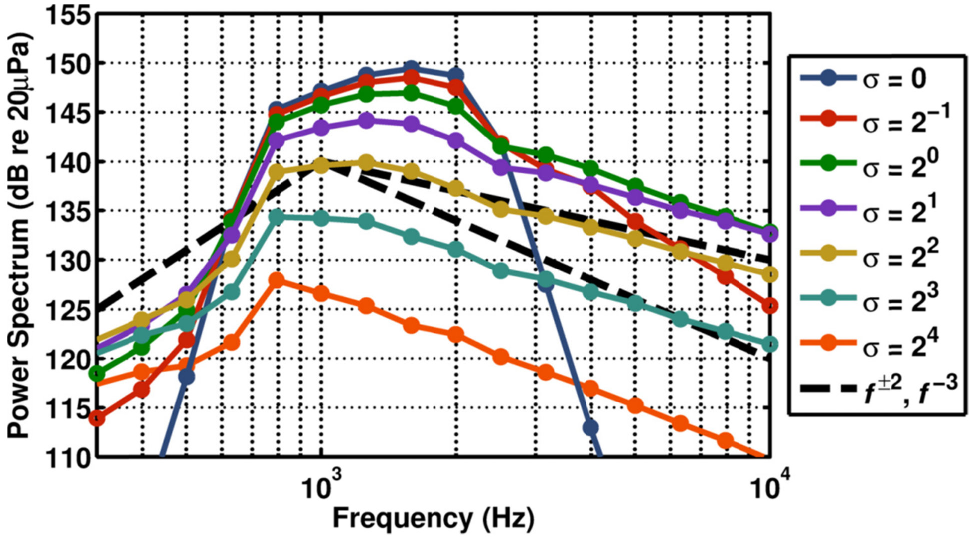

Figure 4.10. One-third octave power spectra predicted by numerically propagating an initially broadband Hz plane wave to various values of σ with linear losses similar to those of propagation in a plane wave tube.

The one-third octave power spectra of the waveforms predicted using the plane-wave-tube numerical model are presented in Figure 4.10, with dashed lines representing the $f^{\pm 2}$ and f^{-3} dependencies predicted by Gurbatov and Rudenko plotted for reference. The spectrum of the input waveform is quite band-limited, with the edges of the pass-band being noted by an amplitude drop of 10-20 dB. As the waveform propagates, the high and low frequencies begin to increase in amplitude, due to nonlinear transfer of energy from the pass-band to the extreme frequencies. At $\sigma = 2^{-1}$ the original pass-band maintains some of its shape, the high frequencies decay nearly as f^{-3}, indicating the pre-shock regime, and the low frequencies increase nearly as f^2. By $\sigma = 2$ the original pass-band region has lost much of its shape, and the extreme frequencies have reached an asymptotic rise and decay rate. Interestingly, the high-frequency asymptotic rates go as f^{-n} where $n < 2$, rather than the f^{-2} rate predicted by Gurbatov and Rudenko. This may be due to the fact that the absorption due to boundary-layer effects are less significant (relative to the absorption at the characteristic frequency) than the absorption due to thermoviscous effects. By $\sigma = 2^4$, the high frequencies have begun to decay faster than the high frequencies of spectra at lower values of σ, indicating that the waveform is leaving the sawtooth regime and is entering the old-age regime.

The WSF values of the noise waveforms predicted by the plane-wave-tube model show many similarities with the values of initially sinusoidal waveforms predicted by the same model. The predicted values of the WSF are plotted in Figure 4.11 as a function of the absorption distance, with the WSF values of the Earnshaw solution of the initially sinusoidal plane wave and the discretely sampled Khokhlov solution are plotted for comparison. For small values of σ, the predicted WSF values follow the trend predicted by the Earnshaw solution until about $\sigma = 0.3$, after which the predicted WSF values become larger than the Earnshaw solution suggests. After the departure, the predicted values of the WSF decrease until they reach a minimum near $\sigma = 4$, after which the values increase slightly. While the trend of the WSF values predicted by the noise case is similar to the initially sinusoidal case in character, there are significant differences in the details. For example, the noise case departs from the Earnshaw solution much earlier than the initially sinusoidal case. Also, the minimum WSF value of the noise case is about 0.13, compared to the minimum value of about 0.07 for the initially sinusoidal case. Since portions of the noise waveform shows significant nonlinear distortion, it appears that the less distorted regions of the waveforms significantly raise the WSF estimates.

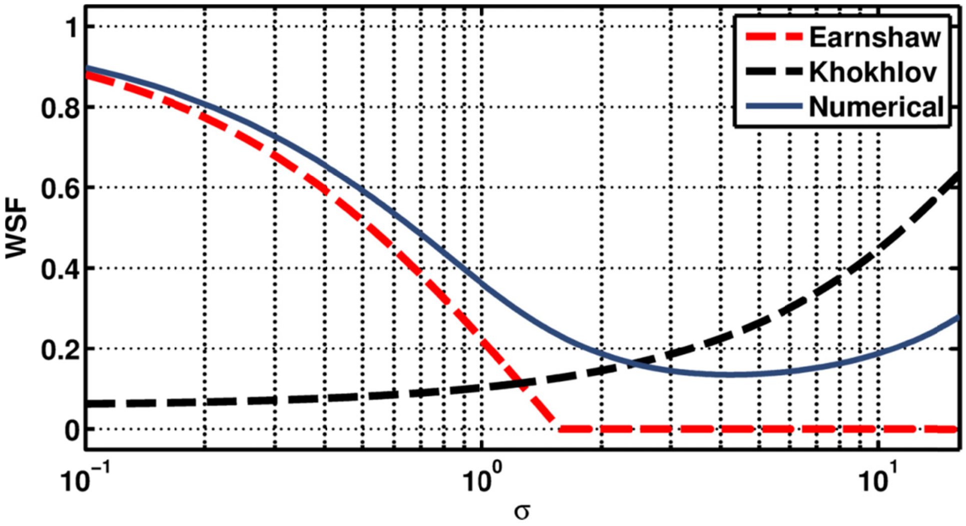

Figure 4.11. Estimates of the wave steepening factor (WSF) of waveforms predicted by numerically propagating an initially broadband plane wave to various values of σ with linear losses similar to those of propagation in a plane wave tube.

The derivative skewness values of the noise waveforms predicted by the plane-wave-tube model (shown in Figure 4.12) show a significantly different behavior than the trends predicted by either of the initially sinusoidal cases considered above. The derivative values of the noise waveforms deviate from the Earnshaw solution from $\sigma = 0$ (which is at the source), and become large very rapidly. The derivative skewness values reach a maximum value (about 27.3) well before $\sigma = 1$, and then decay slightly down to a stable value (about 13.8) until near the end of the sawtooth region. One possible reason for the dramatic rise in derivative skewness values is because the pressure outliers (such as the pressure rise near $\theta = 1.6$, shown in Figure 4.9) rapidly become shocks while most of the waveform takes longer, and then decay until they are no longer pressure outliers. The stable region is reminiscent of the region $1.5 < \sigma < 9$ in the plot of the derivative skewness estimates for the initially sinusoidal case in Figure 4.8. It is therefore likely that the stable region is due to a sampling rate that is too low to properly resolve the shocks. Since it is a noise waveform, rather than an initially sinusoidal signal, the low-amplitude pressure rises are more likely to be well resolved and the derivative skewness estimates may go above the limit for a discretely sampled sawtooth wave.

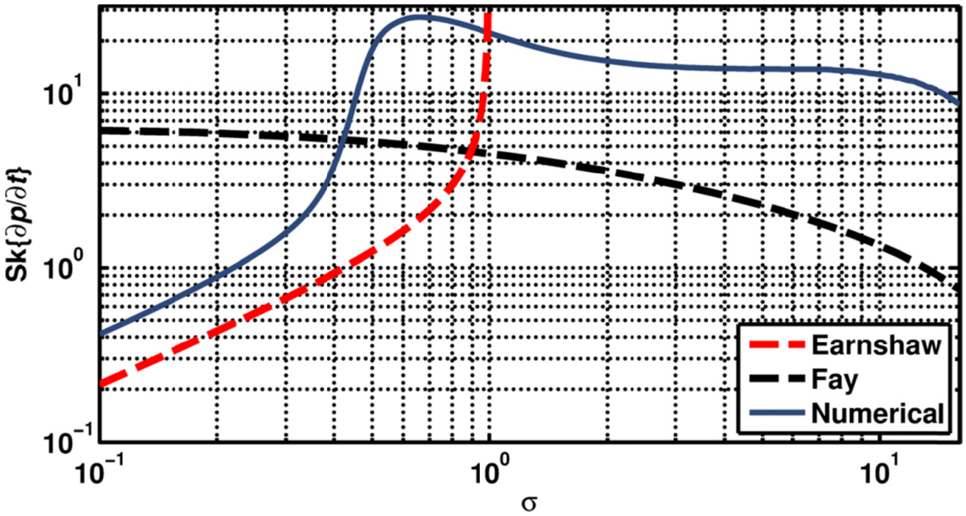

Figure 4.12. Estimates of the derivative skewness of waveforms predicted by numerically propagating an initially broadband plane wave to various values of σ with linear losses similar to those of propagation in a plane wave tube.

Notice that early in the pre-shock region of Figure 4.12 the trend of the derivative skewness estimates of the numerically propagated noise signal appears to be identical to the trend of the derivative skewness associated with the Earnshaw solution, but is slightly offset. The multiplicative factor that would shift the trend for the noise to the trend of the Earnshaw solution was suggested by Muhlestein and Gee [38] as a way to define a characteristic shock formation distance for noise signals.

4.4 Conclusions

A propagation model based on a generalized Burgers equation has been used to numerically analyze the propagation of initially sinusoidal and broadband Gaussian noise signals. Comparisons of the WSF and derivative skewness of initially sinusoidal signals that propagate with thermoviscous absorption compared favorably with analytical solutions, confirming the validity of the propagation model. This experiment was also useful in that it gave examples of what can be expected in measurements during the transition of the wave steepening factor (WSF) and derivative skewness values from the pre-shock propagation regime to the sawtooth propagation regime.

The thermoviscous numerical propagation results were compared with the numerical propagation of an initially sinusoidal signal with linear losses similar to that of a plane wave tube. It was found that, for a given Gol'dberg number, nonlinearity is more important for propagation with losses similar to propagation in a plane wave tube than for propagation with only thermoviscous absorption. It was also shown that the evolution of the two nonlinearity measures, WSF and derivative skewness, is similar in shape but not in details for both thermoviscous and plane-wave-tube like absorption.

Comparing initially sinusoidal wave propagation with initially broadband Gaussian noise propagation shows that both the WSF and the derivative skewness have generally higher values for noise signals than for initially sinusoidal signals. It was hypothesized that, for the sampling frequency and fundamental frequency used for these experiments, the derivative skewness was unable to be properly resolved for the sawtooth regime of propagation, for both initially sinusoidal and Gaussian noise signals. On the other hand, the derivative skewness estimates appeared to show greater sensitivity to the presence of shocks in initially noise waveforms than the WSF estimates.

It is interesting to note that the two nonlinearity measures suggest opposite conclusions about the nature of nonlinear noise distortion. The WSF predicts that noise waveforms will distort at a slower rate than an initially sinusoidal signal for a given Gol'dberg number, whereas the derivative skewness predicts that the noise waveforms distort much more rapidly than an initially sinusoidal signal for the same Gol'dberg number. This apparent contradiction is resolved by realizing that the WSF emphasizes the average slopes and the derivative skewness emphasizes the greatest slopes. Thus, the small numbers of significant shocks that form rapidly in a noise waveform do not affect the WSF values significantly, whereas the derivative skewness is dramatically affected.

Chapter 5

Applications of Nonlinearity Measures to One-Dimensional Measured Waveforms

5.1 Introduction

The main benefit of analyzing the noise measured in a plane wave tube is the small number of unknown parameters in the acoustic propagation. For example, in an air-filled plane wave tube there is no geometrical spreading, the linear absorptive and dispersive effects of propagation are calculable, and a well-understood source may be used. This means the effects of nonlinearity in the noise propagation can be extracted from the data relatively simply. In addition, the lack of geometrical spreading means that nonlinear effects are more likely to be important than if significant spreading occurred. These effects may be verified by comparing the wave steepening factor and skewness estimates of the measured waveforms with the analytically and numerically discussed results from Chapter 3 and Chapter 4. By using this understanding of the nonlinearity characteristics in one-dimensional noise propagation, it will be easier to understand the role of nonlinearity in the more complicated and important problem of jet noise.

5.2 Experimental Setup

A plane wave tube was constructed for the purpose of studying the evolution of measures of nonlinearity as plane waves propagate. The tube consists of several 3.05 m (10 ft) portions of PVC pipe with a radius of 2.54 cm (1 inch), connected by either rigid, plastic couplers or more flexible, rubber couplers. Both the plastic and rubber couplers have an inner rim that acts as a partition between the two lengths of pipe being coupled, but the partitions of the plastic couplers have a thickness much less than the thickness of the PVC pipe walls and the partitions of the rubber couplers have a thickness on the order of the thickness of the PVC pipe walls. The cutoff frequency of the first axial mode of the tube is 4.0 kHz. A plot of the total number of modes with cutoff frequencies below a given threshold is shown in Figure 5.1. The tube is terminated by an anechoic wedge inside a portion of PVC pipe. The absorption coefficients of the termination, shown in Figure 5.2, were obtained using band-limited (500-3500 Hz) white noise, and a two-microphone technique, valid for the frequency range of 450-3601 Hz. These coefficients suggest that the termination is anechoic for the full range of the input noise. The tube was driven by a single BMS coaxial compression driver (model 4590), mounted directly onto one end of the tube. The pressure data were measured using five G.R.A.S 40DD 3.18 mm (eighth-inch) microphones at various distances from the driver, inserted into the tube such that the microphone diaphragms were flush with the inside wall of the tube. No protection grids were used on the microphones so they would fit more closely into the tube walls, and to avoid resonances between the grid and the diaphragm. The microphones were located 0.3 m, 2.5 m, 5.6 m, 8.6 m, and 11.6 m from the driver. The compression driver was controlled with a National Instruments PXI-based system using 24-bit PXI-4461 card. The time-waveform data were acquired with the same PXI-based system used to drive the tube, using PXI-4462 cards. The system was controlled with a LabVIEW®-based software. The data were acquired at a rate of 204 800 samples/s (4.9 μs/sample). Post-processing of the data was performed using MATLAB®.

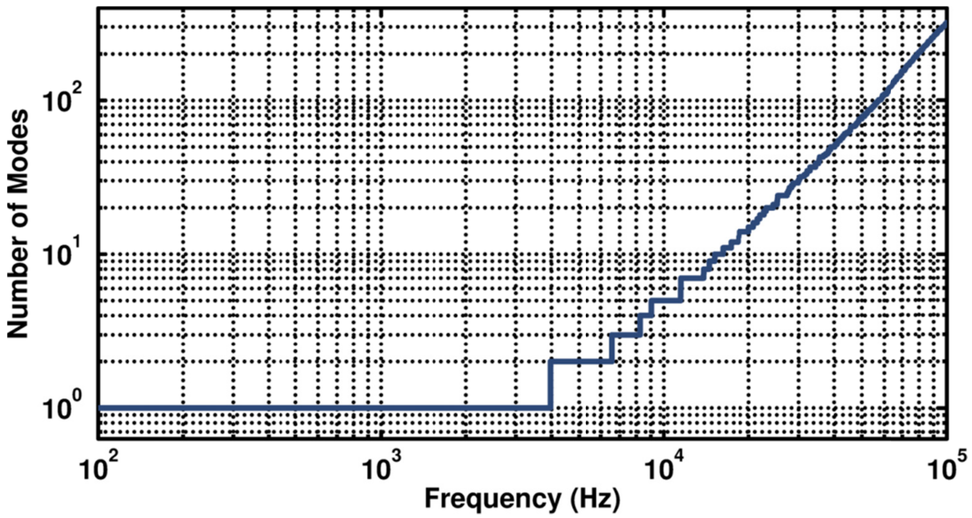

Figure 5.1. Total number of modes in the plane wave tube with cutoff frequencies less than the frequency of interest.

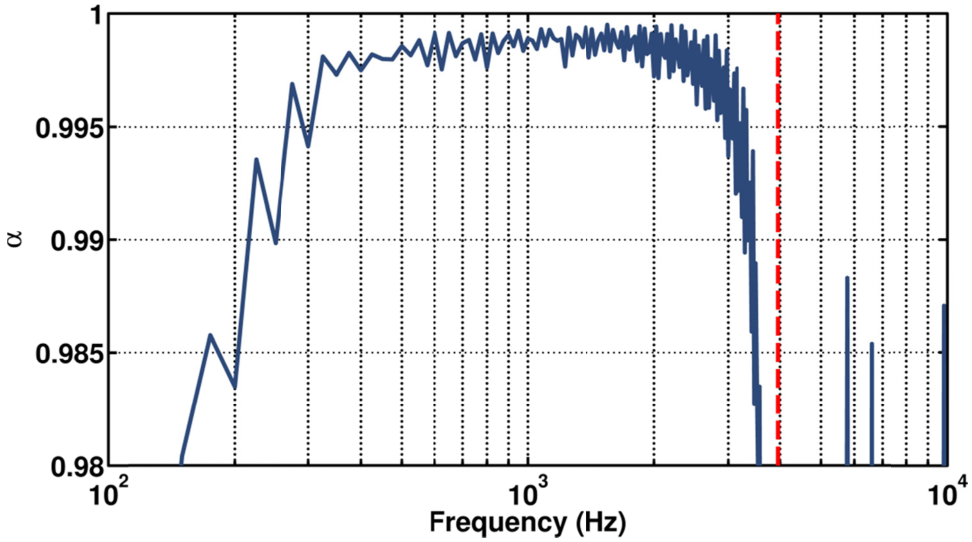

Figure 5.2. Absorption coefficients of the plane wave tube termination. The signal used to estimate the absorption coefficients was band-limited (500-3500 Hz) white noise. The dashed red line represents the cutoff frequency of the first axial mode of the tube.

Several experiments were conducted in the plane wave tube described above. The tube was driven with sine waves, narrowband Gaussian noise, broadband Gaussian noise, narrowband noise with jet noise-like statistics, and broadband noise with jet noise-like statistics. A description of the statistics associated with jet noise is presented in Ref. [35]. The most important aspect of jet noise for the purposes of this thesis is the skewness of the pressure waveform is noticeably greater than zero, as high as 0.6 for an F/A-18E at afterburner engine condition. This can be seen in Figure 5.3, where a Gaussian and jet noise-like probability density functions (PDFs) are plotted. The skewness of the jet noise-like probability density function shown in Figure 5.3 is 0.56. It should be noted that only the pressure statistics were jet noise like; the time-derivative statistics were not accounted for. [25]

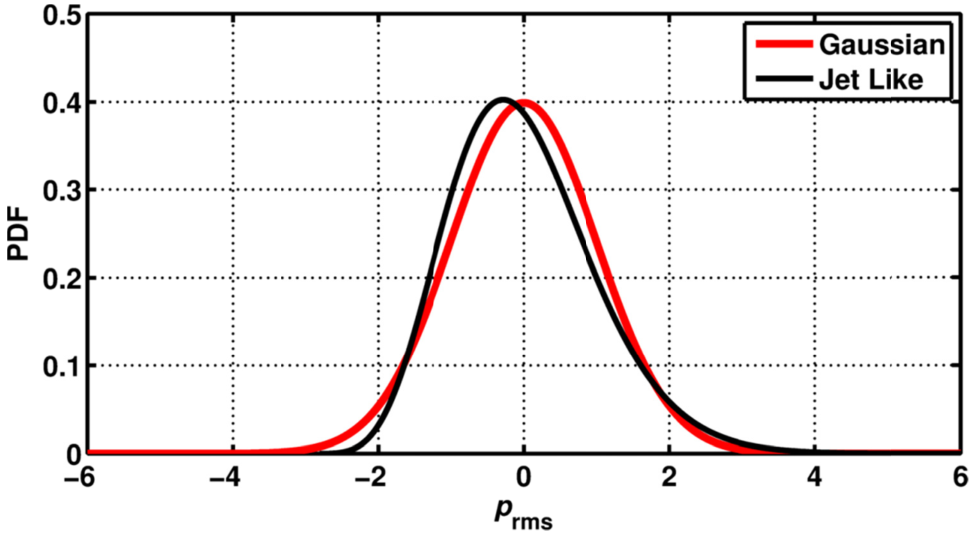

Figure 5.3. Probability density functions of Gaussian and jet like noise.

The bandwidths of the noise signals were arbitrarily chosen to be about one-fifteenth of the characteristic frequency for narrowband noise and is approximately equal to the characteristic frequency for broadband noise. The noise was obtained by filtering spectrally white noise with the proper time-domain statistics with a bandpass filter. For all noise types, the characteristic frequency f_c is considered to be the arithmetic mean of the frequency bounds of the pass-band. For each of the above cases, waveforms with a given characteristic frequency were generated for various amplitudes. The variation of the amplitude varies the nonlinear distortion length of the noise (see Equation (2.27)), and therefore changes the value of σ for a different waveforms at a single microphone location.

Recall from Chapter 2 that we may define a nondimensional distance $\sigma = x/\bar{x}$, where $\bar{x}$ is the shock formation distance for initially sinusoidal signals (Equation (2.3)), or $\sigma = x/\bar{x}_N$ where $\bar{x}_N$ is the characteristic nonlinear distortion length for noise (Equation (2.27)). Throughout this and other chapters, if noise is being considered then the characteristic nonlinear distortion length defined in Equation (2.27) is the assumed normalization of σ, and if an initially sinusoidal signal is being considered the shock formation distance defined in Equation (2.3) is the assumed normalization.

5.3 Waveforms

Examining the waveforms of a given test at multiple distances from the driver can let one directly observe the nonlinear distortion. As a wave propagates, pressure rises will begin to steepen and eventually form shocks, given an initial amplitude such that nonlinear effects will dominate absorptive effects. The waveforms shown in Figure 5.4 and Figure 5.5 have been chosen because they clearly exhibit this nonlinear distortion. Waveforms with lower initial amplitudes do not experience nonlinear distortion as significantly over a given distance. This is due to the decreased relative importance of nonlinearity associated with longer nonlinear distortion lengths at low amplitudes. While waveforms with initial amplitudes higher than those presented here exhibit more nonlinear distortion, they are more difficult to clearly measure due to source distortion, which will be discussed further below.

The waveforms in Figure 5.4 are time-aligned portions of an initially sinusoidal wave with a frequency of 1500 Hz. The amplitude of the wave at 0.3 m from the driver was 515 Pa. Assuming the wave was truly sinusoidal at the 0.3 m measurement location (which, due to propagation and source nonlinearities, is not necessarily a good assumption), then the shock formation distance of this wave is 8.4 m. Since propagation in a tube includes linear losses such as atmospheric and boundary layer absorption and dispersion, the waveforms are expected to have no true discontinuities at 8.6 m or 11.6 m. This expectation is verified by the purple and yellow lines in Figure 5.4. Since the propagation is approximately planar, the decaying amplitude of the waveforms as the measurement distance increases is evidence of the importance of the atmospheric and boundary layer losses mentioned above. The effects of dispersion are also evident, especially in the 11.6 m waveform (represented by the yellow line in Figure 5.4). As shown by Webster and Blackstock, [6] the peaks of shocks that propagate in tubes become more rounded, while the low-pressure portions of the shocks are less rounded. This asymmetry is evident in the waveform measured at 11.6 m. Another feature of the waveform measured at 11.6 m is an oscillation of the waveform near shocks. This oscillation is unexpected, and may be due to physical inhomogeneities in the plane wave tube, such as the impedance change from the PVC tube to the diaphragm of a microphone or a coupler, despite efforts to make the transitions smooth. The fact that the wavelength of these oscillations is about the diameter of a microphone diaphragm supports the idea that these oscillations are due to inhomogeneities in the plane wave tube. Since the nonlinear distortion generates higher harmonics of the initial frequency, and most of the harmonics have frequencies greater than the cutoff frequency of the first axial mode of the tube, this type of inhomogeneity may move energy from the plane-wave mode to cross modes.

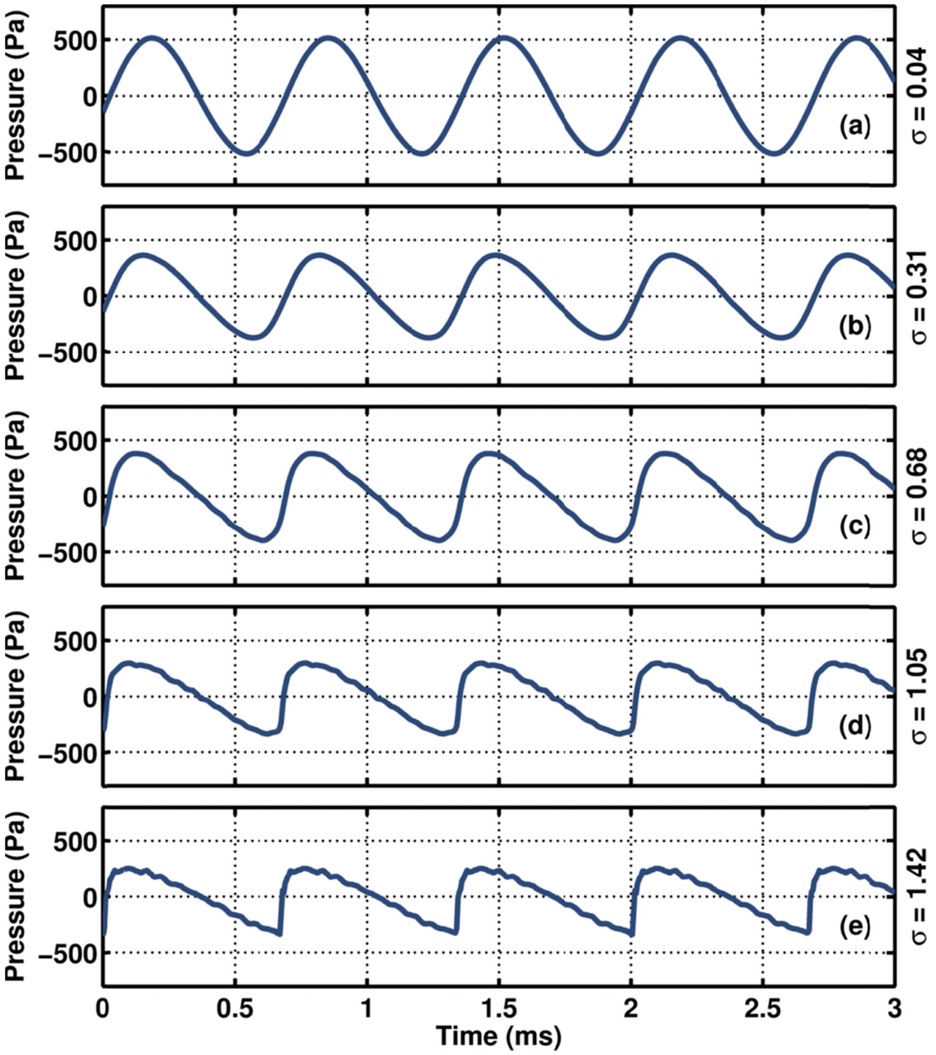

Figure 5.4. Waveforms measured at locations (a) 0.3 m, (b) 2.5 m, (c) 5.6 m, (d) 8.6 m, and (e) 11.6 m from a driver in an anechoically terminated plane wave tube. The input waveform was a 1500 Hz sine wave, and the amplitude at the 0.3 m microphone was 515 Pa. The sine wave at the 0.3 m microphone has a shock formation distance 8.3 m, and the values of σ are stated on the right of the plots.

The waveforms plotted in Figure 5.5 are time-aligned portions of the waveforms measured of initially broadband Gaussian noise. The characteristic (arithmetic mean) frequency of the noise is 1500 Hz (the geometric mean is about 1270 Hz) and the root-mean-square pressure amplitude of the noise measured at the 0.3 m microphone is 375 Pa. This wave has a characteristic nonlinear distortion length of 8.0 m, based on the measurement at the 0.3 m microphone. Just as was seen in Figure 5.4, the overall amplitude of the wave can be seen to decrease for increasing distance in the tube, indicating the importance of linear losses in the noise propagation. The same kind of unexpected oscillations near the shocks seen in Figure 5.4 are also present in several of the waveforms in Figure 5.5. Unlike the initially sinusoidal case, broadband noise does not generate shocks uniformly throughout the waveform. Notice that near 1.2 ms and 2.4 ms, significant shocks have formed in the waveform measured at 11.6 m from the source (represented by the yellow line in Figure 5.5), that shocks are forming at 0.4 ms and 3.2 ms of the same waveform, and that the pressure rise near 4 ms of the same waveform has not even steepened significantly. This variation in the waveform distortion is explained by the fact that nonlinear effects are dependent upon the local amplitude of a waveform. Since the amplitude of noise varies over time, so do the effects of nonlinear distortion, as discussed in Chapter 1. This variation in the effects of nonlinear distortion is the reason why the shock formation distance – the distance at which the first shock in a waveform propagating without losses will appear – of noise depends significantly upon the specifics of the waveform.

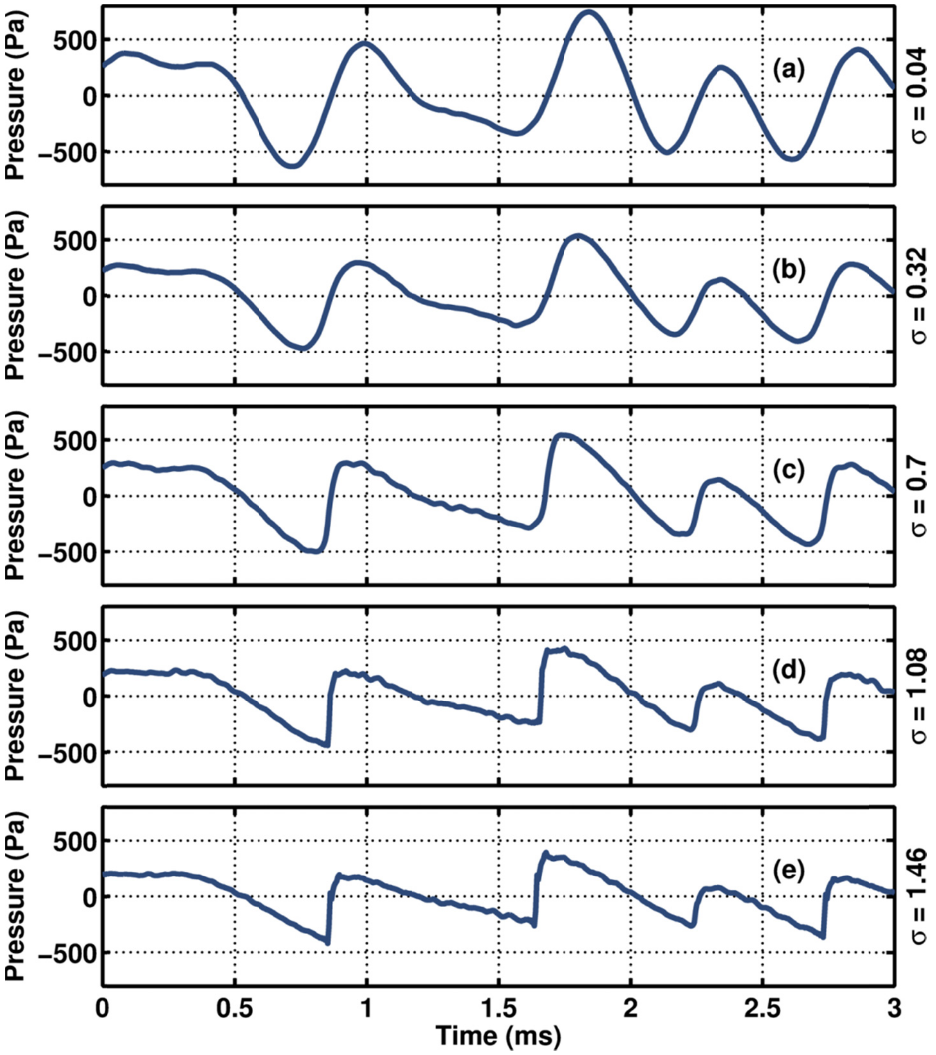

Figure 5.5. Waveforms measured at locations (a) 0.3 m, (b) 2.5 m, (c) 5.6 m, (d) 8.6 m, and (e) 11.6 m from a driver in an anechoically terminated plane wave tube. The input waveform was broadband Gaussian noise with a characteristic (arithmetic mean) frequency of 1500 Hz, and root-mean-square amplitude of 375 Pa at the 0.3 m microphone. The nonlinear distortion length of the noise at the 0.3 m microphone is 8.0 m, and the values of σ are stated on the right.

5.4 Spectra

The nonlinear distortion of the waveforms is also manifest in the frequency domain, as discussed in Section 1.2. This section will focus on demonstrating the importance of nonlinearity in the propagation of high-amplitude signals, both initially sinusoidal and broadband noise, in a plane wave tube. The initially sinusoidal signals will be compared with the

Blackstock bridging function, and the spectral slopes of the broadband signals will be compared to the Gurbatov and Rudenko asymptotes. [43]

5.4.1 Initially Sinusoidal Waves

The harmonic amplitudes of the periodic waveforms shown in Figure 5.4 are shown in Figure 5.6, along with the amplitudes predicted by the Blackstock bridging function, assuming that the amplitude of the waveform measured 0.3 m from the source is the source amplitude. The fundamental frequency dominates the signal for all five measurement locations, but most especially for the measurement 0.3 m from the source. As the distance from the source increases, the strength of the higher harmonics increases, as expected. Since all of the harmonics are integer multiples of the fundamental frequency – 1500 Hz in this case – all sum and difference frequencies will also be either the fundamental frequency or a higher harmonic.

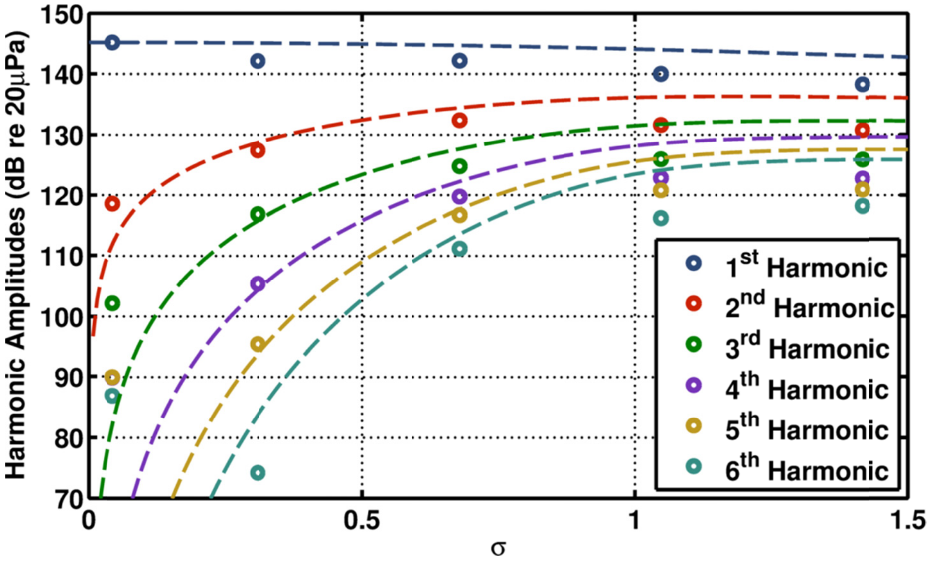

Figure 5.6. Harmonic amplitudes of an initially sinusoidal signal with a characteristic frequency of 1500 Hz. The circles represent the harmonic amplitudes of the signal measured in a plane wave tube 0.3 m, 2.5 m, 5.6 m, 8.6 m, and 11.6 m from the driver. The dashed lines are the amplitudes predicted by the Blackstock bridging function. The shock formation distance of the waveform measured at the 0.3 m microphone is 8.3 m.

Comparing the harmonic amplitudes predicted by the Blackstock bridging function with the measured amplitudes can give insight into the physical phenomena of the propagation. Since the bridging function assumes no linear absorption, we expect the measured amplitudes will be lower than the predicted amplitudes. However, the harmonic amplitudes of the waveform measured 0.3 m from the source and the 3rd through 5th harmonics of the waveform measured 2.5 m from the source are greater than the predicted amplitudes. The most likely cause of this discrepancy is source distortion rather than propagation distortion. The fact that the harmonic amplitudes measured farther from the source (8.6 m and 11.6 m) are all significantly less than the predicted levels further suggests source distortion is the cause of the large harmonic amplitudes of the waveform measured 0.3 m from the source.

The comparison of harmonics with the Blackstock bridging function is easily extended to comparing large numbers of waveforms simultaneously. In Figure 5.7, the amplitudes of harmonics 2 through 6 of several waveforms, all initially sinusoidal plane waves with a fundamental frequency of 1500 Hz but with different initial amplitudes, are plotted as a function of σ. These harmonics are all normalized by the amplitude of the first harmonic measured 0.3 m from the source. In addition, the amplitudes of each harmonic predicted by the Blackstock bridging function are plotted as a function of σ, for comparison.

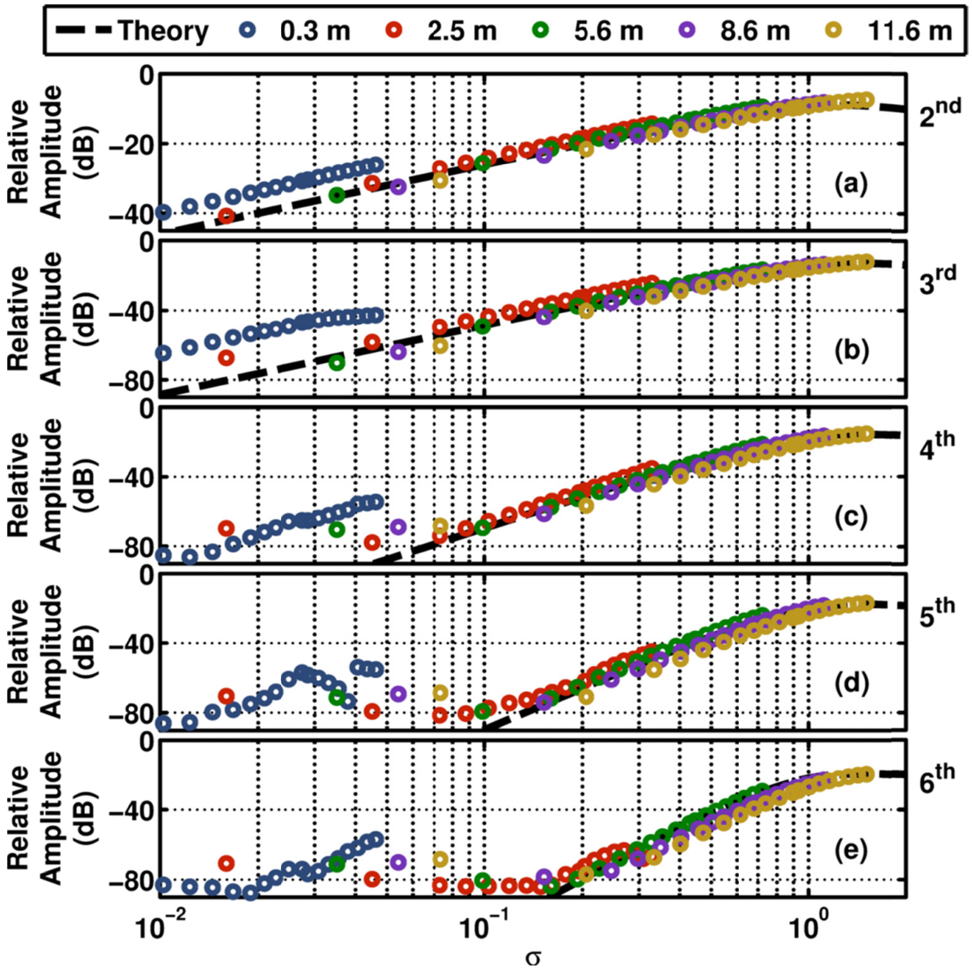

Figure 5.7. Amplitudes of harmonics 2 through 6 ((a) through (e), respectively) relative to the source amplitude of several initially sinusoidal plane waves with a fundamental frequency of 1500 Hz measured at various distances from a source in a plane wave tube. The harmonic amplitudes are normalized by the amplitude of the amplitude of the fundamental frequency measured 0.3 m from the source, and are plotted as a function of σ. The theoretical normalized harmonic amplitudes predicted by the Blackstock bridging function are also plotted (dashed black lines, labeled Theory in the legend), for comparison.

While the normalized amplitudes plotted in Figure 5.7 follow the trends predicted by the Blackstock bridging function, they do not lie perfectly on top of each other. This is most likely due to two important points. First, the propagation in the pipe is not lossless, while the Blackstock bridging function is based on the assumption of no linear losses. Second, the compression driver used was not able to produce a perfect sinusoidal signal at the amplitudes associated with the experiment. This source distortion is most likely the reason why the normalized second and third harmonics are greater than the bridging function predicts for the 0.3

m and 2.5 m measurements. On the other hand, the bridging function does predict the general trend of the amplitudes fairly well. This indicates the importance of nonlinear propagation effects in the data here.

The normalized amplitudes of the harmonics of initially sinusoidal plane waves with a fundamental frequency of 1000 Hz or 2000 Hz measured in the plane wave tube (not shown here) show many of the same trends shown in Figure 5.7. The amplitudes follow a similar trend as the Blackstock bridging function, but show deviations likely due to the linear losses associated with propagation in a tube and to source distortion. To further support the hypothesis that linear losses are a significant factor in the deviation of these trends from the bridging function, the amplitudes of 1000 Hz signals which has a lower absorption coefficient than the 1500 Hz signals, align much more closely to the bridging function, and the amplitudes of the 2000 Hz signals – which has a higher absorption coefficient than the 1500 Hz signals – deviate more significantly than the amplitudes of the 1500 Hz signals.

5.4.2 Broadband Noise

The spectra of the noise waveforms shown in Figure 5.5 are shown in Figure 5.8. Since the input noise was generated by filtering spectrally white noise with a bandpass filter, the top of the spectrum near the source (at the 0.3 m measurement location) is nominally flat, and beyond the bandpass region the spectrum decays at least 20 dB. The energy at the high and low frequency limits of the spectra comes from the pass-band region of the spectra, which is noticeably losing energy. By 8.6 m from the driver, the sharp drop in energy at the upper frequency edge of the bandpass region has disappeared, and the lower frequency edge of the pass-band region is becoming less pronounced. There is some energy near 4000 Hz in all of the spectra. This is likely due to a resonance of the first cross mode of the pipe, since the cutoff frequency of this mode is 4000 Hz. There is also a significant amount of energy around 10.5

kHz. Since a significant number of axial modes have a cutoff frequency within this range, (see Figure 5.1), this distortion is may be due to axial modes.

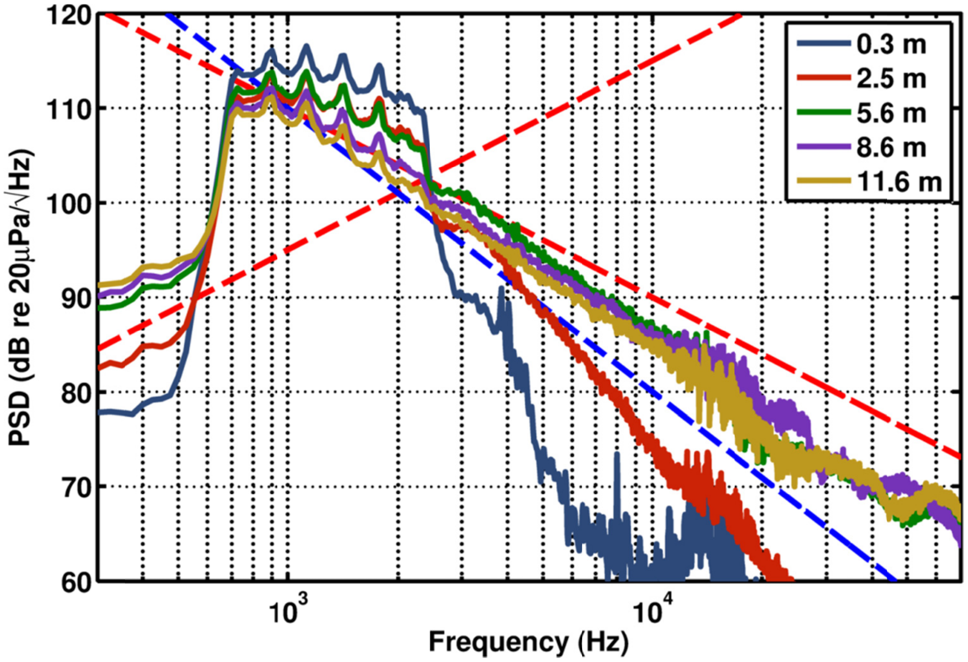

Figure 5.8. Power spectral density (spectrum) of an initially Gaussian broadband signal with a characteristic frequency of 1500 Hz, measured in a plane wave tube 0.3 m, 2.5 m, 5.6 m, 8.6 m, and 11.6 m from the driver. The dashed lines show a $f^{\pm 2}$ dependence (red dashed lines) and a f^{-3} dependence (blue dashed line), for comparison.

As close as 5.6 m from the driver the growth and decay of energy at low frequencies and high frequencies, respectively, have approached what appears to be asymptotic rates, but the high-frequency rates are somewhat different from those described by Gurbatov and Rudenko.[43] In the low-frequency limit the spectral slope goes as nearly f^2 for the spectra of all measurements past the 0.3 m location. The levels of this low-frequency region increase as the wave propagates down the tube indicates the nonlinear processes in the propagation are transferring energy from higher frequency regions to the low-frequency region. This transfer also seems to slow significantly as the wave propagates; the level increase at 400 Hz between the 2.5 m and 5.6 m measurement locations is 6 dB, but the level increase from the 5.6 m and 8.6 m measurement locations is 1 dB, and the level increase from the 8.6 m and 11.6 m measurement locations is only 0.9 dB.

5.5 Wave Steepening Factor

As discussed in Chapter 3, the wave steepening factor (WSF) is one way to characterize the nonlinear distortion in a waveform. In general, large values of the WSF of a waveform indicate the effects of nonlinear propagation are insignificant in the waveform, while small values of the WSF indicate the effects of nonlinear propagation are significant. The WSF for the Fubini and Khokhlov solutions were discussed in Chapter 3, both in the context of continuous sampling and for finite sampling rates. However, the Fubini solution did not include any linear losses and the Khokhlov solution only included thermoviscous losses in addition to nonlinear losses. The propagation of sound in a tube involves both absorptive and dispersive effects due to molecular relaxation and boundary layers, in addition to thermoviscous losses. Also, the source used for the plane wave tube experiments examined in this section likely produced signals with some distortion prior to propagation, as discussed in Section 5.3. With the exception of the source distortion, all of these effects were included in the numerical experiment described in Section 4.3.2.

The estimates of the WSF for a subset of the experiments performed in the plane wave tube, described above, are shown in Figure 5.9 and Figure 5.10 as a function of σ. In Figure 5.9 all of the waveforms used to estimate the WSF values were initially sinusoidal with a frequency of 1000 Hz, 1500 Hz, or 2000 Hz. In addition to the WSF values estimated from measured waveforms, the WSF values estimated from numerically propagated waveforms are also shown. The numerical data simulates the experimental setup: an initially sinusoidal signal is propagated a certain distance given a range of amplitudes. The variation in amplitude allows the WSF values for a range of σ values to be estimated. The numerical predictions for 5.6 m, 8.6 m, and

11.6 m (green, purple, and yellow dashed lines, respectively) are shown in Figure 5.9, for comparison. In Figure 5.10 the WSF estimates for initially narrowband Gaussian noise, initially broadband Gaussian noise, and initially broadband noise with jet noise-like statistics are shown. All of these noise signals have a characteristic (arithmetic mean) frequency of 1500 Hz. In addition, the numerically predicted WSF values for an initially sinusoidal signal with a frequency of 1500 Hz, propagated to a distance of 11.6 m from the source.

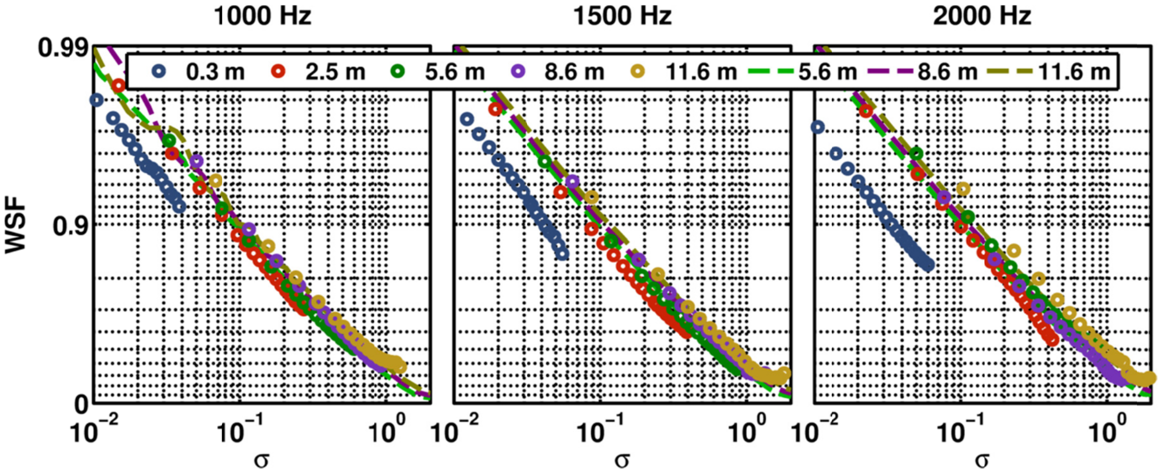

Figure 5.9. Estimates of the WSF of waveforms measured at various distances from the source in a plane wave tube experiment. The initial waveforms were sinusoidal with a frequency of either 1000 Hz, 1500 Hz, or 2000 Hz. By measuring waveforms of varying amplitude, a range of σ values were obtained for each of the distances. The dashed lines are predicted values using a numerical scheme to propagate an initially sinusoidal signal the stated distance.

The WSF estimates of the initially sinusoidal signals with different frequencies are quite similar. In all three plots in Figure 5.9 the WSF estimates from the 0.3 m microphone are significantly lower than the other estimates (likely due to source distortion), and the estimates from all of the other locations seem to follow the trend predicted by the numerical experiments. This uniformity suggests the WSF is not very sensitive to variations in propagation distance or characteristic frequency for initially planar sine waves propagating in a plane wave tube. Near $\sigma = 1.2$ the WSF estimates of the waveforms measured at 8.6 m and 11.6 m from the source become significantly larger than the numerical experiments predict. In particular, the lowest

WSF estimate for the 1500 Hz case is 0.27, whereas the numerical experiments predict a value of about 0.2 at the same location. Since the numerical experiments used the same sampling frequency as the physical experiments, and the minimum WSF value allowed by a discretely sampled sawtooth wave is less than 10^{-2}, this deviation is not likely to be due to insufficient temporal resolution. Comparison with the waveforms in Figure 5.4 suggests, however, the deviation is more likely due to unexpected jitter in the waveform. If this is the case, the WSF seems to be noticeably sensitive to small-scale jitter in a waveform. For example, trend of the WSF estimates based on the 11.6 m, initially 1500 Hz sinusoidal waveforms shown in Figure 5.9 actually begins to increase for $\sigma > 1.2$, whereas the numerically obtained values continue to decrease.

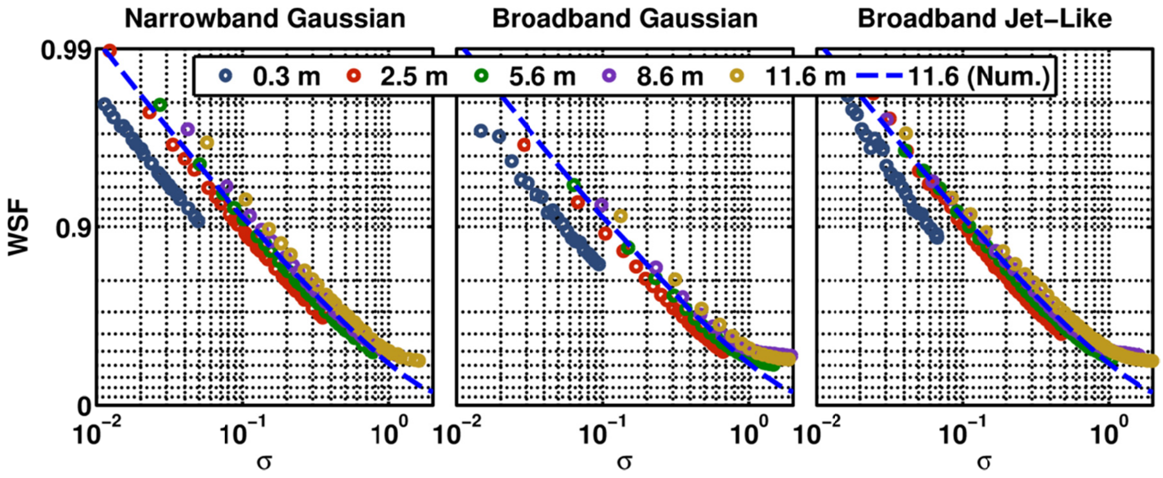

Figure 5.10. Estimates of the WSF of waveforms measured at various distances from the source in a plane wave tube experiment. The initial waveforms were either narrowband Gaussian noise, broadband Gaussian noise, or broadband noise with jet noise-like statistics. All waveforms considered have a characteristic (arithmetic mean) frequency of 1500 Hz. By measuring waveforms of varying amplitude, a range of σ values were obtained for each of the distances. The dashed lines are predicted values using a numerical scheme to propagate an initially sinusoidal signal to 11.6 m from the source.

The estimates of the WSF of the noise waveforms shown in Figure 5.10 are very similar to those of the initially sinusoidal waveforms shown in Figure 5.9. Again, the WSF estimates at the 0.3 m microphone are significantly lower than the other estimates for the same range of σ. The remaining estimates of the WSF all follow the numerically predicted values quite closely until about $\sigma = 1$. Since waveforms at $\sigma > 1$ are prone to unexpected jitter, it is again likely that this jitter caused the WSF estimates to be larger than they would be without the jitter. The similarity between the WSF estimates of the measured waveforms is somewhat unexpected, since the measured waveforms are noise signals while the numerically predicted waveforms are initially sinusoidal. The agreement of the numerically predicted WSF values and the experimentally obtained WSF values suggests the WSF is insensitive to source conditions, such as characteristic frequency, bandwidth, or statistics.

5.6 Derivative Skewness Estimates

As described in Chapter 3, the skewness of the first time-derivatives of the pressure amplitudes (derivative skewness) has been used to characterize jet noise fields. The derivative skewness has been associated with nonlinear propagation and shock content in a waveform. In particular, as a waveform steepens, the derivative skewness generally increases. As was shown in Section 3.2.2.2, given a continuous sampling of a waveform propagating without linear losses (such as the Fubini solution), the derivative skewness can diverge when shocks are present. However, the presence of linear losses or a finite sampling rate can cause the estimation of the derivative skewness to remain finite for all distances from a source.

The estimates of the derivative skewness for a subset of the experiments performed in the plane wave tube, described above, are shown in Figure 5.11 and Figure 5.12 as a function of σ. In Figure 5.11 all of the waveforms used to estimate the derivative skewness values were initially sinusoidal with a frequency of 1000 Hz, 1500 Hz, or 2000 Hz. In addition to the derivative skewness values estimated from measured waveforms, the derivative skewness values estimated from numerically propagated waveforms are also shown. The numerical data was obtained in the same manner as described in 5.5. The numerical predictions for 5.6 m, 8.6 m, and 11.6 m (green, purple, and yellow dashed lines, respectively) are shown in Figure 5.11, for comparison.

In Figure 5.12 the derivative skewness estimates for initially narrowband Gaussian noise, initially broadband Gaussian noise, and initially broadband noise with jet noise-like statistics are shown. All of these noise signals have a characteristic (arithmetic mean) frequency of 1500 Hz. In addition, the numerically predicted derivative skewness values for an initially sinusoidal signal with a frequency of 1500 Hz, propagated to a distance of 11.6 m from the source.

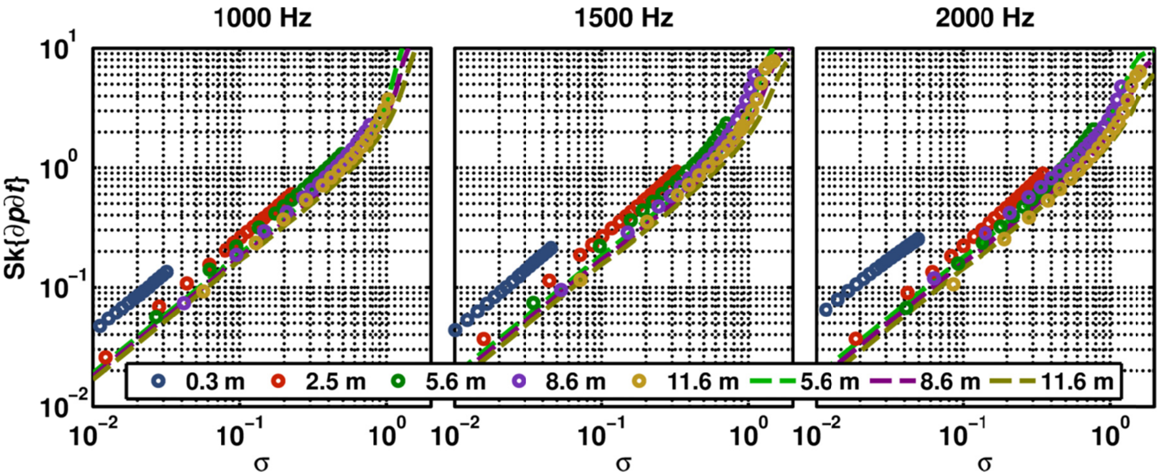
1000 Hz
1500 Hz
2000 Hz

Figure 5.11. Estimates of the derivative skewness of waveforms measured at various distances from the source in a plane wave tube experiment. The initial waveforms were sinusoidal with a frequency of either 1000 Hz, 1500 Hz, or 2000 Hz. By measuring waveforms of varying amplitude, a range of σ values were obtained for each of the distances. The dashed lines are predicted values using a numerical scheme to propagate an initially sinusoidal signal the stated distance.

Similar to the WSF values discussed above, the derivative skewness values of the measured waveforms of initially sinusoidal signals follow the numerically predicted derivative skewness values quite well, with the notable exception of the 0.3 m microphone data. Both the numerical and measured data suggest the derivative skewness values start near zero for σ near zero, and then increase. Near $\sigma = 1$ the derivative skewness values increase significantly. For the 1500 Hz and the 2000 Hz cases, the derivative skewness estimates for the 11.6 m microphone appear to somewhat level out. Since the value the estimates seem to be approaching is near 10, it is likely that they are reaching the sawtooth limit derived in Chapter 3, which for a value of

$\nu = 130$ (which would be the 1500 Hz case) is about 11.3. Thus, it is likely that this leveling off effect is due to insufficient temporal resolution of shocks.

It is notable the derivative skewness estimates of the measured waveforms do not depart significantly from the numerically predicted values. Recall the measured waveforms for large values of σ at the 8.6 m and 11.6 m microphone locations contained significant unexpected jitter. Despite the presence of jitter, the derivative skewness values do not appear to be significantly affected. This is likely due to the skewness is the mean of the cubes of the probability density function, which emphasizing outliers and suppressing small features; thus, a single large shock is much more important in the estimation of the derivative skewness than a very large number of small amplitude oscillations in a waveform.

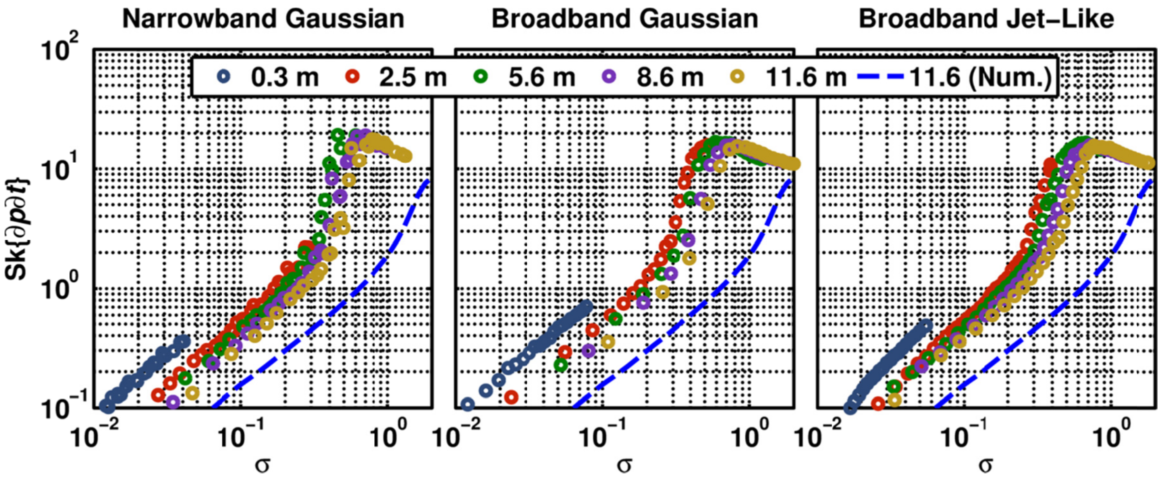

Figure 5.12. Estimates of the derivative skewness of waveforms measured at various distances from the source in a plane wave tube experiment. The initial waveforms were either narrowband Gaussian noise, broadband Gaussian noise, or broadband noise with jet noise-like statistics. All waveforms considered have a characteristic (arithmetic mean) frequency of 1500 Hz. By measuring waveforms of varying amplitude, a range of σ values were obtained for each of the distances. The dashed lines are predicted values using a numerical scheme to propagate an initially sinusoidal signal to 11.6 m from the source.

The derivative skewness estimates from the measured noise signals show similar trends as the initially sinusoidal cases, but also some significant differences. All of the derivative skewness estimates of the noise cases, shown in Figure 5.12, start near zero for very small σ, and increase at a rate similar to that predicted by the numerical experiments, and then at some point the derivative skewness values rise dramatically. However, the derivative skewness estimates of the measured noise signals appear to be offset from the numerically predicted values, and rise more steeply. Since the numerical experiment used here was an initially sinusoidal 1500 Hz signal, it is not necessarily expected the measured values would align with the numerical values. However, if it is desired the two should align, it is likely that the definition of σ for noise ($\sigma = x/\bar{x}_N$, where $\bar{x}_N$ is the nonlinear distortion length defined in Equation (2.27)) is a poor choice.

Another significant difference between the derivative skewness trends for the initially sinusoidal cases and the noise cases is the values at the top of the dramatic rise (near $\sigma = 1$ for initially sinusoidal signals and near $\sigma = 0.6$ for noise signals) level off for the initially sinusoidal cases, but first overshoot, and then decay again for the noise signals. As discussed in Chapter 4, this is likely due to the fact that nonlinearity emphasizes pressure outliers. The high pressures quickly become shocks, and then are attenuated until they are no longer outliers. [43] In this manner, the derivative skewness is especially sensitive to the presence of a small number of shocks in a waveform. Another explanation for the decay of the derivative skewness values after the initial rise is that, as the shock content in the waveform becomes more uniform, the effects of finite sampling frequencies will become more apparent, and the estimated derivative skewness will come closer to the limit found for a sawtooth wave.

5.7 Conclusions

High-amplitude propagation of sound in a plane wave tube, both initially sinusoidal and noise signals, has been shown to exhibit significant evidence of nonlinear propagation distortion in both the time and frequency domains. This nonlinear distortion has been studied in terms of the wave steepening factor (WSF) and the derivative skewness.

The WSF estimates of the measured waveforms follow the trends predicted by numerical experiments. The presence of unexpected jitter in the waveforms appears to significantly affect the estimation of the WSF. In particular, a waveform that contains noticeable shock content and unexpected jitter appears to have significantly higher WSF values than the same waveform without the jitter. The WSF has also been shown to be quite insensitive to characteristic frequency, bandwidth, initial statistics, and low sampling rates.

The derivative skewness estimates also follow the trends predicted by numerical experiments. Unlike the WSF, the derivative skewness appears to be rather insensitive to the presence of unexpected jitter, due to the nature of skewness estimates to emphasize outliers. In addition, the derivative skewness appears to be quite sensitive to the presence of shocks in a waveform. However, the derivative skewness also appears to be relatively sensitive to the effects of low sampling rates.

In order to mitigate the weaknesses of the WSF and the derivative skewness, it would be useful to have a very high sampling rate (greater than 204 800 samples/s). When estimating the WSF, it may be wise to low-pass filter the data if there is unexpected high-frequency content. Filtering should be done judiciously, however, as the filter will also smooth the shocks in a waveform. Since the derivative skewness is not as affected by small-scale unexpected noise, it is not as important to filter the waveforms when considering the derivative skewness.

Chapter 6

Application of Nonlinearity Measures to Full-Scale Jet Noise

6.1 Introduction

The nonlinearity measures described in Chapter 3 are applied to full-scale jet noise measurements. These measures will be interpreted using the results found analytically in Chapter 3, numerically in Chapter 4, and experimentally in Chapter 5. Since the previous chapters consisted of idealized cases (such as using plane waves or spherical waves), the comparison of previous results to the results reported in this chapter is not expected to be perfect. However, some insight into the role of nonlinearity in jet noise propagation is obtained from the comparisons.

6.2 Measurement Setup

A large near-field measurement of a Lockheed Martin/Boeing F-22A Raptor was made during 27-30 July 2009 at Holloman Air Force Base, New Mexico. A full overview of the measurement is presented in Reference [56], and a pertinent summary will be given here.

The aircraft was tied down in the center of a 24.4 m (80 ft.) wide concrete pad, with rain-packed dirt on either side of the pad. An upward curving blast deflector was located approximately 30 m (100 ft.) directly behind the aircraft. On the measurement side of the aircraft, there was a small building approximately 25 m to the side a slightly forward of the nozzle and a short wall was located about 30 m from the jet centerline, running parallel to the jet centerline.

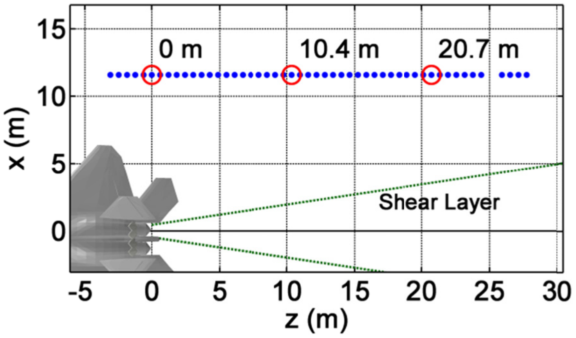

Figure 6.1. Schematic of the measurement locations, relative to the aircraft, used during the July 2009 measurement of noise radiating from an F-22A Raptor. The blue dots represent a fixed array of reference microphones set on the ground. The three circled microphone locations are microphones that are specifically referenced in the text.

Figure 6.1 describes the location of the microphones used during the test. The blue dots represent an array of 50 microphones that were laid on the ground as a fixed array. Several types of microphone were used in the fixed array, including GRAS 6.35 mm (0.25 in) 40BD, 40BE and 40BH prepolarized microphones, and GRAS 3.18 mm (0.125 in) 40DD prepolarized microphones. All of the measurements were recorded using a National Instruments (NI) PXI-1045 Chassis system with NI PXI-4498 and NI PXI-4462 cards as the A/D converters, which streamed data to an NI 8353 rackmount controller with a high-power Intel Core 2 Quad processor and four 250-GB hard drives in a RAID-0 configuration. The entire data acquisition system was monitored using a laptop with a Windows Remote Desktop. The software was a custom designed LabVIEW data acquisition program, which provided setup, microphone calibration, real-time level and spectral monitoring and channel overload alerts. BNC cables ran from the microphones to several NI BNC-2144 InfiniBand-to-BNC breakout boxes. Then bundled InfiniBand cables ran from the breakout boxes to the NI PXI cards.

The distance from the nozzle to the farthest measurement location was less than 23 m, so temperature and wind fluctuations were considered minor. In order to minimize the effects of strong temperature lapses and moderate winds common in the daytime, most measurements were taken in the morning. The average wind speeds did not exceed 2.4 m/s, except for a single row of scans in plane 2 (see Figure 6.1), during which the average wind speed was 5.0 m/s. Temperatures averaged 30°C, with a standard deviation of 4°C.

For every measurement location, the aircraft was fired to operate on condition at idle power and was measured for 30 s at a sampling rate of 96 kHz, then went to an intermediate engine condition and was measured, then went to military engine condition and was measured, and then went to afterburner engine condition and was measured. During the afterburner engine condition the sampling rate was decreased to 48 kHz.

6.3 Waveforms and Spectra

The analyses of measured jet noise presented in this thesis are focused on the measurements at three microphones on the ground array described above. These microphones are labeled in Figure 6.1 by their downstream locations, 0 m, 10.4 m, and 20.7 m. Portions of the waveforms measured at each of these three locations for the intermediate and military engine conditions are shown in Figure 6.2 and Figure 6.3, below.

The portions of the waveforms measured at intermediate engine condition shown in Figure 6.2 suggest the effects of nonlinearity have been relatively unimportant in the noise propagation. The waveforms in plots (a), (c), and (e) do not appear to have experienced very much nonlinear distortion. The expanded waveform portions shown in plots (b), (d), and (f) suggest similar results. In addition, the overall sound pressure levels (OASPLs) of these waveforms (reported in the caption of Figure 6.2) are low with respect to nonlinear processes, noted by the fact that an initially sinusoidal waves with a similar OASPL and characteristic frequency would have a shock formation distance on the order of kilometers. These low levels further suggest that the propagation of the jet noise at intermediate engine condition is dominated by linear phenomena.

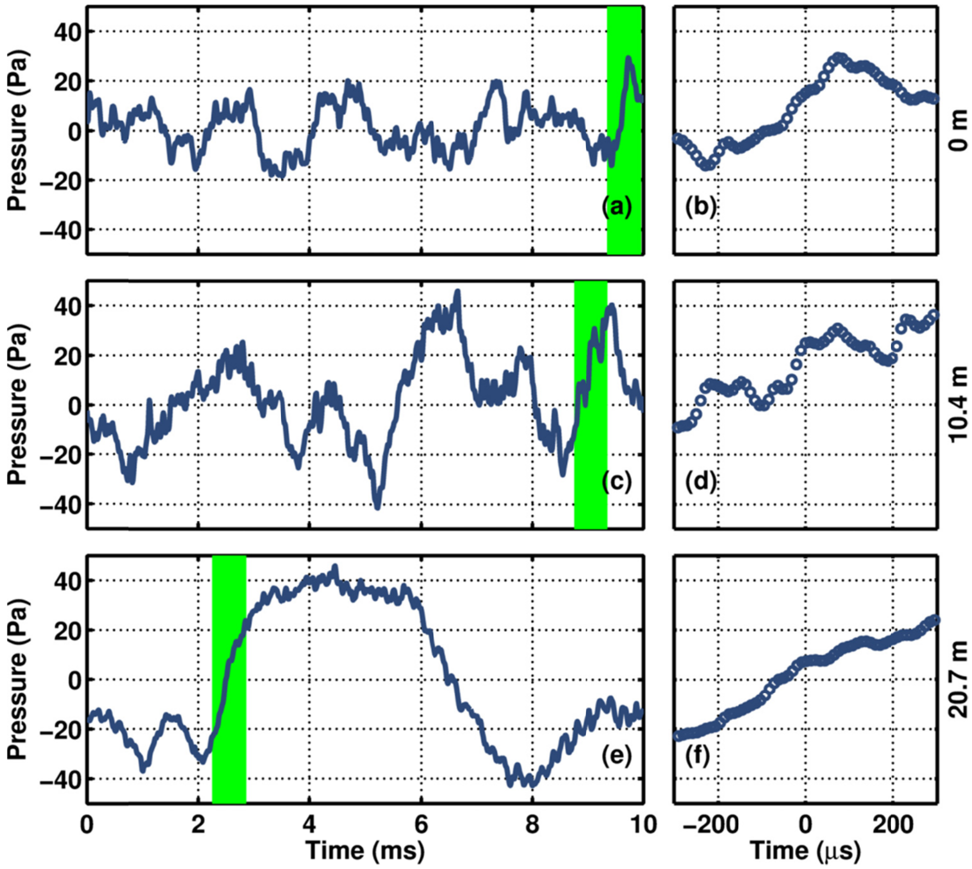

Figure 6.2. Portions of waveforms measured at (a)-(b) 0 m, (c)-(d) 10.4 m, and (e)-(f) 20.7 m downstream of an F22-A Raptor at intermediate engine condition, with overall sound pressure levels of 117 dB (re 20µPa), 120 dB, and 119 dB, respectively. The green region of plots (a), (c), and (e) are shown, expanded and in terms of individual data points, in plots (b), (d), and (f), respectively.

The portions of the waveforms measured at military engine condition shown in Figure 6.3, on the other hand, suggest the effects of nonlinearity have been important in the noise propagation. The waveforms in plots (a), (c), and (e) indicate that nonlinear distortion has decreased rise times and increased fall times of the pressure. In addition, the data points shown in plots (b), (d), and (f) all show what appears to be near discontinuities of the measured pressure, indicating an acoustic shock. Other regions of the waveforms in plots (a), (c), and (e) also suggest shock waves, such as the large pressure rise near 1 ms in plot (c). Finally, the OASPLs of the measured waveforms (reported in the caption of Figure 6.3) are significant for nonlinear processes, noted by the fact that an initially sinusoidal waves with a similar OASPL and characteristic frequency would have a shock formation distance on the order of a hundred meters.

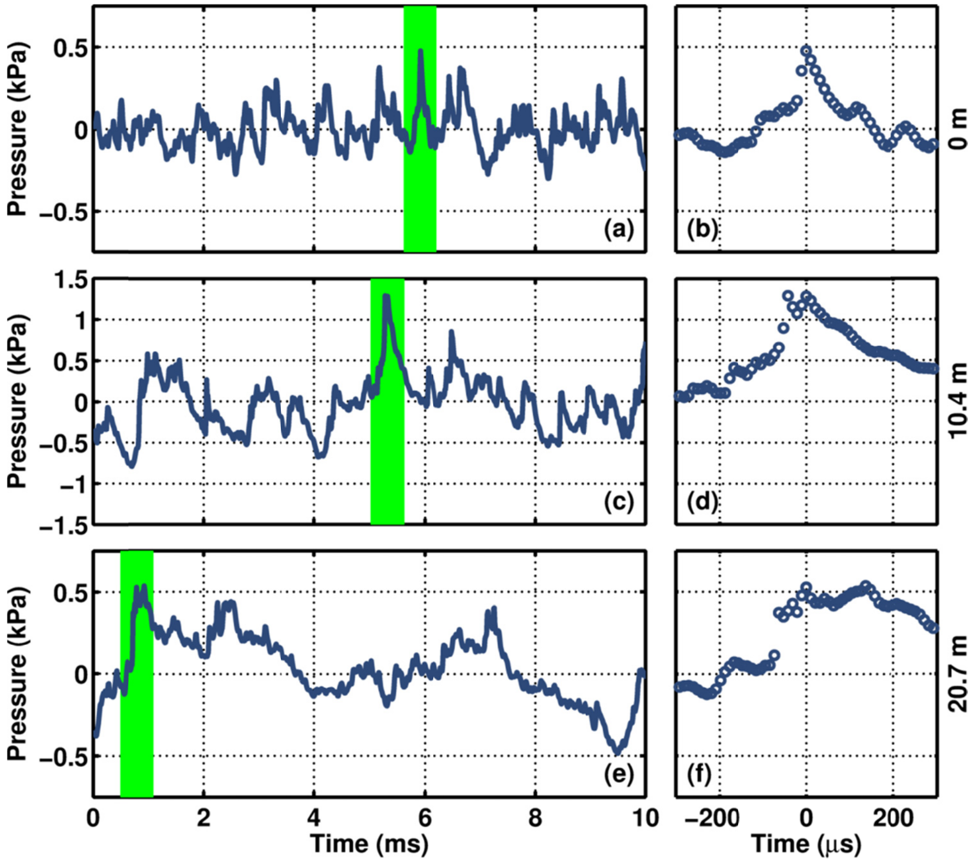

Figure 6.3. Portions of waveforms measured at (a)-(b) 0 m, (c)-(d) 10.4 m, and (e)-(f) 20.7 m downstream of an F22-A Raptor at military engine condition, with overall sound pressure levels of 136 dB (re 20µPa), 146 dB, and 142 dB, respectively. The green region of plots (a), (c), and (e) are shown, expanded and in terms of individual data points, in plots (b), (d), and (f), respectively.

Notice that the waveforms shown in Figure 6.2 and Figure 6.3 appear to have significant high-frequency content, and recall the high-frequency jitter found in the waveforms in the plane wave tube experiments caused the WSF values estimated from the propagated waveforms to be larger than numerical models predict. Regardless of the source of the high-frequency content in the jet noise, it is possible the WSF values estimated from these waveforms would be lower if the high-frequency content were suppressed.

As mentioned in Section 5.4, the effects of nonlinear distortion are also present in the spectra of propagating waveforms. The one-third octave band power spectra of the waveforms being considered here are shown in Figure 6.4, for the waveforms during intermediate engine condition, and in Figure 6.5 for the waveforms during military engine condition. The peak frequencies of the spectra during intermediate engine condition are between 125 Hz and 630 Hz, with peak values ranging from 105 dB (re 20μPa) and 113 dB. The peak frequencies of the spectra during military engine condition are between 125 Hz and 1000 Hz, with peak values ranging from 126 dB to 137 dB. From the very different peak frequencies and values of the spectra from both the intermediate and military engine conditions, it is apparent noise radiating from jets is spatially dependent.

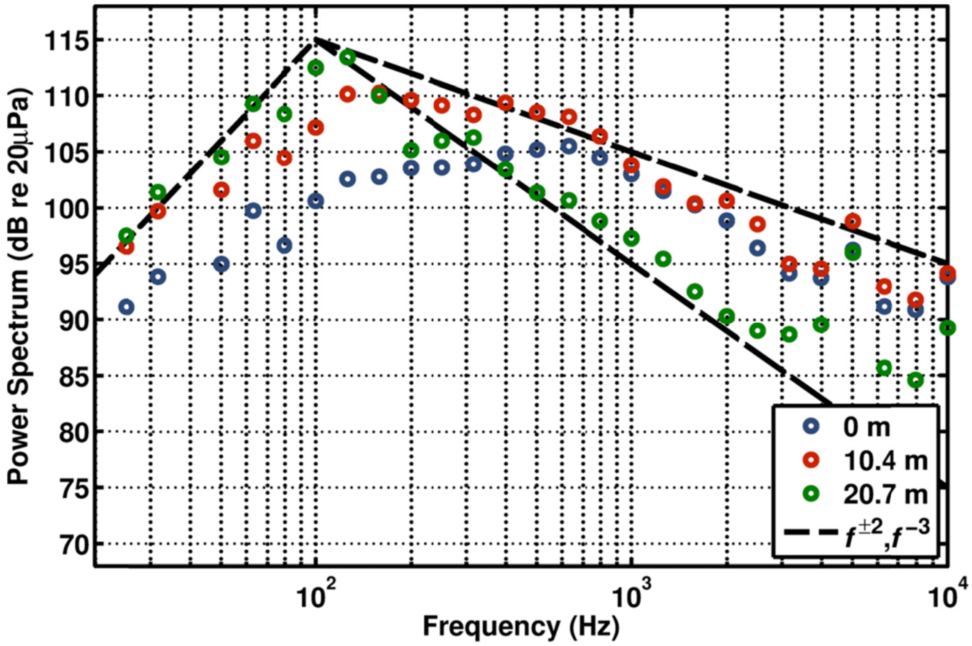

Figure 6.4. One-third octave band power spectra of waveforms measured 0 m, 10.4 m, and 20.7 m downstream of an F22-A Raptor at intermediate engine condition. The dashed lines represent $f^{\pm2}$ and f^{-3} dependencies.

As can be seen in Figure 6.4, the high-frequency spectral shape of the jet noise during the intermediate engine condition is closer to an f^{-3} dependency than f^{-2} dependency. As shown by Rudenko and Soluyan, [14] this spectral shape is characteristic of broadband noise in the pre-shock regime. From this perspective, it is possible that, given a large enough propagation distance, significant shocks could form in the noise. However, since the amplitudes are quite low, as discussed above, it is more likely that the spectral shape is due to source phenomena. [32]

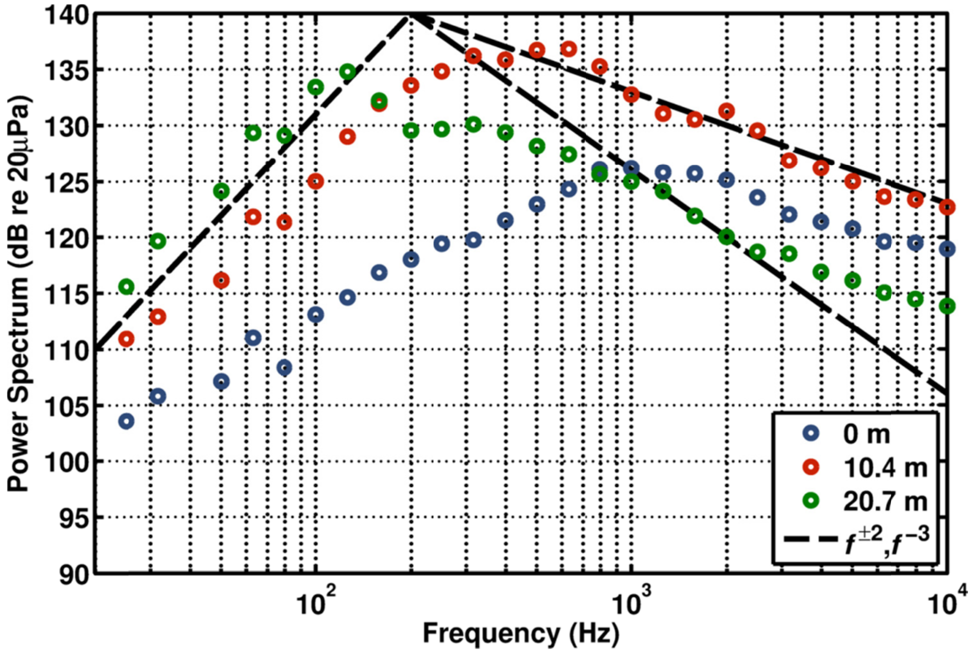

Figure 6.5. One-third octave band power spectra of waveforms measured 0 m, 10.4 m, and 20.7 m downstream of an F22-A Raptor at military engine condition. The dashed lines represent $f^{\pm 2}$ and f^{-3} dependencies.

As is evident in the spectra presented in Figure 6.5, the high-frequency spectral shape of jet noise radiated during military engine condition follows closer to an f^{-2} dependency than to an f^{-3} dependency. Gurbatov and Rudenko reported that an f^{-2} dependency is to be expected in the spectra of waveforms with significant shock content. The spectral shape of the jet noise during military engine condition further supports the claim that nonlinearity is important in the propagation of the noise radiating from an F22-A Raptor at military engine condition. On the other hand, since similar shapes were found for the much lower amplitude intermediate engine condition, it is possible that these spectra are a result of source phenomena.

6.4 A Simple Model of High-Amplitude Noise Propagation

Since jet noise is not planar, it does not make sense to compare the nonlinearity metrics discussed below to the results obtained analytically in Chapter 3 or experimentally in Chapter 5. Given the success of the numerical models in Chapter 4 and Chapter 5 in predicting the propagation of waveforms in a plane wave tube, and in an effort to understand the importance of nonlinearity in a jet noise-like geometry, a numerical model of noise propagating with a geometry similar to jet noise propagation is used to compare the measured waveforms and their associated nonlinearity metrics.

The model consists of initially Gaussian noise with a jet noise-like spectrum that propagates spherically from a source about 5 m downstream of the nozzle. At this distance, the shear layer is approximately 1.2 m is radius (see Figure 6.1). We assume the waveform is known at the edge of the shear layer. In order to estimate the amplitude of the waveform at the shear layer, recall a wave propagating spherically without linear losses decays in amplitude as r^{-1}, where r is the radius from the source region. The overall sound pressure level about 12 m from the source region and on the ground is about 146 dB re 20μPa for the military engine condition. Then, neglecting the ground reflection and absorptive and nonlinear effects, we estimate the overall sound pressure level at the shear layer to be about 166 dB re 20μPa. Given a sampling rate of 96 000 Hz, a characteristic frequency of 750 Hz, and an absorption coefficient of about 4.7×10^{-4} Np/m, we obtain a “spherical Gol’dberg number,” $\Gamma_s = 1/\alpha\bar{r}$, of about 590. (Note that the “spherical Gol’dberg number” is the same as the effective Gol’dberg number defined by Baars et al. except for a factor of $\sqrt{2}$. [28]) By numerically propagating an initially Gaussian noise signal with a jet noise-like spectrum including atmospheric absorption, spherical spreading, and nonlinear propagation phenomena, waveforms are predicted for arbitrary distances from the shear layer. From these waveforms, estimates of the WSF and the derivative skewness are calculated as function of r. The WSF estimates are plotted as a function of σ_s (the distance from the source over the spherical shock formation distance (or, for noise, the nonlinear distortion length); see Equation (2.29)) in Figure 6.6, and the derivative skewness estimates are plotted as a function of σ_s in Figure 6.7.

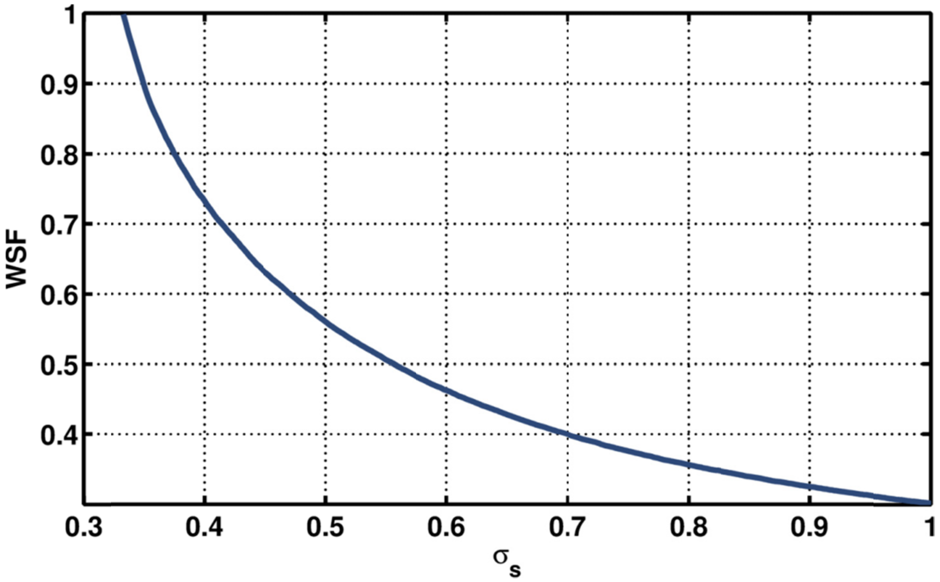

Figure 6.6. Estimates of the WSF of a spherically propagating source as a function of $\sigma_s = r/\bar{r}$. The reference distance is $r_0 = 1.2$ m.

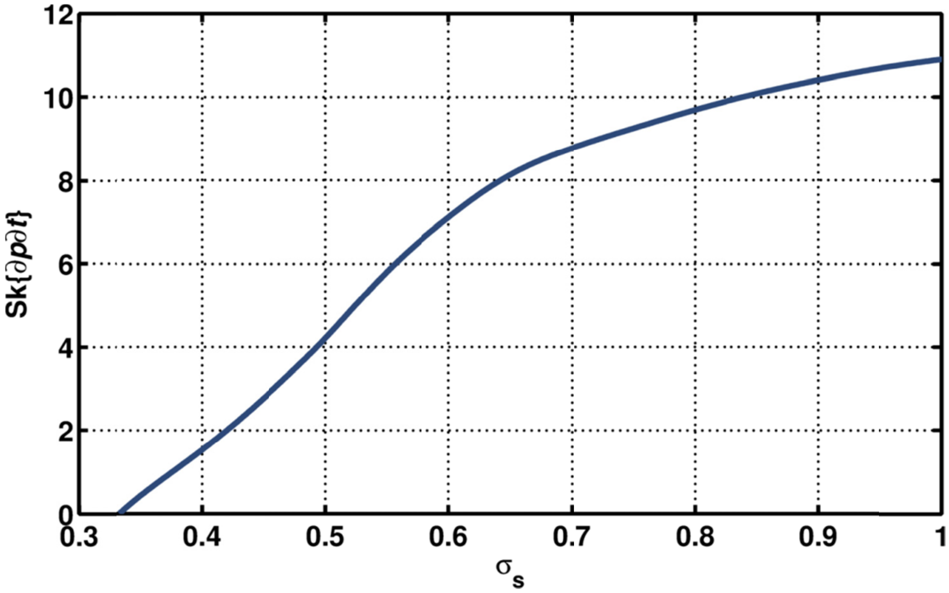

Figure 6.7. Estimates of the derivative skewness of a spherically propagating source as a function of $\sigma_s = r/\bar{r}$. The reference distance is $r_0 = 1.2$ m.

The WSF and derivative skewness estimates shown in Figure 6.6 and Figure 6.7 are somewhat similar to the planar examples shown in Chapter 4, but are more curved. One reason for this is the initial waveform was not defined at $\sigma_s = 0$, but at $\sigma_s = r_0/\bar{r} = 0.33$ in this case. Thus, an estimate that decays according to a power law for small σ_s will not follow a simple line, such as the metrics shown in Chapter 4 do.

By comparing the nonlinearity metrics of this simple jet noise model with estimates of the metrics of measured jet noise waveforms, one may estimate how much nonlinearity has affected measured jet noise waveform.

6.5 Wave Steepening Factor

The WSF estimates of the waveforms measured on the stationary array 0 m, 10.4 m, and 20.7 m downstream (see Figure 6.1) are stated in Table 6.1, below, for intermediate and military engine conditions. In addition, assuming the numerical model proposed in Section 6.4 may be used to model the propagation, an estimate of the σ_s value of the jet noise at the measurement location may be found by comparing the WSF estimates with Figure 6.6. These σ_s values are also presented in Table 6.1.

Table 6.1. Table of calculated WSF for F22-A Raptor noise waveforms measured at three downstream measurement locations and for two engine conditions. Estimates of the associated value of $\sigma_s = r/\bar{r}$ based on the model in Section 6.4 are also included.

Measurement Location	Intermediate Engine Condition		Military Engine Condition	
	WSF	σ_s	WSF	σ_s
0 m	0.985	0.33	0.792	0.38
10.4 m	0.974	0.33	0.621	0.46
20.7 m	0.989	0.33	0.776	0.38

The WSF estimates based on the intermediate engine condition waveforms are all quite high, implying that the characteristic nonlinear distortion length associated with the intermediate engine condition is very large, and that nonlinearity is not very important for this condition. This conclusion is substantiated by the fact that the σ_s values for each of the three measurement locations are 0.33, which is the reference distance. Thus, nonlinearity is not likely to be important for the intermediate engine condition. The WSF estimates based on the military engine condition waveforms are lower than those based on the intermediate engine condition which implies the characteristic nonlinear distortion length associated with the military engine condition is shorter than that for the intermediate engine condition. This claim is also substantiated by the fact that the σ_s values are significantly larger than 0.33, the reference distance.

In order to estimate whether these WSF estimates are an accurate representation of the true noise field, numerical down-sampling may be used to determine the consistency of the WSF values. This analysis consists of decimating a measured waveform to a lower sampling rate than was used for the measurement and then calculating the WSF (or any measure of interest). This process is repeated until the sampling rate is so low the estimates of the WSF become random.

Plots of the WSF estimates as a function of $\nu = f_s/f_{\text{peak}}$, where f_{peak} is the peak frequency of the noise analyzed, are shown in Figure 6.8 for both intermediate and military engine conditions.

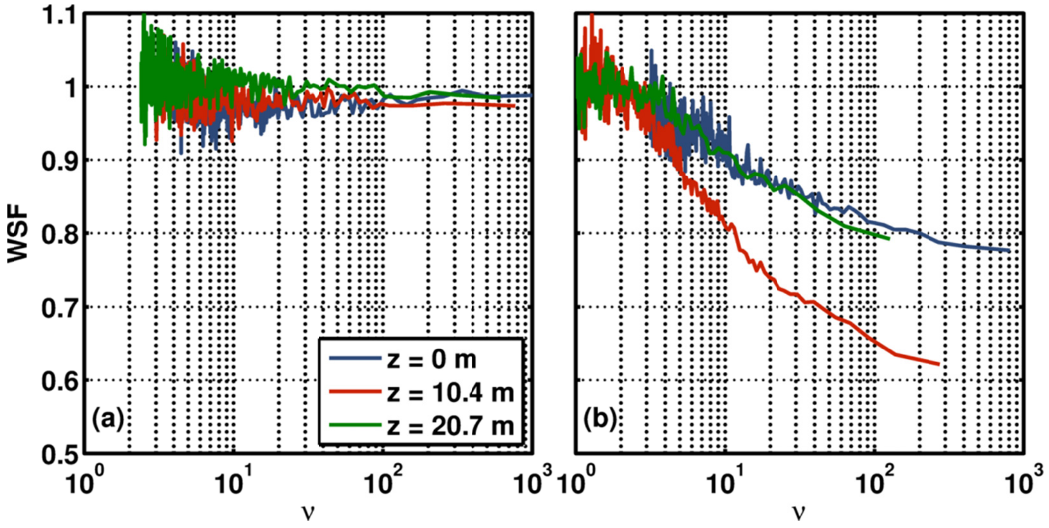

Figure 6.8. Estimates of the wave steepening factor (WSF) of waveforms measured at three downstream locations, 0 m, 10.4 m, and 20.7 m, during (a) intermediate and (b) military engine conditions, plotted as a function of $\nu = f_s/f_{\text{peak}}$.

For low enough values of ν, the behavior of all WSF estimates in Figure 6.8 becomes erratic. This is likely due to the sampling rate being so low the true waveform is being sampled nearly at random. As the value of ν increases, the behavior of the WSF becomes more uniform. For the intermediate engine condition, the WSF of the resampled waveforms approach an asymptotic value as the sampling rate increases, which is near unity. The resampled waveforms for the military engine condition, on the other hand, shows a trend of decreasing values of WSF for increasing values of ν. The rate at which the values of WSF decrease for the military engine condition is about $\nu^{-0.1}$. It is interesting to note this rate of WSF value decay is much slower than the rate predicted in Section 3.3.3.2 for a discretely sampled sawtooth wave, which for large ν goes as ν^{-1}.

Since all real waveforms are continuous, given a sufficiently high sampling rate, the actual WSF would be well estimated, and increasing the sampling rate further would provide negligible improvements to the estimate, which is an asymptotic behavior. In addition, the smoothness of real waveforms suggests that no true WSF would ever reach zero. Therefore, the asymptotic behavior of the WSF estimates for the intermediate engine condition suggests the sampling rate used for the measurement was sufficiently high to estimate the actual WSF value (or the WSF value obtained by continuous sampling) of the noise at intermediate engine condition. However, the fact that the WSF estimates for the military engine condition do not level out to some positive value suggests the sampling rate used was insufficient to estimate the actual WSF of the noise at military engine condition, and the actual WSF value is lower than the reported value. Since the rate at which the WSF values decrease with respect to ν for the military engine condition is significantly less than the sawtooth limit of ν^{-1} or the Fubini-Earnshaw formula of ν^{-2}, it may be some aspect of the waveform with a very short time scale (such as the high-frequency content) may have a strong influence on the estimation of the WSF. If the actual WSF value of the noise during military engine condition is lower than the reported value, then the values of σ for the noise estimated above are low.

6.6 Derivative Skewness

The derivative skewness estimates of the waveforms measured on the stationary array 0 m, 10.4 m, and 20.7 m downstream (see Figure 6.1) are stated in Table 6.2, below, for the intermediate and military engine conditions. In addition, assuming the numerical model proposed in Section 6.4 may be used to model the propagation, an estimate of the σ_s value of the jet noise at the measurement location may be found by comparing the WSF estimates with Figure 6.7. These σ_s values are also presented in Table 6.2.

Table 6.2. Table of calculated derivative skewness values for F22-A Raptor noise waveforms measured at three downstream measurement locations and for two engine conditions. Estimates of the associated value of $\sigma_s = r/\bar{r}$ based on the model in Section 6.4 are also included.

Measurement Location	Intermediate Engine Condition		Military Engine Condition	
	Derivative Skewness	σ_s	Derivative Skewness	σ_s
0 m	0.0593	0.33	1.33	0.39
10.4 m	0.0879	0.34	5.54	0.54
20.7 m	0.0463	0.33	2.79	0.45

The results found in the analysis of the WSF estimates based on the ground array of microphones given in Section 6.5 are corroborated by the derivative skewness estimates. The derivative skewness values for the intermediate engine condition are small, and suggest that nonlinearity is not important in the propagation of the noise radiating at intermediate engine condition. The derivative skewness values at military engine condition are significantly higher, and the estimated σ_s values are of the same range that the σ_s values estimated using the WSF are, and so nonlinearity is likely to be important in the propagation of jet noise at military engine condition. The consistency of the estimated values of σ_s using the WSF and using the derivative skewness suggests that the model used is valid for the waveforms considered.

It should be noted the interpretation of the WSF and the derivative skewness values in terms of σ_s relies upon the validity of the model presented in Section 6.4. However, this simple model is far from an accurate representation of jet noise propagation. Jets are complicated, extended sources, and the results found in this and the previous section should be interpreted in light of this limitation. For example, the geometry of jet noise propagation is neither spherical nor cylindrical, but somewhere in between, is directional, and is frequency dependent. Since the model used here assumed purely spherical propagation, this would suggest that the source amplitude is somewhat lower than the signal used for these analyses, and decay more slowly. The non-spherical geometry would likely change the overall shape of the evolution of the nonlinearity metrics, and therefore change the estimated σ_s values (or some generalization of σ_s for non-spherical, non-cylindrical geometries). While it is unknown how these differences will affect the quantitative interpretation of the WSF and derivative skewness, the author does not think that the qualitative interpretation will change significantly.

In order to estimate whether the derivative skewness estimates tabulated in Table 6.2 are an accurate representation of the true noise field, numerical down-sampling may be used to determine whether the skewness behavior for lower sampling rates. This analysis is very similar to that presented for the WSF in the prior section. The down-sampling analyses of the derivative skewness for the measured waveforms during both intermediate and military engine conditions are shown in Figure 6.9. The analytical derivative skewness of a sawtooth waveform derived in Section 3.3.3.2 is also shown in Figure 6.9, for comparison.

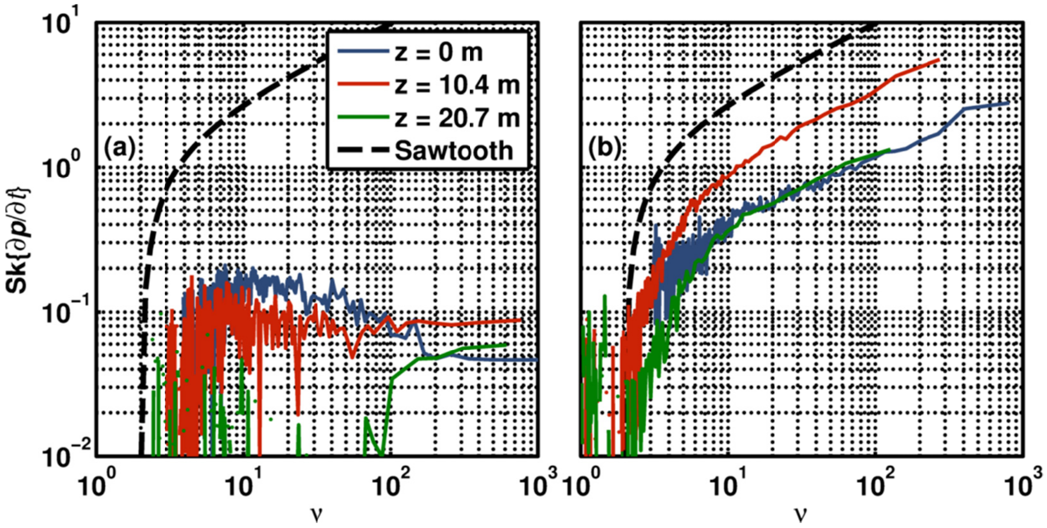

Figure 6.9. Plots of the estimates of the skewness of the first time-derivative of the pressure amplitudes (derivative skewness) of waveforms measured at three downstream locations, 0 m, 10.4 m, and 20.7 m, during (a) intermediate and (b) military engine conditions, plotted as a function of $\nu = f_s/f_{\text{peak}}$. The analytical derivative skewness obtained by assuming a discretely sampled sawtooth wave is also plotted, for comparison.

The characteristics of the down-sampled derivative skewness estimates are similar to those of the down-sampled WSF estimates. For very low values of ν all of the derivative skewness estimates become somewhat erratic, and for high values of ν all of the estimates follow a consistent trend. The derivative skewness estimates for the intermediate engine condition appear to reach an asymptotic value, though only for sampling rates close to the measurement sampling rate. This suggests the sampling rate of 96 000 samples/s is capable of resolving the derivative skewness for the radiate noise of the intermediate engine condition. Notice the behavior of the derivative skewness of the waveforms measured during the intermediate engine condition do not follow the predicted derivative skewness of a sawtooth wave. This is indicative of the lack of significant shock content in the waveforms measured during the intermediate engine condition.

The derivative skewness estimates for the military engine condition do not appear to approach any asymptotic value, but continue to increase for increasing ν. Also notice that the derivative skewness estimates for all three measurement locations increase approximately at the same rate that is predicted for the sawtooth wave. This implies that the radiated noise for the military engine condition is significantly more similar to a sawtooth wave than the radiated noise for the intermediate engine condition is. As mentioned above, since physical waveforms are continuous, we may assume there is an asymptotic estimate of the derivative skewness, even for jet noise radiated during the military engine condition. Therefore, it is likely if the waveforms had been sampled at a much higher sampling rate the derivative skewness estimates would level out and depart from the sawtooth wave trend, which inherently diverges. From this we conclude a sampling rate of 96 000 samples/s, which was used during the measurement, is insufficient for the purposes of estimating the true derivative skewness of the noise radiating from an F22-A Raptor at military engine condition. However, comparisons of the derivative skewness values for the military engine conditions with derivative skewness values based on other waveforms which have also reached a sawtooth wave-like behavior will still yield information about the relative importance of nonlinearity.

6.7 Nonlinearity Metric Evolution with Propagation

In addition to the ground-based measurements, large aperture scans of the acoustic field near the aircraft were taken. See Wall et al. [56] for a summary of the measurement. Maps of the overall sound pressure levels measured during the military and afterburner engine conditions are shown below in Figure 6.10. Since the waveforms measured at military engine condition were sampled at a rate of 96 000 Hz while the waveforms measured at afterburner engine condition were sampled at a rate of 48 000 Hz, a direct comparison of the nonlinearity metrics would not be meaningful. In order to make a meaningful comparison, the waveforms measured at military engine condition were down-sampled (by decimation) to 48 000 Hz.

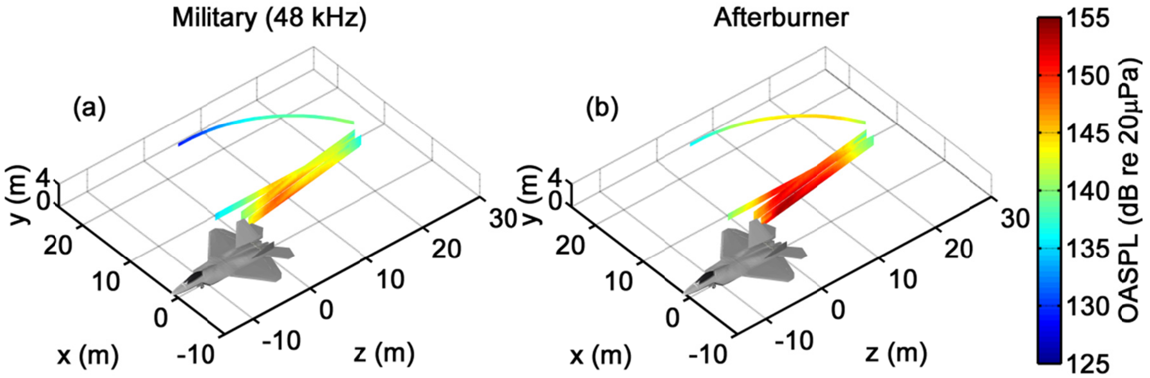

Figure 6.10. Maps of the overall sound pressure level of waveforms measured of an F22-A Raptor at (a) military and (b) afterburner engine condition.

By analyzing the nonlinearity metrics of the waveforms from these scans, information about the how nonlinearity affects jet noise propagation can be obtained. Maps of the WSF of the scans for military and afterburner engine conditions are shown in Figure 6.11, and maps of the derivative skewness of the scans are shown in Figure 6.12. The intermediate engine condition is not shown, due to the fact there is not a set “intermediate” thrust position in the F-22A Raptor, leading to some subjectivity and variation in the source characteristics from run to run. Since the military engine condition was measured with a sampling rate of 96 kHz and the afterburner engine condition was measured with a sampling rate of 48 kHz, a direct comparison of the metrics would not be appropriate, since using different sampling rates would yield different values for the same waveform, as discussed in Chapter 3. For this reason, the waveforms measured for the military engine condition were first resampled (via decimation) to a sampling rate of 48 kHz before the metrics were estimated.

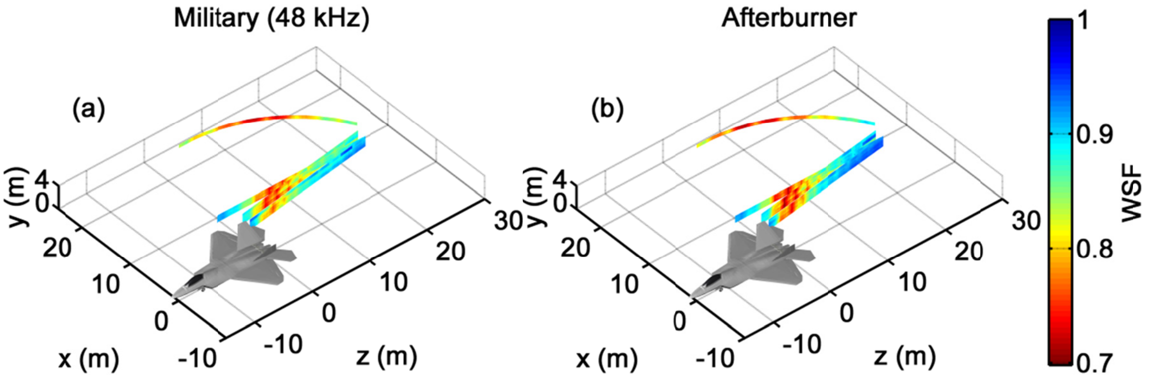

Figure 6.11. Maps of the wave steepening factor (WSF) of jet noise radiating from an F-22A Raptor at (a) military engine condition and at (b) afterburner engine condition.

The maps in Figure 6.11 show that the WSF of jet noise evolves with some directivity. The lowest WSF value estimated from the military and afterburner engine conditions are 0.71 and 0.70, respectively. Based on the analytical forms of the WSF derived in Chapter 3, these WSF values appear to be large, indicating that nonlinearity is not significant for jet noise propagation. However, high-frequency content in the measured waveforms may increase the estimated WSF values. A region of especially low WSF (recall low WSF implies significant nonlinearity) seems to exist for the military engine condition about a ray originating about 5 m downstream of the nozzle and about 113° relative to the aircraft. A similar ray exists for the afterburner engine condition. In both cases, the region about the ray with significantly lower values of WSF becomes larger as the distance from the source region about 5 m downstream of the nozzle increases. The growth of the region of low WSF suggests that the WSF may be noticeably decreasing with propagation, indicating nonlinearity is important for jet noise propagation for both military and afterburner engine conditions.

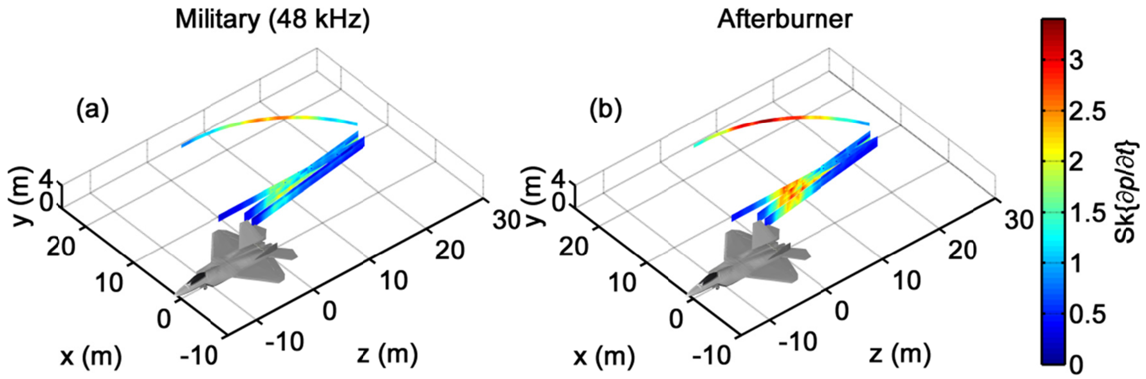

Figure 6.12. Maps of the derivative skewness of jet noise radiating from an F-22A Raptor at (a) military engine condition (waveforms down-sampled to a sampling rate of 48 kHz from a rate of 96 kHz) and at (b) afterburner engine condition (initially sampled at 48 kHz).

The maps of the derivative skewness shown in Figure 6.12 also show the directional behavior the maps of the WSF estimates do. However, the derivative skewness values show a more significant difference between the military and afterburner engine conditions than the WSF maps do. The maximum estimate of the derivative skewness for the down-sampled military engine condition is 2.7, which is significantly less than the 3.4 for the afterburner condition. It should be noted the maximum derivative skewness value for a sawtooth wave with a frequency of 960 Hz, discretely sampled at a rate of 48 000 Hz, is about 7.

Using the down-sampled waveforms for the military engine condition also shows how the derivative skewness estimates in the measurement planes close to the jet are larger in the afterburner engine condition than for the military engine condition, and shows the derivative skewness estimates continue to increase as distance from the nozzle increases for both conditions. These findings emphasize the range and amplitude dependent evolution of the skewness of the time-derivative of the pressure waveforms of high-amplitude jet noise.

6.8 Conclusions

Estimated values of the WSF and derivative skewness of the noise suggest nonlinearity is more important in the propagation of jet noise at military engine condition in the near field than for intermediate engine condition. In particular, the noise radiating from an F-22A Raptor at intermediate engine condition does not appear to be significantly distorted due to nonlinear propagation, nor does it appear to have formed shocks. On the other hand, noise measured within 20 m of an F-22A Raptor at military engine condition does appear to be significantly distorted, and shocks have either formed or are forming in the waveforms.

In addition, maps of the spatial evolution of the WSF and the derivative skewness for an F-22A Raptor at military and afterburner engine conditions were presented. For both engine conditions and for both metrics, significant evidence of nonlinear distortion was found. In order to compare the two engine conditions, the waveforms measured at military engine condition were downsampled to the sampling rate used for the afterburner engine condition. The comparison of the WSF does not show significant differences, but the comparison of the derivative skewness indicates that nonlinearity plays a more significant role in the propagation of noise at afterburner engine condition than at military engine condition.

Chapter 7

Concluding Discussion

7.1 Conclusions

This thesis has presented analytical, numerical, and experimental descriptions of how two nonlinearity metrics, the wave steepening factor (WSF) and the skewness of the time-derivative of a time waveform (derivative skewness). Qualitatively, the WSF quantifies the distortion of a waveform due to nonlinear propagation, and the derivative skewness quantifies the shock content of a waveform.

The evolution of the WSF and the derivative skewness have been analytically described for several important ideal propagation models, the Earnshaw, the Fubini, the Fay, and the Khokhlov solutions to the case of an initially sinusoidal plane wave propagating with and without thermoviscous absorption. In particular, the WSF of the Earnshaw solution is given by

$$\mathrm{WSF} = \frac{\pi - 2\sigma}{\pi + 2\sigma}, \tag{7.1}$$

where σ is the distance from the source over the shock formation distance of an initially sinusoidal signal, and the WSF of the Khokhlov solution is given by

$$\mathrm{WSF} = \left[\frac{\dfrac{\pi^2\Gamma}{2(\sigma+1)}}{\cosh^{-1}\sqrt{\dfrac{\pi^2\Gamma}{2(\sigma+1)}}} - 1\right]^{-1}, \tag{7.2}$$

where Γ is the Gol'dberg number of the initially sinusoidal signal. The derivative skewness of the Fubini solution is

$$\mathrm{Sk}\{\partial p/\partial t\} = \frac{3}{\sqrt{2}}\frac{\sum_{n=1}^{\infty}\sum_{m=1}^{\infty}\sum_{l=1}^{\infty}J_n(n\sigma)J_m(m\sigma)J_l(l\sigma)\delta_{n+m,l}}{\left[\sum_{n=1}^{\infty}J_n^2(n\sigma)\right]^{3/2}}, \tag{7.3}$$

where $\delta_{n,m}$ is the Kronecher delta function and J_n is the n^{th} order Bessel function of the first kind, the derivative skewness of the Earnshaw solution (which is equivalent to the Fubini solution for $\sigma \leq 1$) is

$$\mathrm{Sk}\{\partial p/\partial t\} = \frac{2(1-\sigma^2)^{3/2} + 3\sigma^2 - 2}{(1-\sigma^2)^{3/4}\left(1-\sqrt{1-\sigma^2}\right)^{3/2}}, \tag{7.4}$$

and the derivative skewness of the Fay solution is

$$\mathrm{Sk}\{\partial p/\partial t\} = \frac{3}{\sqrt{2}}\frac{\sum_{n=1}^{\infty}\sum_{m=1}^{\infty}\sum_{l=1}^{\infty}\dfrac{n}{\sinh\left(n\dfrac{\sigma+1}{\Gamma}\right)}\dfrac{m}{\sinh\left(m\dfrac{\sigma+1}{\Gamma}\right)}\dfrac{l}{\sinh\left(l\dfrac{\sigma+1}{\Gamma}\right)}\delta_{n+m,l}}{\left[\sum_{n=1}^{\infty}\dfrac{n^2}{\sinh^2\left(n\dfrac{\sigma+1}{\Gamma}\right)}\right]^{3/2}}. \tag{7.5}$$

By assuming that nonlinear distortion of a waveform due to propagation is relatively minor for $\sigma < 0.2$ for an initially sinusoidal plane wave propagating without linear losses, it has been further found that a WSF value of about 0.75 is high, indicating low waveform distortion, and that a derivative skewness values of 0.5 may be considered low, indicating that shocks have not started to form significantly. Furthermore, by assuming that cumulative nonlinear effects are quite substantial for $\sigma > 0.9$ for an initially sinusoidal plane wave propagating without linear losses, it has been found that a WSF value of 0.25 may be considered low, indicating significant waveform distortion due to nonlinear propagation, and that a derivative skewness value of 5 may be considered high, indicating that shocks are (or soon will be) present in the waveform.

In addition to the exact forms of the WSF and derivative skewness given above, a discussion of the effects of finite sampling rates on the estimation of the WSF and derivative skewness values of these ideal models has been presented. It was shown that the estimate of the WSF of a sawtooth wave is approximately f/f_s, where f_s is the sampling rate and f is the sawtooth frequency, and that the derivative skewness of a sawtooth wave is approximately $\sqrt{f_s/f}$. In general, it appears that the WSF is less sensitive to low sampling rates than the derivative skewness.

Due to the difficulty of considering arbitrary source signals or realistic absorption and dispersion in analytical propagation models including nonlinear phenomena, a numerical propagation model was used to study the effects of noise and realistic absorption and dispersion on the evolution of the WSF and the derivative skewness. By numerically propagating an initially sinusoidal plane wave with thermoviscous absorption, a transition region between the Earnshaw and Fay/Khokhlov solutions was described for the WSF and derivative skewness for two values of the Gol'dberg number. By considering an initially sinusoidal plane wave propagating with plane wave tube-absorption and -dispersion, it was found that the slower growth of absorption with frequency associated with boundary layer absorption caused nonlinearity to become more important with propagation relative to propagation with thermoviscous absorption, as noted by lower values of the WSF and higher values of the derivative skewness. Finally, the importance of nonlinearity in an initially broadband, planar Gaussian noise signal propagating with plane wave tube-absorption and -dispersion was found to be greater than for the initially sinusoidal case, as suggested by Gurbatov and Rudenko. [43]

In order to validate the numerically obtained data, the evolution of nonlinearity metrics of waveforms measured inside a plane wave tube was analyzed. Significant agreement was found between the numerically and experimentally obtained WSF values and derivative skewness values for $\sigma < 1.2$. The difference between the trends for $\sigma > 1.2$ may be attributed to unexpected jitter in the measured waveforms. This small-amplitude, high-frequency phenomenon was found to significantly increase the WSF value of the waveform, indicating that small disturbances in a waveform will mean that the WSF will predict that nonlinearity is less important than it would if the disturbances were not present. On the other hand, the derivative skewness did not appear to be as dramatically affected by the unexpected oscillations in the measured waveforms. The reason for this is that the cubic nature of the skewness will emphasize the largest slopes and suppress the smallest slopes.

These conclusions, based on analytical, numerical, and experimental evidence, were applied to jet noise. The WSF and derivative skewness of a spherically propagating Gaussian waveform with a jet noise-like spectrum were numerically evaluated, and then compared with the WSF and derivative skewness values of measured waveforms of an F-22A Raptor at intermediate and military engine conditions. Nonlinearity in the radiated noise at intermediate engine condition was found to be not very significant, while nonlinearity in the radiated noise at military engine condition was found to be quite significant. In particular, the noise measured about 12 m from the source region in the direction of greatest intensity during military engine condition had WSF values and derivative skewness values similar to the simple spherical wave model at $\sigma_s = 0.5$, where σ_s is the distance from the source region relative to the spherical shock formation distance (or nonlinear distortion length for noise). As further evidence, maps of the WSF and derivative skewness near the F-22A Raptor, based on scans designed to be used for near-field acoustical holography, were shown for military and afterburner engine conditions. Both metrics suggest that nonlinearity becomes more important with greater distance from the source in the direction of greatest amplitude for both engine conditions, providing further insight into the nature of jet noise near fields.

7.2 Future Work

While this thesis has described how two measures of the importance of nonlinearity in jet noise evolve using analytical and experimental means, there is still much that should be done to improve understanding of these measures. The theoretical work shown in Chapter 2 has been focused entirely on understanding the evolution of measures of nonlinearity for the case of an initially sinusoidal signal. While this is an important benchmark case, most real-world problems will deal with more complicated signals. Extending the theoretical work presented in this thesis to include initially Gaussian noise and noise with jet noise-like statistics would help our understanding of how measures of nonlinearity in measured jet noise should be interpreted.

Another limitation of the theoretical work presented in this thesis is that all derivations assumed planar propagation and either no losses or only thermoviscous losses. Analytical or numerical analysis of how geometrical spreading, such as cylindrical or spherical spreading, and more general propagation losses affect the evolution of measures of nonlinearity can also be useful in interpreting jet noise data.

The measurements of noise propagating in a plane wave tube presented in Chapter 3 have shown how different characteristic frequencies, bandwidths and initial statistics can affect the evolution nonlinearity measures. However, oscillations in the measured waveforms that are not due to the planar propagation of the source signal somewhat diminish the utility of the metrics estimated from these waveforms. The experimental setup may be improved by ensuring that the couplings between segments of the plane wave tube are smooth, such as by custom-designing couplers, or by using a single, long tube instead of segments. Since nonlinear processes transfer energy to higher frequencies, cross modes in the plane wave tube may corrupt the measured data. Using lower characteristic frequencies than those used here or using a narrower tube may help in the reduction of energy transferred to cross modes, although this would increase boundary-layer absorption as well.

Comparing the theoretical and experimental evolution of measures of nonlinearity of noise with measured jet noise has given insight into the nature of nonlinear processes in jet noise propagation. However, the measurements used for this thesis is a small subset of a very large set of jet noise measurements. Analyzing all of these data will take time, but this analysis will likely give insight into the spatial dependence and the physical processes associated with the importance of nonlinearity in jet noise.

References

[1] M. J. Lighthill, "On sound generated aerodynamically," *Proc. R. Soc. Lond. A,* vol. 211, pp. 564-587, 1952.

[2] D. F. Pernet and R. C. Payne, "Non-linear propagation of signals in air," *J. Sound Vib.,* vol. 17, no. 3, pp. 383-396, 1971.

[3] A. T. Wall, K. L. Gee, T. B. Neilsen, D. W. Krueger, M. M. James, S. D. Sommerfeldt and J. D. Blotter, "Full-scale jet noise characterization using scan-based acoustical holography," *AIAA,* pp. AIAA-2012-2081, 2012.

[4] D. T. Blackstock, M. F. Hamilton and A. D. Pierce, "Progressive waves in lossless and lossy fluids," in *Nonlinear Acoustics*, Acoustical Society of America, 2008, pp. 65-150.

[5] F. H. Fenlon, "An extension of the Bessel-Fubini series for a multiple-frequency cw acoustic source of finite amplitude," *J. Acoust. Soc. Am.,* vol. 51, no. 1, pp. 284-289, 1972.

[6] D. A. Webster and D. T. Blackstock, "Finite-amplitude saturation of plane sound waves in air," *J. Acoust. Soc. Am.,* vol. 62, no. 3, pp. 518-523, 1977.

[7] I. Rudnick, "On the attenuation of a repeated sawtooth shock wave," *J. Acoust. Soc. Am.,* vol. 25, no. 5, pp. 1012-1013, 1953.

[8] F. M. Pestorius, "Propagation of plane acoustic noise of finite-amplitude," Technical Report ARL-TR-73-23, Applied Research Laboratories, The University of Texas at Austin, AD 778868, 1973.

[9] F. M. Pestorius and D. T. Blackstock, "Propagation of finite-amplitude noise," in *Finite-*

amplitude wave effects in fluids, Copenhagen, 1973.

[10] D. T. Blackstock, "Generalized Burgers equation for plane waves," *J. Acoust. Soc. Am.,* vol. 77, no. 6, pp. 2050-2053, 1985.

[11] D. T. Blackstock, ""Once nonlinear, always nonlinear"," in *17th International Symposium on Nonlinear Acoustics*, State College, PA, 2005.

[12] F. M. Pestorius, S. W. Williams and D. T. Blackstock, "Effect of nonlinearity on noise propagation," in *Proc. 2nd Interagency Symposium on University Research in Transportation Noise*, North Carolina State University, Raleigh, NC, 1974.

[13] K. L. Gee, V. W. Sparrow, M. M. James, J. M. Downing and C. M. Hobbs, "Measurement and prediction of nonlinearity in outdoor propagation of periodic signals," *J. Acoust. Soc. Am.,* vol. 120, no. 5, pp. 2491-2499, 2006.

[14] O. V. Rudenko and S. I. Soluyan, Theoretical Foundations of Nonlinear Acoustics, Moscow, USSR: Plenum Publishing Corporation, 1975.

[15] J. F. Scott, "The nonlinear propagation of acoustic noise," *Proc. R. Soc. Lond.,* vol. 383, pp. 55-70, 1982.

[16] D. G. Crighton and J. F. Scott, "Asymptotic solutions of model equations in nonlinear acoustics," *Phil. Trans. R. Soc. Lond.,* vol. 292, pp. 101-134, 1979.

[17] S. N. Gurbatov, A. N. Malakhov and A. I. Saichev, Nonlinear random waves and turbulence in nondispersive media: waves, rays, particles, New York: Manchester University Press, 1991.

[18] J. Gallagher, "The effect of non-linear propagation in jet noise," in *20th Aerospace Sciences Meeting and Exhibit: AIAA*, Orlando, FL, 1982.

[19] C. L. Morfey and G. P. Howell, "Nonlinear Propagation of Aircraft Noise in the Atmosphere," *AIAA Journal,* vol. 19, no. 8, pp. 986-992, 1981.

[20] C. L. Morfey, "Aperiodic signal propagation at finite amplitudes: some practical applications," in *Proceedings of the 10th International Symposium on Nonlinear Acoustics*, Kobe, Japan, 1984.

[21] K. L. Gee, V. W. Sparrow, T. B. Gabrielson and A. A. Atchley, "Nonlinear modeling of F/A-18E noise propagation," *AIAA,* pp. AIAA-2005-3089, 2005.

[22] K. L. Gee, V. W. Sparrow, M. M. James, J. M. Downing, C. M. Hobbs, T. B. Gabrielson and A. A. Atchley, "Measurement and Prediction of Noise Propagation from a High-Power Jet Aircraft," *AIAA Journal,* vol. 45, no. 12, pp. 3003-3006, 2007.

[23] K. L. Gee, V. W. Sparrow, M. M. James, J. M. Downing, C. M. Hobbs, T. B. Gabrielson and A. A. Atchley, "The role of nonlinear effects in the propagation of noise from high-power jet aircraft," *J. Acoust. Soc. Am.,* vol. 123, pp. 4082-4093, 2008.

[24] K. L. Gee, J. M. Downing, M. M. James, R. C. McKinley, R. L. McKinley, T. B. Neilsen and A. T. Wall, "Nonlinear Evolution of Noise from a Military Jet Aircraft during Ground Run-up," *AIAA,* 2012.

[25] K. L. Gee, T. B. Neilsen, J. M. Downing, M. M. James, R. L. McKinley and R. C. McKinley, "Near-field shock formation in noise propagation from a high-power jet aircraft," *J. Acoust. Soc. Am.,* vol. 133, no. 2, pp. EL88-EL93, 2013.

[26] S. McInerny, K. L. Gee, M. Downing and M. James, "Acoustical nonlinearities in aircraft flyover data," *AIAA,* 2007.

[27] B. P. Petitjean, K. Viswanathan and D. K. McLaughlin, "Acoustic pressure waveforms measured in high speed jet noise experiencing nonlinear propagation," *International Journal of Aeroacoustics,* vol. 5, no. 2, pp. 193-215, 2006.

[28] W. Baars, C. Tinney and M. Wochner, "Nonlinear distortion of acoustic waveforms from high-speed jets," *Journal of Fluid Mechanics,* (in press).

[29] K. L. Gee, A. A. Atchley, L. E. Falco, M. R. Shepherd, L. S. Ukeiley, B. J. Jansen and J. M.

Seiner, "Bicoherence analysis of model-scale jet noise," *J. Acoust. Soc. Am.,* vol. 128, no. 5, pp. EL211-EL216, 2010.

[30] K. L. Gee, T. B. Neilsen and A. A. Atchley, "Skewness and shock formation in laboratory-scale supersonic jet data," *J. Acoust. Soc. Am.,* vol. 133, no. 6, pp. EL491-EL497, 2013.

[31] L. Falco, K. Gee, A. Atchley and V. Sparrow, "Investigation of a single-point nonlinearity indicator in one-dimensional propagation," in *Forum Acusticum*, Budapest, 2005.

[32] T. B. Neilsen, K. L. Gee, A. T. Wall and M. M. James, "Similarity spectra analysis of high-performance jet aircraft noise," *J. Acoust. Soc. Am.,* vol. 133, no. 4, pp. 2116-2125, 2013.

[33] S. A. McInerny and S. M. Ölçmen, "High-intensity rocket noise: Nonlinear propagation, atmospheric absorption, and characterization," *J. Acoust. Soc. Am.,* vol. 117, no. 2, pp. 578-591, 2005.

[34] J. E. Ffowcs-Williams, J. Simson and V. J. Virchis, "'Crackle': An annoying component of jet noise," *Journal of Fluid Mechanics,* vol. 71, no. 2, pp. 251-271, 1975.

[35] K. L. Gee, V. W. Sparrow, A. Atchley and T. B. Gabrielson, "On the perception of crackle in high-amplitude jet noise," *AIAA Journal,* vol. 45, no. 3, pp. 593-598, 2007.

[36] D. G. Crighton, "Nonlinear Acoustic Propagation of Broadband Noise," in *Recent Advances in Aeroacoustics*, New York, Springer New York, 1986, pp. 411-454.

[37] M. R. Shepherd, K. L. Gee and A. D. Hanford, "Evolution of statistical properties for a nonlinearly propagating sinusoid," *J. Acoust. Soc. Am.,* vol. 130, no. 1, pp. EL8-EL13, 2011.

[38] M. B. Muhlestein and K. L. Gee, "Experimental investigation of a characteristic shock formation distance in finit-amplitude noise propagation," in *Proc. Mtgs. Acoust.*, 2011.

[39] A. Larraza, B. Denardo and A. Atchley, "Absorption of sound by noise in one dimension," *J. Acoust. Soc. Am.,* vol. 100, no. 6, pp. 3554-3560, 1996.

[40] A. Steinwolf, R. G. White and H. F. Wolfe, "Simulation of jet-noise excitation in an acoustic

progressive wave tube facility," *J. Acoust. Soc. Am.,* vol. 109, no. 3, pp. 1043-1052, 2001.

[41] M. F. Hamilton and C. L. Morfey, "Model Equations," in *Nonlinear Acoustics*, Acoustical Society of America, 1998, pp. 41-63.

[42] D. T. Blackstock, "Connection between the Fay and Fubini solutions for plane sound waves of finite amplitude," *J. Acoust. Soc. Am.,* vol. 39, no. 6, pp. 1019-1026, 1966.

[43] S. N. Gurbatov and O. V. Rudenko, "Statistical Phenomena," in *Nonlinear Acoustics*, M. F. Hamilton and D. T. Blackstock, Eds., Acoustical Society of America, 2008, pp. 377-398.

[44] H. E. Bass, L. C. Sutherland, A. J. Zuckerwar, D. T. Blackstock and D. M. Hester, "Atmospheric absorption of sound: Further developments," *J. Acoust. Soc. Am. 97(1), 680-683 (1995), and "erratum: Atmospheric absorption of sound: Further developments,: J. Acoust. Soc. Am. 99(2), 1259 (1996).*

[45] D. T. Blackstock, Fundamentals of Physical Acoustics, Austin, TX: John Wiley & Sons, Inc., 2000.

[46] S. A. McInerny, "Launch vehicle acoustics part 2: statistics of the time domain data," *Journal of Aircraft,* vol. 33, no. 3, pp. 518-523, 1996.

[47] S. McInerny, M. Downing, C. Hobbs, M. James and M. Hannon, "Metrics that characterize nonlinearity in jet noise," in *AIP Conf. Proc.*, 2006.

[48] D. T. Blackstock, "Thermoviscous attenuation of plane, periodic, finite-amplitude sound waves," *J. Acoust. Soc. Am.,* vol. 36, no. 3, pp. 534-542, 1964.

[49] "Maple 16. Maplesoft, a division of Waterloo Maple Inc., Waterloo, Ontario.".

[50] R. O. Cleveland, J. P. Chambers, H. E. Bass, R. Raspet, D. T. Blackstock and M. F. Hamilton, "Comparison of computer codes for the propagation of sonic boom wavefomrs through isothermal atmospheres," *J. Acoust. Soc. Am.,* vol. 100, no. 5, pp. 3017-3027, 1996.

[51] L. D. Robinson, Sonic boom propagation through an inhomogeneous, windy atmosphere,

The University of Texas at Austin, 1991.

[52] H. E. Bass, R. Raspet, J. P. Chambers and M. Kelly, "Modification of sonic boom wave forms during propagation from the source to the ground," *J. Acoust. Soc. Am.,* vol. 111, no. 1, pp. 481-486, 2002.

[53] H. H. Brouwer, "Numerical Simulation of Nonlinear Jet Noise Propagation," *AIAA,* pp. AIAA-2005-3088, 2005.

[54] S. Saxena, P. J. Morris and K. Viswanathan, "Algorithm for the Nonlinear Propagation of Broadband Jet Noise," *AIAA Journal,* vol. 47, no. 1, pp. 186-194, 2009.

[55] M. F. Hamilton, Y. A. Il'inskii and E. A. Zabolotskaya, "Dispersion," in *Nonlinear Acoustics*, Acoustical Society of America, 2008, pp. 151-175.

[56] A. T. Wall, K. L. Gee, M. M. James, K. A. Bradley, S. A. McInerny and T. B. Neilsen, "Near-field noise measurements of a high-performance military jet aircraft," *Noise Control Eng. J.,* vol. 60, pp. 421-434, 2012.

Appendix A

McInerny Plots

This appendix defines and discusses another way to analyze the effects of nonlinear terms in propagation models that has been used to study jet aircraft and rocket noise. Since our understanding of this technique is still immature, and the results are preliminary, this analysis has been placed in an appendix, rather than a chapter.

Measures such as the WSF or the derivative skewness provide a convenient way to study an entire waveform, but specifics about the shock content can also provide useful information. McInerny and Ölcmen [33] developed a scatter plot (hereafter called a McInerny plot) in the study of rocket noise which provides information on some of the specifics of the shock content in a waveform. For every pressure rise, a point is placed on a plot where the horizontal axis is the difference of the maximum and minimum pressure for a given rise in pressure (Δp) and the vertical axis is the maximum rate of pressure increase between the times of the maximum and minimum pressure ($\partial p/\partial t|_{\mathrm{max}}$). They were able to show that Gaussian noise and noise with significant shock content followed different trends on this scatter plot.

In the form presented by Mcinerny and Ölçmen [33] the locations of the points on these McInerny plots depends greatly upon the overall sound pressure level and characteristic frequency of the waveform. Proper normalization of the axes of the scatter plots can aid the comparison of different waveforms with different general characteristics. Different normalization schemes can accentuate different aspects of a waveform. This appendix will make use of two normalization schemes of the McInerny plots, one emphasizing the importance of sufficient temporal resolution of shocks, which will be called the sampling rate normalization, and one emphasizing the waveform distortion due to nonlinear processes, which will be called the inverse local WSF (ILWSF) normalization.

The sampling rate normalization scheme consists of normalizing the vertical axis of the McInerny plot by the sampling frequency multiplied by the difference between the maximum and minimum pressure of a pressure rise ($[\partial p/\partial t|_{\max}]/f_s \Delta p$), and normalizing the horizontal axis by the standard deviation of the pressure amplitudes (which is the same as the root-mean-square of the pressure for zero-mean processes) of the entire waveform ($\Delta p/p_{\mathrm{rms}}$). The reason for this particular scheme is explained in Section A.2. The ILWSF normalization scheme consists of normalizing the vertical axis of the McInerny plot by the negative of the minimum slope of the pressure fall just after the pressure rise of interest ($-[\partial p/\partial t|_{\max}]/[\partial p/\partial t|_{\min}]$) and the horizontal axis by the standard deviation of the pressure amplitudes of the entire waveform ($\Delta p/p_{\mathrm{rms}}$). Since the WSF is the magnitude of the mean negative slope over the mean positive slope, the normalization of the vertical axis makes it what may be considered the inverse of a WSF for the region just around the pressure rise of interest, and is referred to as the inverse local WSF, and hence the name of the normalization scheme. The sampling rate normalization is used primarily in Section A.2 to elucidate some subtleties of using the McInerny plots with waveforms that have been sampled with a finite sampling rate. The ILWSF normalization will be the primary normalization scheme used to study measured waveforms in this appendix.

A.1 Analytical Treatment of the Khokhlov Solution

Since every pressure rise in a McInerny plot is accounted for, it is useful to know how idealized pressure rises will be placed on the plots. In order to do this, we will analyze the

Khokhlov solution in terms of the ILWSF normalization. We choose the Khokhlov solution because it is not written in the form of a Fourier series.

The Khokhlov solution is described in Section 2.2.3.5. The second time-derivative of the Khokhlov solution is given as

$$\frac{\partial^2 P}{\partial \theta^2} = \frac{1}{1+\sigma}\frac{\pi^2}{2\psi}\left(\frac{\pi}{\psi}\left(1-\tanh^2\frac{\pi}{2\psi}\theta\right)\tanh\frac{\pi}{2\psi}\theta\right). \tag{A.1}$$

Then the maxima and minima of the pressure slope may be found at the zeros of Equation (A.1), which occur at $\theta = 0$ and $\pm\infty$. Since the solution is only valid from $|\theta| < \pi$, we conclude that the waveform extrema are at $\theta = 0$ and $\pm\pi$. By observation, $\theta = 0$ is the location of the maximum slope, and $\theta = \pm\pi$ is the location of the minimum slope. Using Equation (2.43) we calculate the maximum slope to be

$$\left.\frac{\partial P}{\partial \theta}\right|_{\max} = \frac{1}{1+\sigma}\left[\frac{\pi^2}{2\psi} - 1\right] \tag{A.2}$$

and the minimum slope to be

$$\left.\frac{\partial P}{\partial \theta}\right|_{\min} = \frac{1}{1+\sigma}\left[\frac{\pi^2}{2\psi}\left(1-\tanh^2\frac{\pi^2}{2\psi}\right) - 1\right]. \tag{A.3}$$

The maximum pressure difference for the waveform is found to be

$$\Delta P = \left(P(\Theta_{\max}) - P(\Theta_{\min})\right), \tag{A.4}$$

which yields

$$\Delta P = \frac{1}{1+\sigma}\left[2\pi\sqrt{1-\frac{2}{\pi^2}\psi} - \frac{4}{\pi}\psi\tanh^{-1}\sqrt{1-\frac{2}{\pi^2}\psi}\right]. \tag{A.5}$$

Since the standard deviation of P does not have a closed form in terms of elementary functions, we use the standard deviation of the Fay solution, which is given as

$$P_{\text{Fay,rms}} = \frac{2}{\Gamma}\sqrt{\sum_{n=1}^{\infty}\frac{1}{\sinh^2(n\psi)}}. \tag{A.6}$$

Since the Khokhlov solution is for a periodic function with only a single pressure rise and a single pressure fall for each period, its representation on a McInerny scatter plot will be a single point. However, the location of that point will vary as the wave propagates. In particular, the location of the point on the McInerny scatter plot (without any normalization) will be

$$\begin{aligned}\left(\Delta p, \left.\frac{\partial p}{\partial \tau}\right|_{max}\right) &= \left(p_0 \Delta P, p_0 \omega \left.\frac{\partial P}{\partial \theta}\right|_{max}\right) \\ &= \frac{p_0}{1+\sigma}\left(2\pi\sqrt{1-\frac{2}{\pi^2}\psi} - \frac{4}{\pi}\psi \tanh^{-1}\sqrt{1-\frac{2}{\pi^2}\psi}, \omega\left[\frac{\pi^2}{2\psi}-1\right]\right).\end{aligned} \tag{A.7}$$

Equation (A.7) is plotted in Figure A.1 assuming $\sigma = 9$, for $\omega = 5\pi$, 10π, and 20π, and for $p_0 =$ 2 and 4.

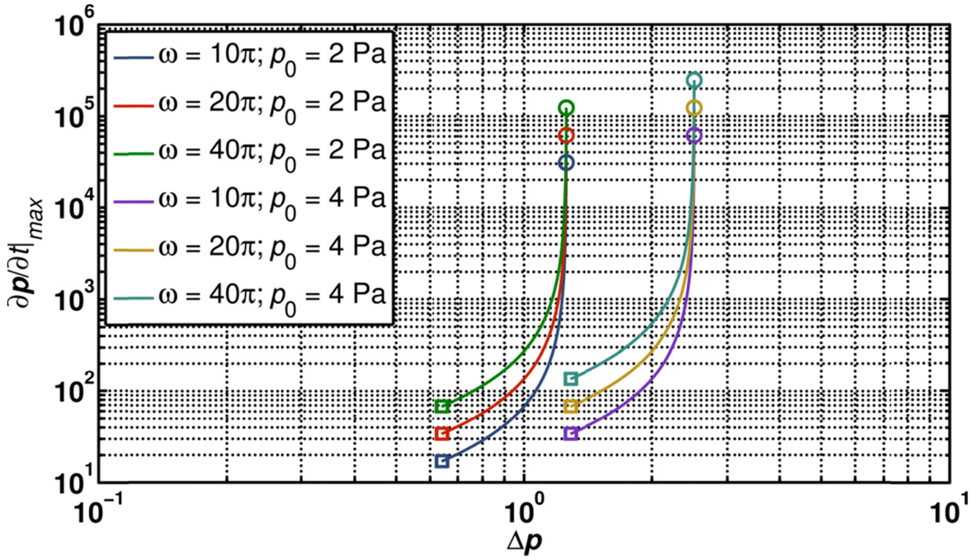

Figure A.1. McInerny plot locations for the Khokhlov solution for two initial amplitudes (2 and 4 Pa), and for three different initial angular frequencies (10π, 20π, and 40π rad/s). The locations are parametrically dependent upon $\psi = (1+\sigma)/\Gamma$, where σ is the distance from the source over the shock formation distance (assumed to be 9 for this plot) and Γ is the Gol'dberg number. The circles denote the locations for $\psi = 10^{-3}$, and the squares denote the locations for $\psi = 4/3$, and the lines between the two symbols of the same color are the locations for the values of $10^{-3} > \psi > 4/3$.

Notice that the locations on the McInerny plot shown in Figure A.1 for each combination of ω and p_0 follow a similar trend – approaching $(2\pi p_0/(1+\sigma), \infty)$ as $\psi \to 0$ and falling to the lower left of that point as ψ increases. Even though all of the cases follow a similar trend, the specific locations are highly dependent upon the initial amplitude and frequency.

The ILWSF normalization leads to a point which has a location of

$$\left(\frac{\Delta p}{P_{\text{Fay,rms}}}, -\frac{\left.\frac{\partial p}{\partial t}\right|_{max}}{\left.\frac{\partial p_K}{\partial t}\right|_{min}}\right) = \left(\frac{\frac{2}{\pi}\left(\frac{1}{\Psi}\sqrt{1-\Psi}-\tanh^{-1}\sqrt{1-\Psi}\right)}{\sqrt{\sum_{n=1}^{\infty}\frac{1}{\sinh^2\left(n\frac{\pi^2}{2}\Psi\right)}}}, \frac{1-\Psi}{\tanh^2\left(\frac{1}{\Psi}\right)-1-\Psi}\right), \tag{A.8}$$

where $\Psi = 2\psi/\pi^2$, which is plotted in Figure A.2, below. The locations in Figure A.2 follow a very similar trend as the locations in un-normalized scatter plot, but now all initial amplitudes and frequencies fall upon the same curve. For very small values of ψ, which indicates significant shocks, the vertical position diverges upwards (suggesting that an ILWSF value above 10^3 is large), and for values of ψ near 4/3 the vertical position approaches unity. The fact that all frequencies and initial amplitudes follow the same trend allows for more ready comparison of the nonlinear distortion of waveforms with different initial conditions. For example, if an initially sinusoidal signal propagating with thermoviscous losses was found to have a vertical position on the McInerny scatter plot with ILWSF normalization of about 1000, then it is likely to have significant shocks. On the McInerny plot without normalizations, a vertical position of about 1000 means nothing without the initial frequency and amplitude.

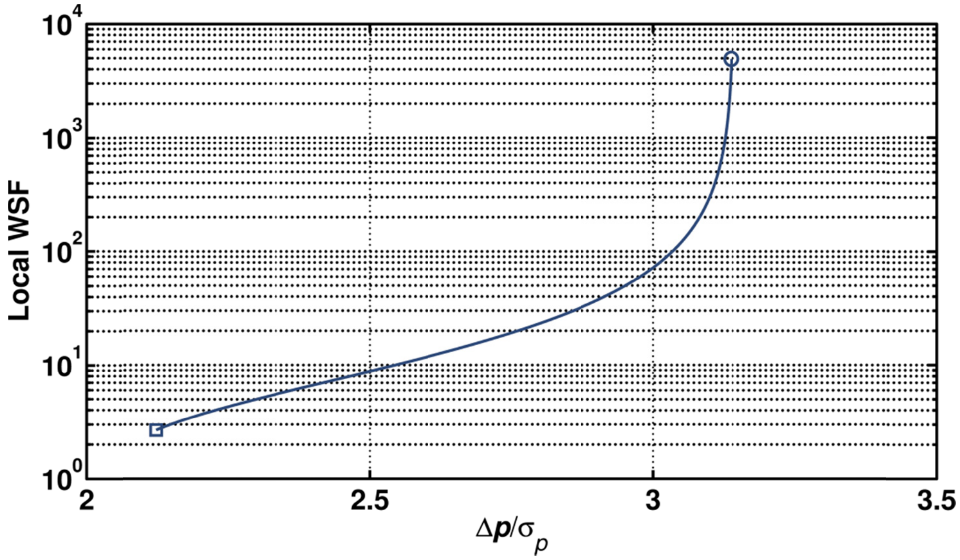

Figure A.2. McInerny plot with ILWSF normalization locations for the Khokhlov solution. The locations are parametrically dependent upon $\psi = (1+\sigma)/\Gamma$, where σ is the distance from the source over the shock formation distance and Γ is the Gol'dberg number. The circle denotes the location for $\psi = 10^{-3}$, and the square denotes the location for $\psi = 4/3$, and the line between the two are the locations for the values of $10^{-3} > \psi > 4/3$.

While the derivation here assumed that the waveform was sinusoidal, the conclusions can be readily interpreted for narrowband noise as well. Narrowband noise can be described as an amplitude-modulated sine wave. Thus, each pressure rise is like one oscillation of a sine wave with a given amplitude, which is only loosely related to the amplitude of the next pressure rise. Since each pressure rise has its own amplitude, it is implied that it will have its own value of σ. Thus, given a narrowband plane wave that propagates according to the Burgers equation, the curve in Figure A.2 describes the distribution of points on a normalized McInerny plot of said waveform. However, this interpretation must be made carefully, because the standard deviation is of the entire narrowband noise waveform, and not just for the waveform locally around a pressure rise. Thus, the positions of the points on a McInerny plot of narrowband noise are likely to be spread about horizontally somewhat.

A.2 Effects of Finite Sampling Rate on McInerny Plots

The plots used by McInerny and Ölcmen [33] compared the maximum time-derivative of pressure between adjacent pressure minima and maxima with the pressure difference between the respective pressure maxima and minima. These quantities depend only upon a single shock, so this analysis will focus on different types of individual shocks. For each of these shocks, we will assume that the sampling rate is $f_s = 1/\Delta t$, and that the difference between the maximum and minimum pressures is Δp.

A.2.1 Two-Data-Point Shock

The minimum number of data points that could possibly constitute a shock is two, where the first data point has a pressure of p_{min} and the second data point has a pressure of $p_{\max}$. Therefore, the time derivative of this shock is found to be simply $\Delta p/\Delta t = \Delta p f_s$. This means that the location of this shock on a McInerny plot will be $(\Delta p, \Delta p f_s)$. Using the sampling frequency normalization defined just before Section A.1, the vertical position of the shock on a scatter plot would become one, regardless of the pressure increase.

A.2.2 Three-Data-Point Shock

Suppose that a shock consists of three data points, with pressures $p_{\min}$, p_2, and $p_{\max}$. Define the pressure differences $\Delta_1 = p_2 - p_{\min}$ and $\Delta_2 = p_{\max} - p_2$. Without loss of generality, we may assume that $\Delta_2 \geq \Delta_1$. There are two limiting cases for the three-data-point shock, which is that $\Delta_2 = \Delta_1 = \Delta$, or that $\Delta_2 \gg \Delta_1$. If we examine the first limiting case, we find that $\Delta p = 2\Delta$, and the maximum time-derivative estimate is

$$\frac{\Delta}{\Delta t} = f_s \Delta. \tag{A.9}$$

Therefore the vertical position of this shock on the normalized scatter plots would be

$$f_s \Delta / 2 f_s \Delta = 1/2. \tag{A.10}$$

Examining the second limiting case, we find that $\Delta p = \Delta_1 + \Delta_2 \approx \Delta_2$, and that the maximum time-derivative estimate is $\Delta_2 f_s$. Then the vertical position of this shock on the normalized scatter plots would be $\Delta_2 f_s / \Delta_2 f_s = 1$. Since all three-point-shocks must fall between these two limiting cases, we conclude that the vertical position of any three-point-shock is constrained to be between one half and one.

A.2.3 *i*-Data-Point Shock

Using similar arguments as those in the three-data-point shock discussion, it can be shown that all shocks with i data points will be constrained to stay between $1/(i-1)$ and one.

A.2.4 ILWSF Normalization

The limitations discussed above also apply to the ILWSF normalization scheme, except that the ILWSF normalization uses both the positive and negative slope extrema, not just the positive. Constraints on the estimate of the negative slope apply much as they do for the positive slopes discussed above. However, for most waveforms with significant shock content, the pressure increase usually happens much faster than the succeeding pressure decrease. This means that the estimate of the true location of a pressure rise and fall on the McInerny plot with ILWSF normalization is likely to be more accurate than an estimate of the true location on a McInerny plot with no normalization. However, if there are any small scale oscillations, physical or digital, around a pressure rise, then the calculated location on a McInerny plot with ILWSF normalization may be misleading.

A.3 McInerny Plots of Plane Wave Tube Measurements

The waveforms measured in the plane wave tube experiments described in Chapter 5 were analyzed in terms of McInerny plots, in addition to the WSF and derivative skewness. Once again, the purpose of using a plane wave tube measurement is that it allows for a relatively well understood system. The known geometrical propagation and absorption in a plane wave tube give the necessary information to be able to discern what phenomena are due to nonlinearity.

McInerny plots allow one to study each pressure rise in a given waveform as a part of a set. This approach seems to be especially useful in studying nonlinear noise propagation because not every pressure rise in a distorted noise waveform is going to be a shock, or even have significant nonlinear distortion. As discussed above, the McInerny plots presented here will be normalized using the ILWSF normalization scheme. This means that every pressure rise and succeeding pressure fall will create a single point on the scatter plot, located at

$$\left(\frac{\Delta p}{p_{\mathrm{rms}}}, -\frac{\partial p/\partial t|_{\max}}{\partial p/\partial t|_{\min}}\right), \tag{A.11}$$

where Δp is the pressure difference between the greatest and smallest pressure measured for the pressure rise of interest, p_{rms} is the standard deviation of the pressure of the entire waveform, $\partial p/\partial t|_{\max}$ is the time-derivative estimate during the pressure rise of interest with the greatest value, and $\partial p/\partial t|_{\min}$ is the time-derivative estimate during the succeeding pressure fall with the lowest value. The vertical position is also referred to as the ILWSF. Higher values of the ILWSF indicate that the waveform shows more nonlinear waveform distortion, higher values of $\Delta p/p_{\mathrm{rms}}$ indicate large pressure rises. The region of a McInerny plot most likely to describe shocks in a waveform then is near the upper right corner.

In order to facilitate an understanding of the McInerny plots of the waveforms measured in the plane wave tube, McInerny plots of numerically generated, specrally (a) white, (b) broadband, and (c) narrowband Gaussian noise are shown in Figure A.3, along with two-dimensional histograms of the plots. Both the broadband and narrowband Gaussian noise signals were given a characteristic frequency of 1500 Hz, and have a bandwidth of 1600 Hz and 100 Hz, respectively. The varying bandwidths were obtained by bandpass filtering the white Gaussian noise signal. The number of samples in each waveform is 2^{18}, and an artificial sampling frequency of 204800 Hz was chosen.

The McInerny plots in Figure A.3 themselves do not yield much information. It is noted that the points on a McInerny plot due to Gaussian noise lie within a triangular shaped region. This triangular region is significantly reduced in size for narrower bandwidths. In particular the triangular region of the plot of the narrowband waveform (plot (c)), is very narrow, to the point that it may be considered to be a line. The narrowband noise positions appear to be consistent with the interpretation of the results in Section A.1. Notice that the majority of points in plot (a) and all of the points in plots (b) and (c) have values of ILWSF less than 1000, which is also consistent with the guidelines found in Section A.1.

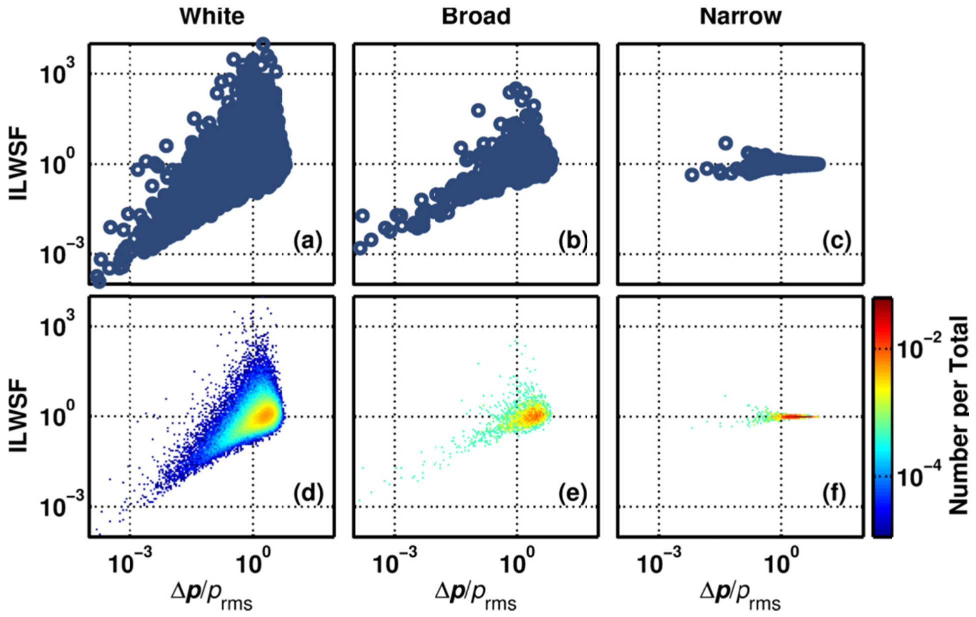

Figure A.3. McInerny plots of numerically generated spectrally (a) white, (b) broadband, and (c) narrowband Gaussian noise waveforms. The corresponding two-dimensional histograms are shown in plots (d), (e), and (f).

The histograms present more information on the densities of the McInerny plots, in addition to the same information as the original plots. In addition to the triangular shape found in the McInerny plots, the associated histograms also show that the densest region of the plots is just above $\Delta p/p_{\mathrm{rms}} = 1$ and at about ILWSF = 1. The value of the ILWSF of the peak region of the McInerny plots can be understood by recalling that the WSF of Gaussian noise is one. Since the two-dimensional histograms of the McInerny plots provide the same and more information as the McInerny plots of a waveform, only the two-dimensional histograms will be presented for the remainder of this appendix.

The two-dimensional histograms of the McInerny plots of measured noise waveforms are quite complicated compared to numerically generated Gaussian noise waveforms. The histograms of the McInerny plots of initially broadband Gaussian noise measured in the plane wave tube (a) 0.3 m and (b) 11.6 m from the source are shown in Figure A.4. The histogram in plot (a) rather resembles the histogram in Figure A.3(e). Since the initial waveform was Gaussian, the fact that the histogram of the waveform measured 0.3 m from the source resembles the histogram of a Gaussian waveform is expected. The histogram in plot (b), on the other hand, is very different from any of the histograms in Figure A.3. The general features in the histogram of the waveform measured 11.6 m from the source are the large mass of points centered about $(\Delta p/p_{\mathrm{rms}}, \mathrm{ILWSF}) = (10^{-2}, 1)$ and the smaller and more complicated mass of points centered about (2,10). Both of these groups of points will be discussed below.

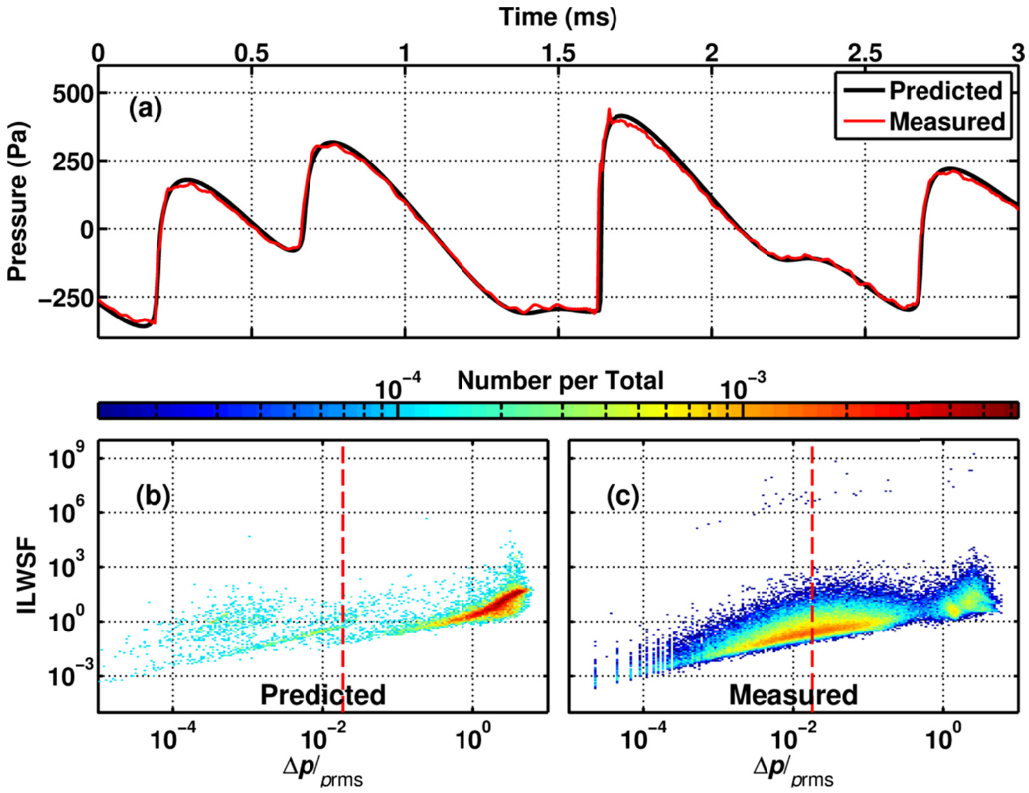

Figure A.4. Two-dimensional histograms of McInerny plots initially broadband Gaussian noise measured 0.3 (a) and 11.6 m (b) from the source in a plane wave tube. The red dashed lines represent the lower bound used by McInerny and Ölçmen. [33]

As mentioned in Section A.1, any small scale oscillations near significant pressure rises in a waveform can greatly reduce the significance of the data in a McInerny plot. As with any acoustical measurement, some unexpected, random vibration in the waveform is inevitable. Since unexpected noise is generally very small in amplitude relative to the main waveform, we may assume that points on a scatter plot with very small values of $\Delta p/p_{\mathrm{rms}}$ are not likely to be meaningful. McInerny and Ölçmen accounted for this by only considering pressure rises that are larger than 0.3% of the amplitude of the largest pressure rise in the waveform. [33] This lower threshold is plotted as the red dashed lines in Figure A.4. If this limit is considered to be meaningful, then the large group of points centered about $(10^{-2}, 1)$ is likely to be associated with unexpected vibrations.

Another way to identify data that are meaningful is to compare a waveform at different stages of its propagation. Notice that the histogram in Figure A.4(a) only has one region with a high point-density, centered about (2, 1). Since the waveforms being considered are much longer than their characteristic periods, it may be assumed that only the trends of high-density regions can be interpreted in terms of propagation effects. Thus, much of the histogram in plot (a) is not likely to be meaningful. Since the area around (2, 1) seems to characterize the waveform measured 0.3 m from the source, it is likely that propagation would cause a continuous modulation of this region. Thus, the cluster of points about (2,10) in plot (b) is the most likely cluster in the histogram to have meaning with respect to propagation.

A simple numerical test can be used to test the hypothesis that the points in Figure A.4(b) near (2,10) are the important ones. A prediction of the waveform that was measured 11.6 m from the source was obtained using the propagation model discussed in Chapter 4. The waveform analyzed in Figure A.4(a), which was measured 0.3 m from the source, was used as the input waveform. The measured and predicted waveforms are shown in Figure A.5(a), the two-dimensional histogram of the McInerny plot of the measured waveform is shown in Figure A.5(b), and the histogram of the predicted waveform is shown in Figure A.5(c). The predicted waveform is nearly identical to the measured waveform with the notable exception of some small oscillations. Note that the histogram of the predicted waveform has significantly less data beyond the cluster near (2, 10) than the histogram of the measured waveform. The lack of oscillations in the waveform and compactness of the points in the histogram of the predicted waveform suggests that the large cluster of points in plot (c) are due to some kind of systematic error in the measurement.

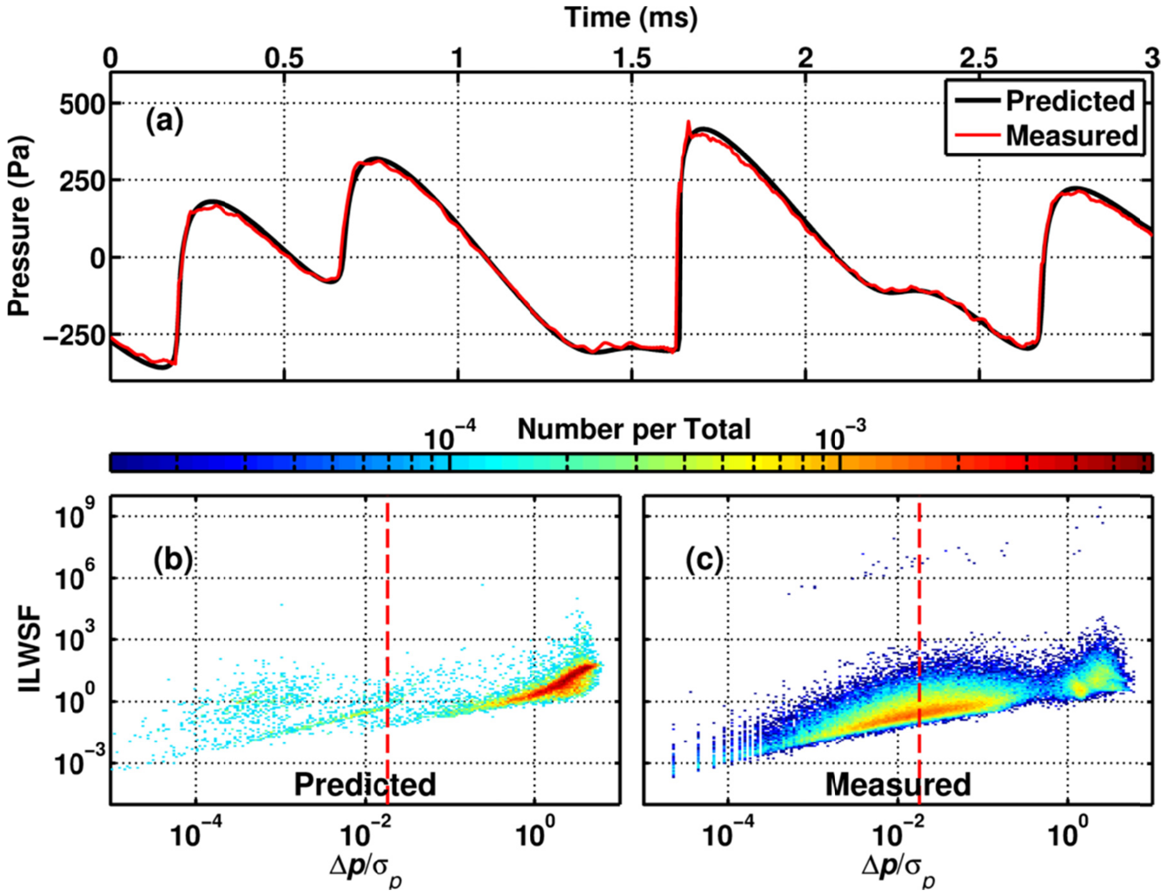

Figure A.5. (a) Portions of an initially broadband Gaussian noise waveform measured at 11.6 m from the source in an anechoically terminated plane wave tube and a numerical prediction. (b) Two-dimensional histograms of the McInerny plot of the predicted waveform. (c) Two-dimensional histograms of the McInerny plot of the measured waveform. The noise at the measurement location has a *σ* value of 1.14. The data inside the red circles are not likely to be meaningful, while the data in green squares are.

As noted by the presence of significant shocks in the waveforms in Figure A.5(a), it is very likely that nonlinear distortion is important in the propagation of this particular signal. Based on the findings in Section A.2, we expect to find a significant number of points with ILWSF values near or above 1000. This is the case for both histograms in Figure A.5. While the regions with the greatest densities do not quite make it to 1000, they are within an order of magnitude.

The histograms of the McInerny plots of noise waveforms at various locations in the plane wave tube may be compared in order to better understand how McInerny plots evolve with nonlinear propagation. In order to simplify the explanations, all of the histograms of waveforms measured in the plane wave tube presented below will be compared with the histograms of an initially broadband Gaussian noise waveform with a characteristic frequency of 1500 Hz. The waveforms analyzed were chosen to have σ values similar to those of the reference waveforms. Following McInerny and Ölçmen, only those points on the McInerny plot with values of Δp greater than 0.3% of the maximum value of the waveform are included in the plots.

First, the reference set of histograms (initially 1500 Hz, broadband Gaussian noise) will be discussed. Then, the effects of different characteristic frequencies will be discussed by comparing histogram sets from initially 1000 Hz and from 2000 Hz broadband Gaussian noise waveforms with the reference set. The effects of bandwidths are then analyzed by comparing initially 1500 Hz narrowband Gaussian noise with reference set. Finally, initially 1500 Hz broadband jet noise-like noise will be compared with the reference set to understand the effects of different initial statistics.

Initially 1500 Hz, Broadband Gaussian Noise

Portions of the histograms of the McInerny plots of initially 1500 Hz broadband Gaussian noise measured in a plane wave tube (a) 0.3 m, (b) 2.5 m, (c) 5.6 m, (d) 8.6 m, and (e) 11.6 m from the source are shown in Figure A.6. (It should be noted that the portions shown in plot (a) and plot (e) are portions of the histograms shown in Figure A.4 and Figure A.5.)

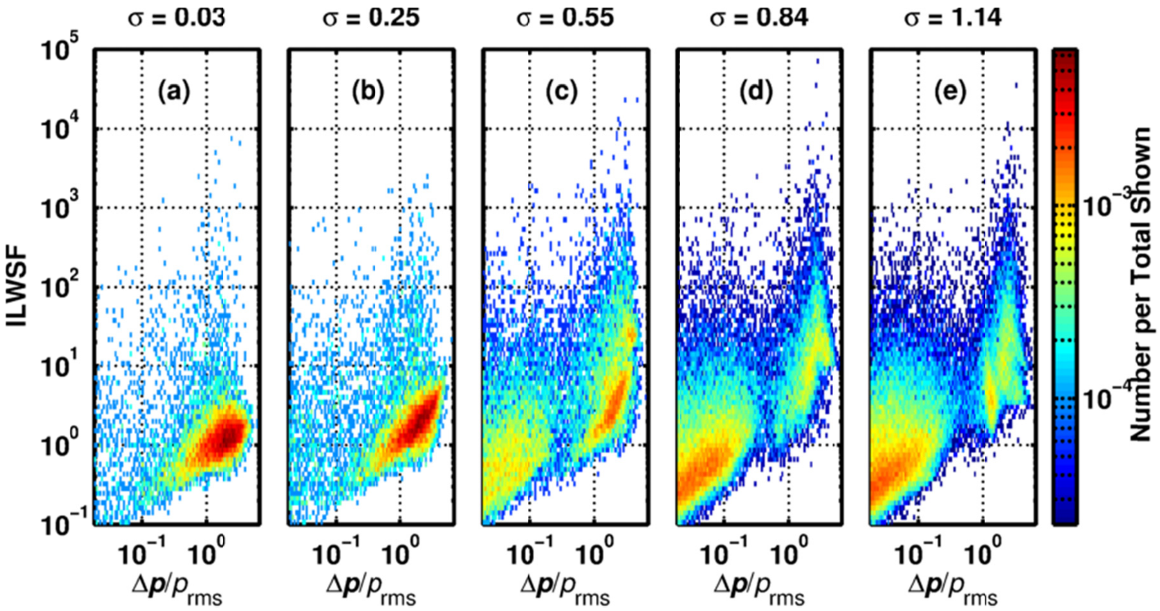

Figure A.6. Portions of the histograms of the McInerny plots of initially 1500 Hz broadband Gaussian noise measured in a plane wave tube (a) 0.3 m, (b) 2.5 m, (c) 5.6 m, (d) 8.6 m, and (e) 11.6 m from the source.

The histograms shown in Figure A.6 illustrate much of the evolution of initially broadband noise. Plot (a) shows that most of the pressure rises are located in one region centered around (1, 2). The points surrounding this region appear to be in a somewhat triangular shape. This triangular shape was found in the analysis of a numerical Gaussian signal. In plot (b) this main region appears to be evolving. The portion of this region with larger values of $\Delta p/p_{\mathrm{rms}}$ have obtained larger values of ILWSF, while the portion of the region with lower values of $\Delta p/p_{\mathrm{rms}}$ have not changed their values of ILWSF very significantly. The points surrounding the dense region in plot (b) still form a kind of triangular shape. The increase in ILWSF of the points with larger values of $\Delta p/p_{\mathrm{rms}}$ may be explained by nonlinear distortion. The portions of the initial waveform with larger pressure excursions will distort more rapidly than the portions with small pressure excursions.

The transition from plot (b) to plot (c) is similar to the transition from plot (a) to plot (b). The large dense region in plot (c) has continued to evolve, elongating as the points with larger values of $\Delta p/p_{\mathrm{rms}}$ continue to gain even higher values of ILWSF, suggesting that these portions of the noise waveform are becoming significantly distorted. It appears that the main dense region has bifurcated into two portions, one centered about (2, 3) and the other centered about (3, 27). In addition to the main dense region on the right hand side of the plot, another dense region has started to form on the left hand side of the plot. It appears to be truncated by the threshold introduced by McInerny and Ölçmen, suggesting that this region is similar to the region centered about $(10^{-2}$,1) in Figure A.4(b). The dense region developing on the left of plot (c) is likely noise generated by some systematic error in the measurement.

By plot (d) the dense region on the left of the histogram has become the main dense region in the histogram. However, the dense region on the right, which is more likely to represent the evolution of the initial waveform, is still easily distinguishable. The dense region on the right side of the histogram still looks like there are two portions of it, creating an inverted “v” shape. The peak of the “v” shape is located near (3, 80). It is interesting that largest values of ILWSF for the dense region on the right of plot (d) is approximately the same as the largest values of the ILWSF for the dense region on the right of plot (c), as well as the largest ILWSF values for the dense region on the right of plot (e). While there is some interesting structure to these right-hand dense regions, the overall shape does not vary much between plots (c), (d), and (e), suggesting that the waveform has reached a more stable part of the propagation by $\sigma = 0.55$. The most likely case would be that the waveform has already passed some threshold similar to the shock formation distance for sine waves. This conclusion is strengthened by the derivative skewness estimates presented in Section 5.6. The derivative skewness estimates of noise follow a similar trend of the initially sinusoidal signals, but progress at much faster in terms of σ.

Characteristic Frequency Comparison

Comparing the histograms of McInerny plots of initially broadband Gaussian noise with different characteristic frequencies can help us understand the importance of absorption on the nonlinear propagation of noise.

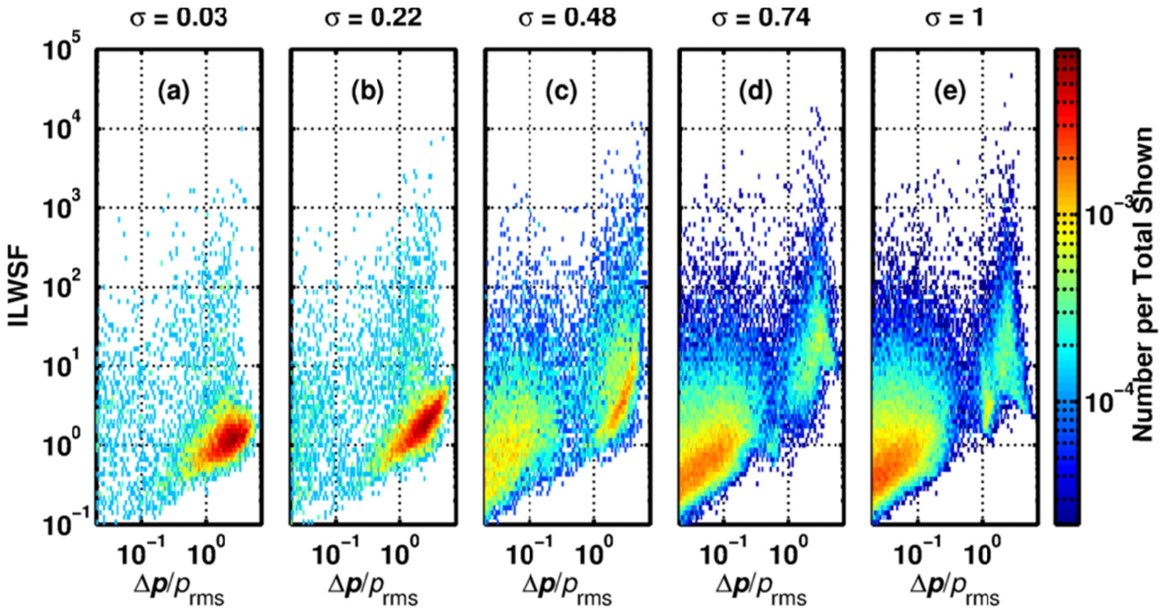

Figure A.7. Portions of the histograms of the McInerny plots of initially 1000 Hz broadband Gaussian noise measured in a plane wave tube (a) 0.3 m, (b) 2.5 m, (c) 5.6 m, (d) 8.6 m, and (e) 11.6 m from the source.

All of the trends that were seen in Figure A.6 are seen in the histograms in Figure A.7. Although the dense region on the right of plot (c) of Figure A.7 does not seem to have bifurcated yet, evidence of the region splitting is seen in plot (d) and plot (e).

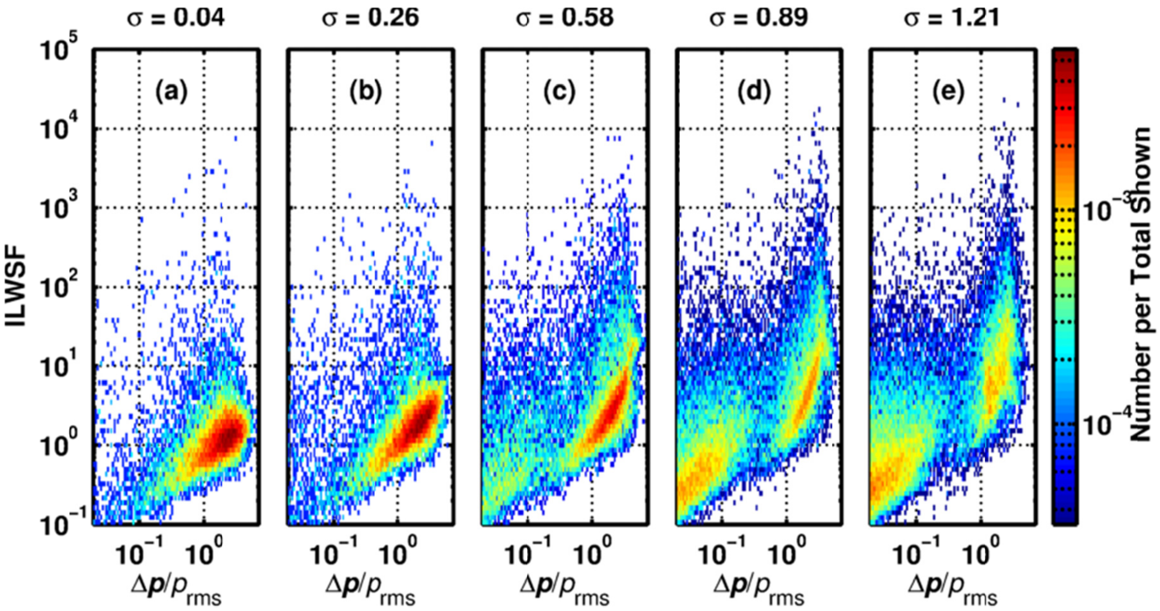

Figure A.8. Portions of the histograms of the McInerny plots of initially 2000 Hz broadband Gaussian noise measured in a plane wave tube (a) 0.3 m, (b) 2.5 m, (c) 5.6 m, (d) 8.6 m, and (e) 11.6 m from the source.

The general trends seen in Figure A.6 are present in the histograms of the higher frequency waveforms shown in Figure A.8, but there are some interesting differences. For example, the evolution of the dense region on the right seems to be progressing, but at a slower rate (in terms of σ) than the 1500 Hz case. It isn't until $\sigma = 1.21$ (plot (e)) that the dense region on the right begins to bifurcate, unless the dense region on the left in plots (c), (d), and (e) is actually a bifurcation of the dense region on the right. The fact that the dense region on the left grows in a similar manner as the dense region on the left of Figure A.6 suggests that the dense region on the left in Figure A.8 is noise associated with some systematic error in the measurement.

Bandwidth Comparison

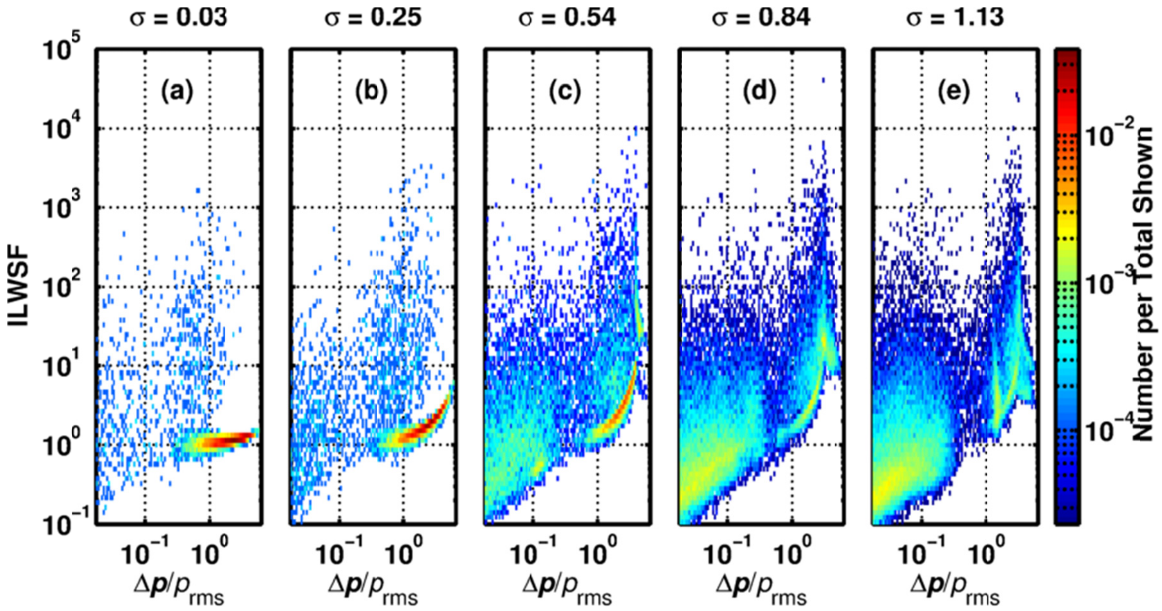

Figure A.9. Portions of the histograms of the McInerny plots of initially 1500 Hz narrowband Gaussian noise measured in a plane wave tube (a) 0.3 m, (b) 2.5 m, (c) 5.6 m, (d) 8.6 m, and (e) 11.6 m from the source.

Portions of the histograms of initially 1500 Hz narrowband Gaussian noise measured at various locations in a plane wave tube are shown in Figure A.9. The first and most obvious difference between the histograms in Figure A.6 and in Figure A.9 is that the dense region on the right in the plots of Figure A.9 is much narrower than the dense regions on the right in the plots of Figure A.6. In spite of the much narrower dense region, the dense regions on the right of the plots in Figure A.9 undergo a similar evolution to the dense region on the right of the plots in Figure A.6: The portions with larger values of $\Delta p/p_{\mathrm{rms}}$ tend to shift to larger values of ILWSF. The dense region on the right also apparently bifurcates at or near $\sigma = 0.54$, as seen in plot (c). It seems that the stable part of the waveform propagation still has not started by $\sigma = 0.54$, but has started by $\sigma = 0.84$, as seen in plot (d) and plot (e).

Initial Statistics Comparison

Since jet noise has different statistical characteristics than Gaussian noise, we now see if this has a noticeable effect on the histograms of the McInerny plots of noise with jet noise-like statistics. Portions of these histograms are shown in Figure A.10. The histogram portions shown in Figure A.10 are remarkably similar to the histogram portions shown in Figure A.6. The dense region in plot (a) shows the triangular shape associated with Gaussian noise, and is centered about (2, 1). By 2.5 m (shown in plot (b)), the dense region has begun to evolve, with large values of $\Delta p/p_{\mathrm{rms}}$ going to higher values of ILWSF. Note that the dense region on the right in plot (c) appears to have bifurcated, that the same region in plot (d) has formed a sort of inverted "v" shape, and that characteristics of the histogram portions shown in plots (c), (d), and (e) do not vary much. All of these observations were also made of the histogram portions in Figure A.6. These similarities suggest that the initial statistics do not have a significant effect on the nonlinear propagation of broadband noise.

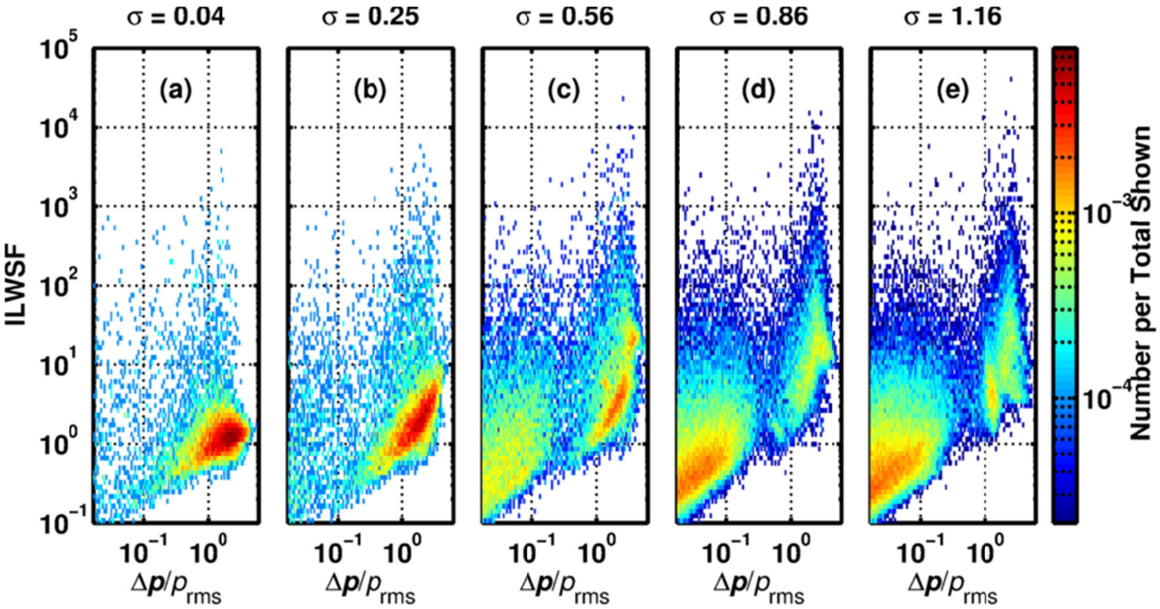

Figure A.10. Portions of the histograms of the McInerny plots of initially 1500 Hz broadband noise with jet noise-like statistics measured in a plane wave tube (a) 0.3 m, (b) 2.5 m, (c) 5.6 m, (d) 8.6 m, and (e) 11.6 m from the source.

The analyses presented above have shown that the evolution of McInerny plots are similar for all noise waveforms in a plane wave tube. It does appear that the absorption and dispersion associated with propagation in a plane wave tube affects the plots significantly, and different phenomena may be manifested in McInerny plots for measure jet noise, which is not planar, and does not propagate with boundary layer effects.

A.4 Analysis of Jet Noise

The two-dimensional histograms of the McInerny plots of waveforms measured during the intermediate and military engine conditions, measured on the ground array at 0 m, 10.4 m, and 20.7 m downstream of the nozzle, are shown in Figure A.11 and Figure A.12.

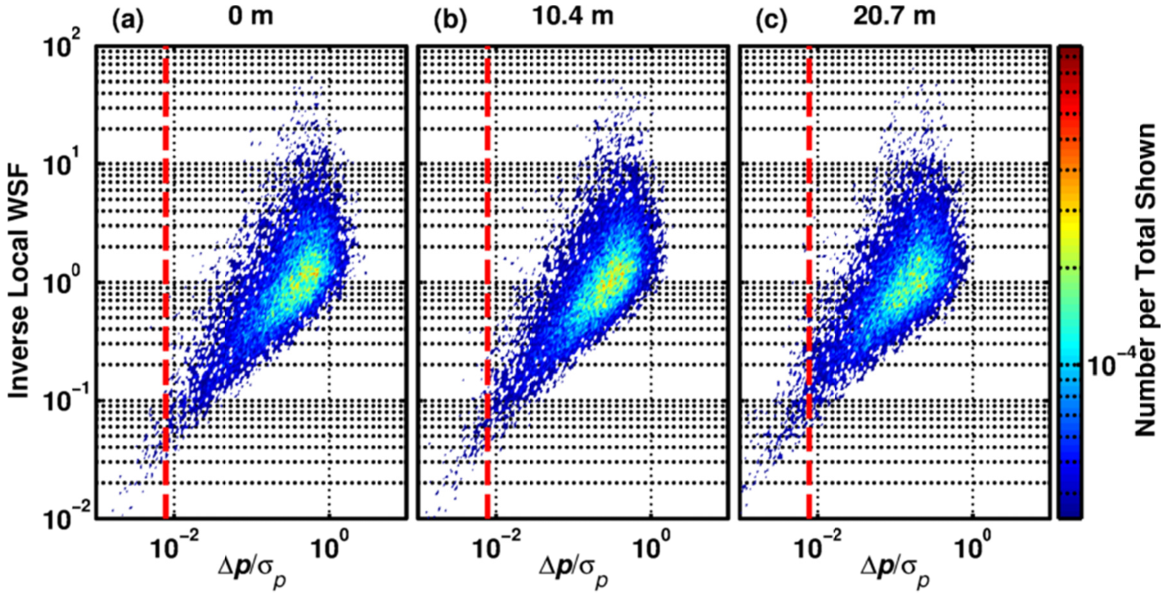

Figure A.11. Two-dimensional histograms of McInerny plots with ILWSF normalization of noise waveforms measured on the ground array (a) 0 m, (b) 10.4 m, and (c) 20.7 m downstream of the nozzle of an F22-A Raptor at intermediate engine condition. The red dashed line represents the threshold suggested by McInerny and Ölçmen.

The histograms shown in Figure A.11 show the characteristic triangular shape that is expected for broadband Gaussian noise. Compared to the scatter plots calculated when discussing the tube data, the peaks of the histograms in Figure A.11 have low values of $\Delta p/p_{\mathrm{rms}}$, and there is only one peak per histogram. This suggests that there is a low frequency wave that carries high frequency energy, which is the case, as seen in Figure 6.2.

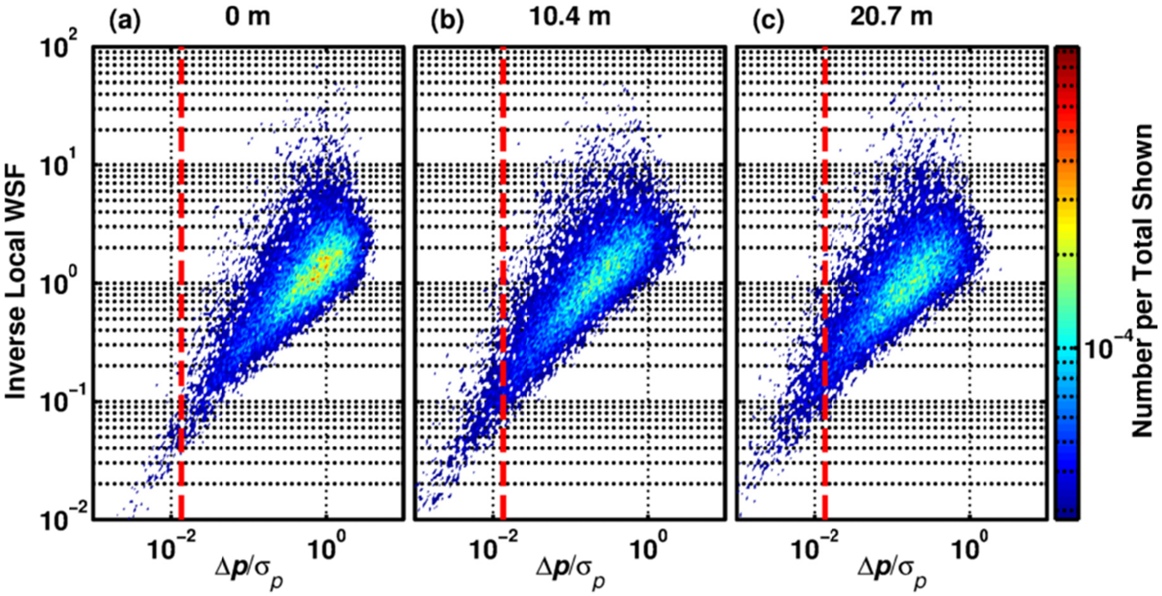

Figure A.12. Two-dimensional histograms of McInerny plots with ILWSF normalization of noise waveforms measured on the ground array (a) 0 m, (b) 10.4 m, and (c) 20.7 m downstream of the nozzle of an F22-A Raptor at military engine condition. The red dashed line represents the threshold suggested by McInerny and Ölçmen.

The histograms for the military engine condition shown in Figure A.12 are very similar to the histograms for the intermediate engine condition shown in Figure A.11. The dense regions still retain the triangular shape, though they do seem to be a little more extended than the dense regions of the histograms for the intermediate engine condition, especially the histogram in Figure A.12(b).

As seen in the histograms analyzed for the plane wave tube experiments, the slight extension of the dense region in the histograms in Figure A.12 likely implies nonlinear propagation. One can estimate a value of σ for the noise used to generate the histograms. Comparing the histograms with the histograms from Section A.3, the noise measured during the intermediate engine condition likely has a σ value near zero, and the noise measured during the military engine condition likely has a σ value near 0.1. This choice is quite subjective, and therefore quite imprecise. It may be that histograms of McInerny plots will be more useful when comparing waveforms with greater shock content than the waveforms considered in this appendix.